

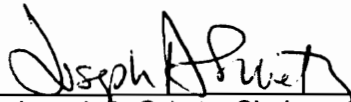
**NEW INTEGRAL AND DIFFERENTIAL COMPUTATIONAL PROCEDURES
FOR INCOMPRESSIBLE WALL-BOUNDED TURBULENT FLOWS**

by

Jean Caillé

Dissertation submitted to the Faculty of the
Virginia Polytechnic Institute and State University
in partial fulfillment of the requirements for the degree of
Doctor of Philosophy
in
Aerospace Engineering

APPROVED:


Joseph A. Schetz, Chairman


Roger L. Simpson


Bernard Grossman


J. N. Reddy


Dominique H. Pelletier

September, 1992
Blacksburg, Virginia

NEW INTEGRAL AND DIFFERENTIAL COMPUTATIONAL PROCEDURES FOR INCOMPRESSIBLE WALL-BOUNDED TURBULENT FLOWS

by

Jean Caillé

Joseph A. Schetz, Chairman

Aerospace Engineering

(ABSTRACT)

Three new computational procedures are presented for the simulation of incompressible wall-bounded turbulent flows. First, an integral method based on the strip-integral method has been developed for the solution of three-dimensional turbulent boundary-layer flows. The integral equations written in a general form using non-orthogonal streamline coordinates include the turbulent shear stress at the upper limit of an inner strip inside the boundary-layer. The shear stress components are modeled using the Boussinesq assumption, and the eddy viscosity is defined explicitly as in differential methods. The turbulence modeling is not hidden in opaque empirical correlations as in conventional integral methods. A practical four-parameter velocity profile has been established based on the Johnston Law of the Wall using a triangular model for the crosswise velocity. Two strips are used to solve for the four unknowns: skin friction coefficient, wall crossflow angle, boundary-layer thickness, and location of maximum crosswise velocity. The location of maximum crosswise velocity proves to be a natural and adequate parameter in the formulation, but it is numerically sensitive and has a strong influence on the wall crossflow angle. Good results were obtained when compared to predictions of other integral or differential methods.

Secondly, two computational procedures solving the Reynolds Averaged Navier-Stokes equations for 2D and 3D flows respectively have also been developed using a new treatment of the near-wall region. The flow is solved down to the wall with a slip velocity based on Clauser's idea of a pseudolaminar velocity profile. The present idea is different from the wall-function methods and does not require a multi-layer eddy viscosity model. The solution of the equations of motion is obtained by the Finite Element Method using the wall shear stress as a boundary condition along solid surfaces, and using the Clauser outer region model for the eddy viscosity. The wall shear stress distribution is updated by solving integral equations obtained

from the enforcement of conservation of mass and momentum over an inner strip in the near-wall region. The Navier-Stokes solution provides the necessary information to the inner strip integral formulation in order to evaluate the skin friction coefficient for 2D flows, or the skin friction coefficient and the wall crossflow angle for 3D flows. The procedures converge to the numerically "exact" solution in a few iterations depending on the accuracy of the initial guess for the wall shear stress. A small number of nodes is required in the boundary-layer to represent adequately the physics of the flow, which proves especially useful for 3D calculations. Excellent results were obtained for the 2D simulations with a simple eddy viscosity model. 3D calculations gave good results for the turbulent boundary-layer flows considered here.

The present methods were validated using well-known experiments chosen for the STANFORD conferences and EUROVISC workshop. The 2D numerical predictions are compared with the experimental measurements obtained by Wieghardt-Tillmann, Samuel-Joubert, and Schubauer-Klebanoff. For the 3D analyses, the numerical predictions obtained by the strip-integral method and the Finite Element Navier-Stokes Integral Equation procedure are validated using the Van den Berg-Elsenaar and Müller-Krause experiments.

ACKNOWLEDGEMENTS

I would like to express my appreciation and gratitude to my advisor, Dr. Joseph A. Schetz, for his ideas, his support and guidance, his competent teaching, and also for his infinite enthusiasm and patience throughout my studies and research. It was an honor and a pleasure to share time and energy with a great scientist.

I also extend my gratitude to my committee members, Drs. R. L. Simpson, B. Grossman, J. N. Reddy, and D. H. Pelletier, for their comments on this work, for their teaching, and for many fruitful discussions. I also want to thank Dr. H. L. Moses for the discussions we shared about his original work with the strip-integral method, which is at the basis of the present work.

I owe a special thank to Mr. William W. Richardson of the Computing Center who was always present and dedicated, answering all sorts of requests and helping solve many problems with the computers and the program FIDAP.

I wish to thank three organizations for their financial support: the Aerospace and Ocean Engineering department, the Office of Naval Research, and the Fonds F.C.A.R. of the province of Québec.

A few persons, although not directly implicated in my field of study and research, had an inestimable influence on me. They taught me about the qualities, the responsibilities, and the duties of a Doctor of Philosophy as a scientist and as a human being. My gratitude and admiration go to Hélène Lecaudey, Evelyne Chaussé-Caillé, Dr. Gilles Caillé, and Dr. James Robert Mahan for their teaching, inspiration, and friendship.

Finally, I would like to thank my family, as well as my dear friends from all over the world for helping me enjoy the experience of being an international student and for reminding me that the "Doctorate of Life" is also important.

TABLE OF CONTENTS

Acknowledgements.....	iv
Nomenclature.....	vi
List of Tables.....	viii
List of Figures.....	ix
Chapter 1 Introduction.....	2
Chapter 2 Ideas, Concepts, and Morphology	7
2.1 Morphology of Flows	7
2.2 Morphology of Mathematical and Turbulence Models.....	8
2.3 Morphology of Numerical Methods	19
Chapter 3 Three-Dimensional Strip-Integral Method	26
3.1 Integral Equations	26
3.2 Velocity Profile.....	28
3.3 Turbulence Model.....	29
3.4 Set of Differential Equations.....	30
3.5 Numerical Scheme	36
3.6 STRIP3D Results	37
Chapter 4 Two-Dimensional Navier-Stokes Computational Procedure	40
4.1 2D Navier-Stokes Solver.....	40
4.2 2D Near-Wall Formulation.....	42
4.3 2D Computational Procedure.....	44
4.4 2D FENSIE Results	45
Chapter 5 Three-Dimensional Navier-Stokes Computational Procedure.....	47
5.1 3D Navier-Stokes Solver.....	47
5.2 3D Near-Wall Formulation.....	49
5.3 3D Computational Procedure.....	56
5.4 3D FENSIES Results.....	56
Chapter 6 Conclusions and Perspectives	59
References.....	62
Tables.....	68
Figures	73
Vita.....	131

NOMENCLATURE

A	Normalized wall shear stress
C_f	Skin friction coefficient
C_{LW}	Constant in Law of the Wall
C_{mc}	Constant in the expression for the crosswise velocity
C_{zx}	Ratio of 3D eddy viscosity components
h_x, h_z	Metrics of the transformation to non-orthogonal streamline coordinates
H	Height of control volume and location of upper limit of inner strip
k	Turbulent kinetic energy
l_m	Mixing-length
n_j	Normal vector components
p	Pressure
Re_{δ^*}	Reynolds number based on displacement thickness
Re_{δ_1}	Reynolds number based on streamwise displacement thickness
t_i	Traction components
u, v, w	Cartesian velocity components
u_i	Mean velocity components
u_i'	Fluctuating velocity components
u_*	Friction velocity
\bar{U}, \bar{W}	Non-orthogonal streamline velocity components
U, W	Orthogonal streamline velocity components
U_e	Velocity at edge of boundary-layer
U_{mc}	Streamwise velocity at location of maximum crosswise velocity
W_{mc}	Maximum crosswise velocity

x, y, z	Cartesian coordinates
X, Z	Non-orthogonal streamline coordinates
β_w	Wall crossflow angle
δ	Boundary-layer thickness
δ^*	Displacement thickness
δ_1	Streamwise displacement thickness
ε	Turbulent dissipation rate
ϕ	General function
η	Non-dimensionalized normal coordinate
η_H	Location of upper limit of inner strip
η_{mc}	Location of maximum crosswise velocity
κ	Constant in Law of the Wall
λ	Non-orthogonal angle
λ_p	Penalty parameter
μ	Laminar or dynamic viscosity
μ_T	Eddy viscosity
θ	Momentum thickness
ρ	Density
τ	Shear stress
τ_w	Wall shear stress
ω	Specific dissipation rate

LIST OF TABLES

Table 2.1	Primary Classification of Mathematical and Turbulence Models.
Table 2.2	Classification of One-Point Closure Methods Based on the Treatment of Reynolds Stresses.
Table 2.3	Classification of Turbulence Models Using the Boussinesq Assumption.
Table 2.4	Classification of Near Solid Wall Treatments.
Table 2.5	Classification of Numerical Methods.

LIST OF FIGURES

- Figure 2.1 Morphology of Flows.
- Figure 2.2 Clauser Pseudolaminar Velocity Profiles on Defect Law Plot.
- Figure 2.3 Schematic Diagram of Inner Strip in Boundary-Layer.
- Figure 2.4 Flowchart of Computational Procedures for the Reynolds Averaged Navier-Stokes Equations.
- Figure 2.5 Two-Dimensional Control Volume of Finite Height (H) and Infinitesimal Base (dx).
- Figure 2.6 Three-Dimensional Control Volume of Finite Height (H) and Infinitesimal Base (dx by dz).
- Figure 2.7 Johnston Triangular Model on Polar Plot.
- Figure 3.1 Schematic Diagram of Non-Orthogonal Coordinates System.
- Figure 3.2 Comparison of Streamwise Velocity Profiles between the Present Analytical Model and Experimental Measurements for the Van den Berg-Elsenaar Flow at Station 1.
- Figure 3.3 Comparison of Crosswise Velocity Profiles on Polar Plot between the Present Analytical Model and Experimental Measurements for the Van den Berg-Elsenaar Flow at Station 1.
- Figure 3.4 Comparison of Streamwise Velocity Profiles between the Present Analytical Model and Experimental Measurements for the Van den Berg-Elsenaar Flow at Station 6.
- Figure 3.5 Comparison of Crosswise Velocity Profiles on Polar Plot between the Present Analytical Model and Experimental Measurements for the Van den Berg-Elsenaar Flow at Station 6.
- Figure 3.6 Van den Berg-Elsenaar - Computational Domain and Flow Conditions.
- Figure 3.7 Van den Berg-Elsenaar - Skin Friction Coefficient along the Measurement Plane.
- Figure 3.8 Van den Berg-Elsenaar - Wall Crossflow Angle along the Measurement Plane.
- Figure 3.9 Van den Berg-Elsenaar - Boundary-Layer Thickness along the Measurement Plane.
- Figure 3.10 Van den Berg-Elsenaar - Streamwise Displacement Thickness along the Measurement Plane.

- Figure 3.11 Van den Berg-Elsenaar - Influence of the Location of Inner Strip Upper Limit on the Results for the Skin Friction Coefficient along the Measurement Plane.
- Figure 3.12 Van den Berg-Elsenaar - Influence of the Location of Inner Strip Upper Limit on the Results for the Wall Crossflow Angle along the Measurement Plane.
- Figure 3.13 Van den Berg-Elsenaar - Influence of the Location of Inner Strip Upper Limit on the Results for the Boundary-Layer Thickness along the Measurement Plane.
- Figure 3.14 Van den Berg-Elsenaar - Influence of the Location of Inner Strip Upper Limit on the Results for the Streamwise Displacement Thickness along the Measurement Plane.
- Figure 3.15 Müller-Krause - Computational Domain and Flow Conditions.
- Figure 3.16 Müller-Krause - Skin Friction Coefficient along z-axis at $x=0.4$.
- Figure 3.17 Müller-Krause - Wall Crossflow Angle along z-axis at $x=0.4$.
- Figure 3.18 Müller-Krause - Boundary-Layer Thickness along z-axis at $x=0.4$.
- Figure 3.19 Müller-Krause - Streamwise Displacement Thickness along z-axis at $x=0.4$.
- Figure 3.20 Müller-Krause - Skin Friction Coefficient along z-axis at $x=0.6$.
- Figure 3.21 Müller-Krause - Wall Crossflow Angle along z-axis at $x=0.6$.
- Figure 3.22 Müller-Krause - Boundary-Layer Thickness along z-axis at $x=0.6$.
- Figure 3.23 Müller-Krause - Streamwise Displacement Thickness along z-axis at $x=0.6$.
- Figure 3.24 Müller-Krause - Influence of the Location of Inner Strip Upper Limit on the Results for the Skin Friction Coefficient along z-axis at $x=0.4$.
- Figure 3.25 Müller-Krause - Influence of the Location of Inner Strip Upper Limit on the Results for the Wall Crossflow Angle along z-axis at $x=0.4$.
- Figure 3.26 Müller-Krause - Influence of the Location of Inner Strip Upper Limit on the Results for the Skin Friction Coefficient along z-axis at $x=0.6$.
- Figure 3.27 Müller-Krause - Influence of the Location of Inner Strip Upper Limit on the Results for the Wall Crossflow Angle along z-axis at $x=0.6$.
- Figure 3.28 Müller-Krause - Influence of the Eddy Viscosity Ratio on the Results for the Skin Friction Coefficient along z-axis at $x=0.4$.
- Figure 3.29 Müller-Krause - Influence of the Eddy Viscosity Ratio on the Results for the Wall Crossflow Angle along z-axis at $x=0.4$.
- Figure 3.30 Müller-Krause - Influence of the Eddy Viscosity Ratio on the Results for the Skin Friction Coefficient along z-axis at $x=0.6$.
- Figure 3.31 Müller-Krause - Influence of the Eddy Viscosity Ratio on the Results for the Wall Crossflow Angle along z-axis at $x=0.6$.

- Figure 4.1 Wieghardt-Tillmann - Computational Domain, Flow Conditions, and Boundary Conditions.
- Figure 4.2 Wieghardt-Tillmann - Skin Friction Coefficient along the Plate.
- Figure 4.3 Wieghardt-Tillmann - Displacement Thickness along the Plate.
- Figure 4.4 Samuel-Joubert - Computational Domain, Flow Conditions, and Boundary Conditions.
- Figure 4.5 Samuel-Joubert - Skin Friction Coefficient along the Flat Surface.
- Figure 4.6 Samuel-Joubert - Displacement Thickness along the Flat Surface.
- Figure 4.7 Schubauer-Klebanoff - Computational Domain, Flow Conditions, and Boundary Conditions.
- Figure 4.8 Schubauer-Klebanoff - Skin Friction Coefficient along the Body Surface.
- Figure 4.9 Schubauer-Klebanoff - Displacement Thickness along the Body Surface.
- Figure 5.1 Van den Berg-Elsenaar - Computational Domain and Flow Conditions.
- Figure 5.2 Van den Berg-Elsenaar - Skin Friction Coefficient along First and Mid-Streamlines.
- Figure 5.3 Van den Berg-Elsenaar - Wall Crossflow Angle along the First and Mid-Streamlines.
- Figure 5.4 Van den Berg-Elsenaar - Streamwise Displacement Thickness along the First and Mid- Streamlines.
- Figure 5.5 Müller-Krause - Computational Domain and Flow Conditions.
- Figure 5.6 Müller-Krause - Skin Friction Coefficient along z-axis at $x=0.4$.
- Figure 5.7 Müller-Krause - Wall Crossflow Angle along z-axis at $x=0.4$.
- Figure 5.8 Müller-Krause - Streamwise Displacement Thickness along z-axis at $x=0.4$.
- Figure 5.9 Müller-Krause - Skin Friction Coefficient along z-axis at $x=0.6$.
- Figure 5.10 Müller-Krause - Wall Crossflow Angle along z-axis at $x=0.6$.
- Figure 5.11 Müller-Krause - Streamwise Displacement Thickness along z-axis at $x=0.6$.

"Concern for man himself and his fate must always form the chief interest of all technical endeavors . . . in order that the creations of our minds shall be a blessing and not a curse to mankind. Never forget this in the midst of your diagrams and equations."

**Albert Einstein in an address to the students of
the California Institute of Technology**

CHAPTER 1

INTRODUCTION

Engineers and Flow Predictions

One of the tasks faced by aeronautical and naval engineers is to predict the aerodynamic or hydrodynamic characteristics of different devices, such as wings, control surfaces, and propellers, with the objective of improving the overall design. Many reasons give a strong motivation to invest time and energy in seeking new solutions: increasing performance and efficiency (e.g. more thrust with less input power), decreasing the influence of undesirable factors (e.g. reduce vibrations and noise), or even exploring entirely new ways to attain the same goal (e.g. subsonic to supersonic to . . . hypersonic transportation). Each new sought improvement requires new studies and new predictions.

The predictions can be obtained analytically (theoretically), experimentally in laboratories, or numerically by computer simulations. These different approaches have their advantages and limitations, as mentioned by Anderson et al [1] in their introductory remarks. Analytical methods usually give a solution in closed-form making the study of the given parameters straightforward. General conclusions are easily obtained with minimum effort and at low costs, but they are restricted to simple models and simple problems. On the other hand, they can be coupled with numerical methods extending their field of application. Analytical methods are rarely used directly as a design tool but are rather imbedded in computational procedures to obtain preliminary or intermediate results.

Experiments do not require a mathematical model; the fluid "is" and the processes occur "naturally." However, the acquisition of information about the flow characteristics is not trivial. The instrumentation is not always accurate and the measuring devices sometimes induce perturbations in the flow leading to misinterpretation of the measurements. Some characteristics cannot be measured directly but have to be calculated by the intermediate of other sources of data. Furthermore, it is often impractical or even impossible to reproduce certain flow conditions in the testing facilities. Finally, experimental simulations are expensive and there is no prospect for their cost to go down in the near future [2].

With the development of new technology, the performance of computers increases while the cost is reduced, offering the possibility to get cheaper predictions for a wider range of flow conditions without measurement limitations. As early as 1975, the study of Dean R. Chapman, director of Astronautics at NASA Ames Research Center, clearly showed that computers are an indispensable tool in flow simulations [3]. At that time, the rapid increase of computer capabilities, mainly in speed and storage, and the development of new computational methods started to: ". . . bring about a reversal in the traditional roles of computation and experiment in providing simulations of physical phenomena" [3]. This trend continued over the years, and computer simulations are now a major part of the design process [4,5].

Even if experiments are not viewed anymore as the main ingredient in the design process, they are still important as a research tool [6], especially for the development of turbulence models. The experimental investigation of basic flows sheds some light on new problems helping the development of improved computational methods. Therefore, our overall concern should be focus on exploring new practical ways to use the computer for flow simulations, based on the information available from existing experiments and analyses.

Computers and Turbulent Flows

For most practical applications, the flow is mainly turbulent, and the nature of a turbulent flow is more complex than the nature of a laminar flow [7-9]. The motion of fluid particles is swirling with random and irregular fluctuations. The swirling fluid particles are called eddies, and their size spans several orders of magnitude. The different processes, i.e. convection, diffusion, etc., are also more complex than for a laminar flow. A turbulent flow is inherently unsteady and three-dimensional (3D), and it is generally accepted that the unsteady 3D Navier-Stokes equations are a valid mathematical model to represent the turbulent motion of fluid particles.

But, flow simulations using this mathematical model are still problematic because of limitations in present computer capabilities. Even in this era of supercomputers and massive parallelism [10-12], it is still not possible to solve the previous set of equations along with the continuity equation for practical configurations by Direct Numerical Simulation [13,14]. The refinement of the grid must be such that it captures the motion of the smallest eddies. If not, part of the physics is not simulated, and the predictions become inaccurate. Some attempts have also been made to solve turbulent flows by resolving directly the motion of the larger

eddies while modeling the smaller ones. These methods are part of a class called Large Eddy Simulation (LES) and use sub-grid scale models [14,15]. The LES methods are also restricted to simple flows, e.g. homogeneous flows, because of computer limitations.

The most common approach to overcome this problem is to divide the motion into mean and fluctuating components, and to average each term in the equations with respect to time. The resulting equations are called Reynolds Averaged Navier-Stokes equations. They have the same form as the original Navier-Stokes equations, except for supplementary terms due to the transport of momentum by the fluctuating components. These terms act like stresses on the fluid and are thus called "apparent" stresses or Reynolds stresses. The next step consists in finding new algebraic and/or differential equations to solve for these quantities along with the mean velocity components and the pressure; this is known as the closure problem.

The presence of fluctuations in a turbulent flow not only changes the nature of the motion of the fluid particles, it also shifts the problem in the analysis. Because of the presence of the Reynolds stresses in the equations of motion, one must now talk about turbulence modeling. Another problem becomes apparent when examining the empirical information. A very small region adjacent to the wall surface shows a high velocity gradient and more important viscous effects. The treatment of the near-wall region (also called the inner region of the boundary-layer) is an integral part of turbulence modeling. The type of approach used to model the Reynolds stresses influences the treatment of the wall region and vice-versa. The choice of turbulence modeling has the highest impact on the quality of the predictions and on the practicality of the computer method.

Classification and Objectives

During the years of research and development in turbulent flow applications, a large number of technical works were published by numerous scientists from all over the world. Furthermore, many new experiments were designed to achieve a better understanding of the fundamental characteristics of turbulent flows in practical cases. The number of communications increased rapidly, and it became difficult to collect all the data, to analyze ideas and results, and to draw pertinent conclusions from all these analyses.

In 1968, a conference on the computation of turbulent boundary-layers was organized at Stanford university and sponsored by the AFOSR in order to assess the state-of-the-art in

turbulence modeling and to evaluate the various numerical methods using benchmark experiments [16]. A paper by Reynolds [17] provided an outline of the main factors to be considered for the classification and evaluation of turbulence models and numerical methods. This conference was a great success, and the information gathered by the organizers was seen as the standard reference for new developments until the following Stanford conference which took place in 1980-81 [18]. At that time, an updated overview of the latest developments in turbulent flow computations was prepared by Ferziger, Bardina, and Allen [19]. The initial morphology of prediction methods was expanded, and the new classification included a morphology of the flows, a morphology of the turbulence models (and mathematical models), and a morphology of the numerical methods.

The Stanford conferences dealt mainly with two-dimensional (2D) turbulent flows, but a survey of three-dimensional (3D) turbulent boundary-layer experiments was undertaken for that meeting by Humphreys and van den Berg [20]. This preliminary study was followed in 1982 by a EUROVISC workshop in Berlin [21], where experimental measurements and numerical predictions were presented and discussed with the same objectives as for the previous two meetings. Therefore, the proceedings of the Stanford conferences and EUROVISC workshop provide the set of "developer's tools" necessary to design new computational procedures by giving access to a "library" of existing turbulence models and numerical methods, and to a large database of flow experiments and numerical results for the validation of new predictions.

The objective of the present work is to introduce new computational procedures to simulate incompressible wall-bounded turbulent flows in or about two-dimensional or three-dimensional geometries, using the above-mentioned sources as main references. The ideas and concepts are presented in Chapter 2 within the perspective of the morphology proposed at the 1981 meeting. The different approaches are globally introduced with respect to existing models and methods, and the mathematical background is established in order to prepare the presentation of the developments for each of the three simulation procedures.

First, a three-dimensional integral method was developed as an extension of the 2D strip-integral method presented by Moses [22] at the 1968 Stanford conference. The application of the strip-integral concept to incompressible flow problems proves to be a more natural way to introduce the physics in the mathematical model, when compared to the conventional integral methods. The strip-integral method does not depend as much on correlations, and there is no need for empirical relationships for the entrainment coefficient, the

skin friction coefficient, or any other coefficients or functions. The turbulence modeling is completely "open" as in differential methods [23]. The mathematical developments and the validation of the predictions of the STRIP3D integral method are presented in Chapter 3.

Two computational procedures have also been designed to solve the Reynolds Averaged Navier-Stokes equations by the Finite Element method for two- and three-dimensional flow problems respectively [24]. The flow is solved down to the wall with a slip velocity following Clauser's idea of pseudolaminar velocity profile [25]. The wall shear stress is imposed as boundary condition for the Navier-Stokes solution, and corrected values are obtained by enforcing the conservation principles over a small strip in the inner region of the boundary-layer. The strip-integral method is also used in these procedures but under a 1-strip-integral formulation. The turbulence modeling is provided through an algebraic equation for the eddy viscosity in the outer region. The description and validation of the 2D computational procedure called FENSIE can be found in Chapter 4, while the 3D computational procedure called FENSIES is introduced in Chapter 5.

All numerical predictions are compared with the experimental measurements of benchmark test cases. The 2D results are validated for three cases: the Wieghardt-Tillman flow over a flat plate; the Samuel-Joubert flow over a flat surface with a moderate adverse-pressure gradient; and the Schubauer-Klebanoff flow about an airfoil-like body with a strong adverse-pressure gradient. The 3D results are validated using two experiments: the Van den berg-Elsenaar flow over a flat surface with a 35° sweep angle under infinite swept-wing conditions in an adverse-pressure gradient; and the Müller-Krause flow over a flat surface with an adverse-pressure gradient in the streamwise direction and an induced pressure gradient in the crosswise direction. The present methods prove to be efficient and practical tools for the simulation of incompressible wall-bounded turbulent flows.

CHAPTER 2

IDEAS, CONCEPTS, AND MORPHOLOGY

The 1968 and 1980-81 Stanford conferences, and the 1982 EUROVISC workshop marked major points in time when the scientific community gathered in order to assess the state-of-the-art in turbulence modeling and computational methods for turbulent flows. In 1981, a classification was proposed to evaluate and compare the different models and methods through a morphology of the flows, a morphology of the turbulence models (and mathematical models), and a morphology of the numerical methods [19]. This document is still seen as a standard reference and it provides helpful guidelines for the comparative description of new developments in turbulent flow analysis. The main ideas and concepts behind the present computational procedures are elaborated in the next sections following the classification proposed for the 1981 meeting and, when necessary, amendments to the original morphology are introduced and discussed.

2.1 Morphology of Flows

The proposed classification is reproduced in Figure 2.1. The classification scheme depends on the state of the fluid, the flow conditions, and the physical environment of the flow. As can be observed, the following factors are considered:

Homogeneous	Inhomogeneous
Incompressible	Compressible
Free-shear flow	Wall-bounded flow
"Simple" strains	"Extra" effects
External flow	Internal flow
Attached flow	Separated flow
Mixing layer	Wake
Near-field	Far-field
Transonic	Supersonic

The applications and the range of applicability considered in the present work lead to the following choices:

Inhomogeneous
 Incompressible
 Wall-bounded flow
 "Simple" strains and "Extra" effects
 External and Internal flows
 Attached flow

For practical cases, the flow is inhomogeneous, which means that the statistical state of the fluid at a given time varies in space. The applicability is limited to incompressible wall-bounded turbulent flows with either "simple" strains as for flows over flat surfaces, or "extra" effects as for flows over walls with curvature like an airfoil section or a wing. The present methods are also applicable to external and internal flows in regions where there is no separation (attached flows).

This range of applicability is valid for flows in or about two-dimensional (2D) and three-dimensional (3D) geometries. Another restriction must however be added for full 3D cases: the case of flow reversal. An example is the flow about a cylindrical body standing perpendicularly over a flat surface [26]. The fluid particles in the boundary-layer developing on the flat surface deviate from the main flow direction under the induced pressure gradient created by the body, producing a crosswise velocity relative to the external streamlines. The crosswise velocity profile is of bell-shaped type with a maximum crosswise velocity in the boundary-layer. With the fluid going around the body, the main flow is brought back to the original direction and some fluid particles move in the reverse crosswise direction under the inverse induced pressure gradient. Thus, this flow reversal causes an S-shaped crosswise velocity profile in some regions of the flow. This case is outside the range of applicability of the present integral method.

2.2 Morphology of Mathematical and Turbulence Models

The primary classification of the mathematical and turbulence models is reproduced in Table 2.1. Level 1 represents methods depending only on empirical information and correlations with experimental measurements. Level 2 represents integral methods in which the turbulence modeling is done through empirical relations for the skin friction coefficient, the entrainment coefficient, or other coefficients and functions. Levels 3 to 6 are different types of turbulence modeling for differential equations. In the proposed morphology, a secondary classification is then presented for Levels 2, 3, and 4.

Here the classification is rather extended and discussed for two categories: the category of differential equations making use of Level 3 models; and the category of integral equations, which includes Level 2 methods and some of the Level 3 turbulence models. The models at Levels 4, 5 and 6 are not included in the discussion. The Two-point Closure models (Level 4), which are based on spectral theories of turbulence, the Large Eddy Simulation [15] (Level 5), and the Full (or Direct) Simulation [13] (Level 6) are currently restricted to simple flows. These methods are of fundamental interest, but are not considered as practical engineering tools at the present time.

Differential Equations

The unsteady three-dimensional form of the Navier-Stokes equations is generally accepted as a valid mathematical model to represent the turbulent motion of fluid particles. The motion of the fluid is swirling with random and irregular fluctuations, and the size of the eddies spans several orders of magnitude, the smallest being about 10^{-3} times the characteristic size of the flow domain [1]. The velocity fluctuations of the particles also span a wide range of frequencies [9]. The requirements in computer capabilities, processing speed and storage, are such that today's supercomputers can only be used for simple flows, e. g. homogeneous flows, because of the fine mesh and time step required.

The most common approach to overcome this problem is to divide the motion into mean and fluctuating components, and to average each term in the equations with respect to time. This decomposition is due to Reynolds and the new form of the equations for the mean quantities is called the Reynolds Averaged Navier-Stokes equations. Assuming steady flow in the mean, the continuity equation and the momentum equations in tensor notation are written as:

$$u_{i,i} = 0 \quad (2.1)$$

$$\rho u_j u_{i,j} = -p_{,i} + [\mu (u_{i,j} + u_{j,i}) - \rho \overline{u'_i u'_j}]_{,j} \quad (2.2)$$

where ρ is the density, u_i are the mean velocity components, u'_i are the fluctuating velocity components, p is the mean pressure, and μ is the laminar viscosity. Equations (2.2) have the same form as the Navier-Stokes equations except for the last term of the right-hand side. These supplementary terms are due to the transport of momentum by the fluctuating components.

Because this last term appears as a viscous term, it is seen as a representation of "apparent" stresses, also known as Reynolds stresses.

In order to solve the system of equations, the Reynolds stresses must be related to the mean flow quantities throughout algebraic and/or differential equations. The turbulence modeling is then classified as Level 3 and refers to one-point closure methods. The classification of one-point closure methods is presented in Table 2.2. The Boussinesq class of models is based on the Boussinesq assumption, which states that the Reynolds stresses are proportional to the mean strain rates:

$$-\rho \overline{u'_i u'_j} = \mu_T (u_{i,j} + u_{j,i}) \quad (2.3)$$

where μ_T is the turbulent viscosity, also known as eddy viscosity. The closure problem is then translated to finding an appropriate model for the eddy viscosity. This approach is the most popular by far, and numerous models ranging from extremely simple to highly complex have been developed in the past.

The other classes of one-point closures include the Algebraic, Differential, and Reynolds-stress models. All three classes assume that the Reynolds stresses are not proportional to the mean strain rates. For the Algebraic models, the Reynolds stresses are approximated by algebraic equations, while a system of differential equations is solved for the two other classes. The Reynolds-stress models use one equation for each relevant Reynolds stress, while a smaller number of equations than the relevant stress components is used for the Differential models.

A sub-classification was established for the Boussinesq models and a reproduction is shown in Table 2.3. These models are often labeled considering the type and number of equations. The labeling system is also included in the right column of Table 2.3. Algebraic equations are not counted as equations but are rather taken as ways to prescribe either the eddy viscosity or the mixing length (l_m). Ordinary differential equations (ODE) are counted as half equations while partial differential equations (PDE) are considered as full equations. Turbulence models using prescribed values for the eddy viscosity are called zero-equation models or algebraic eddy viscosity models. A half-equation model uses an ODE to represent the mixing length, which appears explicitly in the eddy viscosity relation. One-equation models, also known as TKE models, use a PDE derived from the conservation of energy for the

fluctuations and solved for the turbulent kinetic energy (k). If the mixing length is obtained through an ODE, the models are then known as one-and-a-half equation models. The last class uses a set of two partial differential equations for two quantities chosen among the turbulent kinetic energy, the mixing length, or a combination of the first two of the form $k^a l_m^b$. A popular choice is the turbulent dissipation rate

$$\varepsilon = \frac{C k^{3/2}}{l_m} \quad (2.4)$$

Another is the specific dissipation rate (ω), and a third one is $k^2 l_m$. The usual combinations are presented in Table 2.3. For all these formulations, the closure problem remains to find an approximate representation for the diffusion, production, and dissipation terms of the PDE's in relation with the turbulent kinetic energy, the mixing length, the new combined quantities, and the mean flow quantities.

The Navier-Stokes computational procedures proposed in this work utilize a prescribed eddy viscosity model combined with a new treatment for the near-wall region. This new wall treatment can be implemented in other types of formulations, but it is appropriate to first validate a new concept in the simplest formulations. Also, algebraic eddy viscosity models, although conceptually simple, have been found adequate for flows near equilibrium pressure gradient conditions [16]. It was previously mentioned that the treatment of the wall region is as important as the treatment of the Reynolds stresses and therefore, it is especially important to verify the extent of applicability of a simple eddy viscosity model for a particular treatment of the wall.

The present treatment of the near-wall region is based on an extension of an original idea of Clauser [25]. In the analysis of turbulent boundary-layer with emphasis on the outer region, Clauser observed that the velocity profile seems to intersect the wall with a non-zero velocity and that the eddy viscosity remains almost constant across the outer region. Based on these observations, he reduced the momentum equation for the turbulent boundary-layer over a flat plate to the equation of Blasius for laminar flow assuming a pseudolaminar velocity profile with a slip velocity at the wall. After rescaling the coordinates and matching experimental data on a defect law plot (see Fig. 2.2), he obtained the following relation for the eddy viscosity, which is known as the Clauser outer region eddy viscosity model:

$$\mu_T = C \rho U_e \delta^* \quad (2.5)$$

where ρ is the density, U_e is the edge velocity, δ^* is the displacement thickness, and C is a constant that Clauser found to be $C=0.018$ for the flat-plate problem. The analysis was extended to include flows with equilibrium pressure gradient, and the same form of equation was found adequate, except that other researchers judged that $C=0.0168$ was a better choice for all types of flow [9].

This model is valid only for the outer region. Other models have been developed for the inner region to represent the eddy viscosity which decreases in magnitude from its outer region constant value to zero at the wall. The analysis of the inner region is more complex due to the high and rapidly changing velocity gradients and the presence of the laminar sub-layer. This makes the treatment of the wall region an important part of turbulence modeling.

Table 2.4 shows the classification of existing types of treatment near solid walls. The first approach solves the flow down to the wall assuming no-slip velocity. A multi-layer eddy viscosity is required over the entire boundary-layer and a very fine mesh must be used to get accurate predictions for the wall shear stress. This leads to large requirements in computer storage and processing speed making this approach impractical for 3D flow analyses. A method was proposed by Schetz and Favin [27] to reduce the mesh requirements near the wall. The method also solves the flow down to the wall using a no-slip condition, but the wall shear stress is evaluated by matching the calculated velocity derivative at a point away from the wall with the velocity derivative from the Law of the Wall. The predictions of the wall shear stress are accurate with a coarser mesh. The second approach solves the flow down to a point located above the wall where the velocity is calculated using the Law of the Wall. These methods are often referred to as wall-function methods [28]. The eddy viscosity is thus not required below the point where the wall function is applied. This approach also alleviates the mesh requirements, which is useful especially for 3D flows. However, the imposition of the velocity or its derivative at a fixed point using an empirical relation proves to be constraining and inaccurate for flows outside the range of validity of the Law of the Wall, which is well documented only for 2D flows over smooth, solid surfaces.

The present approach for the treatment of the near-wall region uses the idea of a pseudolaminar velocity profile. The flow is solved down to the wall assuming a slip velocity, and the wall shear stress is imposed as a boundary condition. The Reynolds Averaged Navier-Stokes equations with the wall shear stress boundary condition can be viewed as solving the flow in the outer region of the boundary-layer. Two advantages are apparent from this

approach: first, an eddy viscosity model is required only for the outer region, which simplifies greatly the turbulence modeling; second, a relatively coarse mesh can be used, resulting in computational savings and making the method practical for 3D flows. The wall shear stress is obtained by enforcement of conservation of mass and momentum in an integral sense over a thin strip in the near-wall region (see Fig. 2.3). Interaction between the Navier-Stokes formulation and the inner strip formulation is done through the wall shear stress, the displacement thickness, and the velocity and shear stress at the upper limit of the inner strip (see Fig. 2.4). The physics of the flow is better represented by enforcing conservation of mass and momentum over a thin strip than by matching the velocity or the velocity derivative at a fixed point above the wall as in wall function methods.

The inner strip formulation is obtained by the strip-integral method. The discussion of the formulation will be presented after the review of the methods for integral equations, which includes the strip-integral method.

Integral Equations

The classification of the methods for integral equations is based on the additional equation used in combination with the momentum integral equation for 2D analyses or with the two momentum integral equations for 3D analyses. One of the three following equations is used:

- 1- Energy integral equation
- 2- Moment of momentum equation
- 3- Entrainment equation

The choice of the additional equation influences the type of correlations necessary to "close" the model [29]. In most cases, the skin friction coefficient is modeled by a skin friction law, such as the Ludwig-Tillmann relation or Green's formula, and more empiricism must be included through correlations for the shape parameter, the entrainment coefficient, or the viscous dissipation function.

In conventional integral equations, the effects of turbulence are not included explicitly in the formulation but are rather imbedded in the empirical relations. As stated by Humphreys and Lindhout, the turbulence modeling tends to be "hidden in opaque correlations" [30]. This situation justifies the proposed morphology of turbulence models, which classifies the integral

methods as one level of turbulence models. However, it is somehow restrictive to include the form of the basic equations of motion in the classification of turbulence models. The turbulence modeling depends directly on the mathematical model, but it is important to remember that a turbulence model is not only restricted to just one form of equations. An example of this distinction can be found with the strip-integral method.

The strip-integral method is a particular case of the Method of Weighted Residuals [31]. It has been applied to laminar boundary-layers by Pallone [32], and to two-dimensional incompressible turbulent boundary-layers by Moses [22]. The strip-integral method uses the momentum integral equation defined over as many control volumes as there are unknown parameters to be evaluated.

For a two-dimensional analysis, the conservation of mass and momentum is applied to a control volume of finite height (H) and infinitesimal base (dx) as shown in Figure 2.5 leading to the following general integral equation:

$$\frac{d}{dx} \int_0^H u^2 dy - u_H \frac{d}{dx} \int_0^H u dy = -\frac{H}{\rho} \frac{dp}{dx} + \frac{\tau_H - \tau_w}{\rho} \quad (2.6)$$

where u is the velocity, u_H and τ_H are respectively the velocity and the shear stress at the upper limit of the control volume, and τ_w is the wall shear stress. If the height of the control volume is taken as the boundary-layer thickness (δ), the equation becomes:

$$\frac{d}{dx} \int_0^\delta u^2 dy - U_\theta \frac{d}{dx} \int_0^\delta u dy = -\frac{\delta}{\rho} \frac{dp}{dx} - \frac{\tau_w}{\rho} \quad (2.7)$$

where U_θ is the velocity at the edge of the boundary-layer. The integrals of the velocity are left in the last equation instead of replacing them by use of the definitions of the displacement thickness (δ^*) and momentum thickness (θ):

$$\delta^* = \int_0^\delta \left(1 - \frac{u}{U_\theta}\right) dy \quad (2.8a)$$

$$\theta = \int_0^\delta \frac{u}{U_\theta} \left(1 - \frac{u}{U_\theta}\right) dy \quad (2.8b)$$

The transformation of equation (2.7) using the definitions of δ^* and θ , and using Bernoulli equation for the pressure gradient would give the famous Von Karman equation used by most integral methods [29].

Assuming that the edge velocity distribution is known, the only unknowns in equation (2.7) are the velocity function $u(y)$, the boundary-layer thickness, and the wall shear stress. The velocity function can be approximated by the Law of the Wake, a parametrized velocity profile depending on three parameters: the edge velocity, the skin friction coefficient (C_f), and the boundary-layer thickness. Thus, the velocity function assumes the following form:

$$u = u(y, U_e, C_f, \delta) \quad (2.9)$$

Knowing that

$$\tau_w = \frac{C_f}{2} \rho U_e^2 \quad (2.10)$$

the only remaining unknown parameters are C_f and δ . An additional equation is then required to solve for the two unknowns. Using equation (2.6) for a control volume extending from the wall to an arbitrary location inside the boundary-layer, an additional momentum integral equation for an inner strip over the wall is then obtained as a second equation. The same parametrized velocity profile can be used in the integrals, and the shear stress at the upper limit of the inner strip (τ_{ij}) is the only term remaining to be determined. Therefore, the closure problem is now reduced to finding a model for the turbulent shear stress as in differential methods, except that the turbulent shear stress needs to be modeled only along a single line at the upper limit of the inner strip.

Therefore, compared to conventional integral methods, the strip-integral method shows many advantages. First, the entrainment equation, the energy integral equation, or the moment of momentum equation is not required. Second, no empirical relations are required for the skin friction coefficient, the shape parameter, or any other coefficients. Third, empirical information is included through the parametrized velocity profile, but the integration of the velocity tends to diminish the effects of modeling errors. And finally, the turbulence modeling is completely "open" as for differential methods.

For his work, Moses used the Boussinesq assumption to represent the shear stress. The derivative of the velocity at the upper limit of the inner strip was obtained using the

parametrized velocity profile, and an algebraic outer region model was chosen to model the eddy viscosity. As mentioned above, the location of the upper limit of the inner strip is arbitrary and it can be set in the lower part of the outer region making the turbulence model quite simple to implement. The set of two first-order ordinary differential equations is solved for the two unknown parameters C_f and δ . This method was applied on the selection of flows chosen for the 1968 Stanford conference and performed very well, even compared to differential methods and even though a simple turbulence model was used in the strip-integral method. The applicability of the strip-integral method can be extended to include higher-order turbulence models following an analysis similar to the one for differential methods.

The strip-integral method can also be extended to three-dimensional turbulent boundary-layer analysis. The conservation of mass and the conservation of momentum in the x and z directions are applied to a control volume of finite height (H) and infinitesimal base (dx by dz) as shown in Figure 2.6 giving the following integral equations in Cartesian coordinates:

$$\frac{\partial}{\partial x} \int_0^H u^2 dy + \frac{\partial}{\partial z} \int_0^H u w dy - u_H \left[\frac{\partial}{\partial x} \int_0^H u dy + \frac{\partial}{\partial z} \int_0^H w dy \right] = -\frac{H}{\rho} \frac{\partial p}{\partial x} + \frac{(\tau_{xH} - \tau_{xw})}{\rho} \quad (2.11a)$$

$$\frac{\partial}{\partial z} \int_0^H w^2 dy + \frac{\partial}{\partial x} \int_0^H u w dy - w_H \left[\frac{\partial}{\partial x} \int_0^H u dy + \frac{\partial}{\partial z} \int_0^H w dy \right] = -\frac{H}{\rho} \frac{\partial p}{\partial z} + \frac{(\tau_{zH} - \tau_{zw})}{\rho} \quad (2.11b)$$

where u is the velocity component in the x direction, w is the velocity component in the z direction, u_H and w_H are the velocity components at the upper limit of the control volume, τ_{xH} and τ_{zH} are the shear stress components at the upper limit of the control volume, and τ_{xw} and τ_{zw} are the wall shear stress components. These equations are also established for 2 strips; one extending from the wall to the edge of the boundary-layer, and the other extending from the wall to a location in the overlap region. A set of four equations is then available for the 3D analysis.

The formulation depends primarily on the parametrization of the velocity profile. The usual way to express the 3D velocity components is by streamline orthogonal coordinates [33], leading to a streamwise velocity profile, $U(y)$, and a crosswise velocity profile, $W(y)$. Based on the conclusions of the excellent review of three-dimensional Laws of the Wall by Ölçmen and Simpson [34,35], it was decided to use a new Law of the Wake based on the Johnston Law of the Wall [36] with the Moses wake function [22] in the streamwise direction, and the Johnston

triangular model (see polar plot, Fig. 2.7) for the crosswise velocity. The streamwise velocity depends on the usual parameters and assumes the general form

$$U = U(y, U_e, C_f, \beta_w, \delta) \quad (2.12)$$

where β_w is the wall crossflow angle. The crosswise velocity depends on the streamwise velocity, the edge velocity, the wall crossflow angle, and a factor defining the slope of the straight line in region II of the polar plot:

$$\begin{aligned} W &= U \tan\beta_w && \text{for } \eta < \eta_{mc} \\ W &= C_{mc} (U_e - U) && \text{for } \eta > \eta_{mc} \end{aligned} \quad (2.13)$$

with
$$C_{mc} = \frac{W_{mc}}{U_e - U_{mc}}$$

where η is the normal coordinate (y) normalized with respect to the boundary-layer thickness, and η_{mc} is the location of maximum crosswise velocity, which becomes an additional parameter in the formulation. Thus, the crosswise velocity assumes the general form

$$W = W(y, U_e, C_f, \beta_w, \delta, \eta_{mc}) \quad (2.14)$$

Here again, assuming that the edge velocity distribution is known and using Bernoulli equation for the pressure gradients, plus knowing the fact that the velocity and shear stress components in Cartesian coordinates can be found from the velocities and shear stresses expressed in streamline orthogonal coordinates, the remaining unknowns are the four parameters in equations (2.12) and (2.14), and the turbulent shear stresses at the upper limit of the inner strip. These shear stresses are also modeled using the Boussinesq assumption, and they are determined using an algebraic eddy viscosity model and the velocity derivatives evaluated from the parameterized velocity profiles. The streamwise and crosswise velocity profiles form a practical 4-parameter family, the four parameters being: the boundary-layer thickness, the skin friction coefficient, the wall crossflow angle, and the location of maximum crosswise velocity. Therefore, the set of four equations is solved for four unknowns. The complete details of the formulation are presented in Chapter 3.

Near-Wall Integral Formulation

The treatment of the near-wall region is based on the application of the conservation principles over a thin strip extending from the wall to a location in the overlap region of the boundary-layer. For a two-dimensional analysis, the strip-integral equation is represented by equation (2.6) in which H is the location of the upper limit of the inner strip. The velocity needs to be approximated exclusively over the inner region contrarily to a full boundary-layer analysis. Therefore, the Law of the Wall is a suitable representation for the velocity profile. The Law of the Wall in the overlap or logarithmic region is usually written as:

$$\frac{u}{u_*} = \frac{1}{\kappa} \ln\left(\frac{\rho u_* y}{\mu}\right) + C \quad (2.15)$$

where u_* is the friction velocity, and κ and C are constants. Choosing the displacement thickness (δ^*) as characteristic dimension, equation (2.15) can be rewritten as:

$$\frac{u}{U_e} = A \ln(C_{LW} A Re_{\delta^*} \eta) \quad (2.16)$$

where η is the transverse coordinate normalized with respect to the displacement thickness, Re_{δ^*} is the Reynolds number based on the displacement thickness, A is a normalized form of the wall shear stress, and C_{LW} is a constant. The velocity profile thus assumes the general form:

$$u = u(y, U_e, C_f, \delta^*) \quad (2.17)$$

Introducing the velocity profile in equation (2.6), the remaining unknowns are then U_e , C_f , δ^* , the pressure gradient, and the velocity and shear stress at the upper limit of the inner strip. The values of all these variables are provided by the Navier-Stokes solution for the whole layer, except for the skin friction coefficient which is imposed as a boundary condition. Therefore, the integral equation is used to calculate the corrected skin friction coefficient distribution that will be used at the following iteration until convergence is reached.

A similar development is performed for a three-dimensional analysis. The strip-integral equations are represented by equations (2.11a) and (2.11b) in which H is the location of the upper limit of the inner strip. Here also the Johnston Law of the Wall is a suitable representation for the velocity profile, which assumes the general form:

$$U = U(y, U_e, C_f, \beta_w, \delta_1) \quad (2.18a)$$

$$W = W(y, U_\theta, C_f, \beta_w, \delta_1, \eta_{mc}) \quad (2.18b)$$

where δ_1 is the streamwise displacement thickness, which is used as characteristic dimension for 3D flows, and η_{mc} is now normalized with respect to δ_1 .

Introducing the velocity profile in equations (2.11a) and (2.11b), the unknowns are then U_θ , C_f , β_w , δ_1 , η_{mc} , the pressure gradient, and the velocity and shear stress components at the upper limit of the inner strip. The values of all these variables are provided by the Navier-Stokes solution, except for the skin friction coefficient and the wall crossflow angle, which give the wall shear stress imposed as boundary condition. Therefore, the set of two integral equations is used to calculate the corrected skin friction coefficient and wall crossflow angle distributions that will be used at the following iteration until convergence is reached.

The resolution of the integral equations and the Reynolds Averaged Navier-Stokes equations is done by different classes of numerical methods. The comparative description is presented in the next section.

2.3 Morphology of Numerical Methods

The classification of numerical methods is divided in two categories as shown in Table 2.5. The first category is related to the discretization of the equations, and the second to the solution technique. The discussion about a numerical method depends on the form of the basic equations. Two forms are employed in the present work: first-order differential equations for the 2-strip-integral and the 1-strip-integral formulations; and the Reynolds Averaged Navier-Stokes equations, which are second-order partial differential equations.

Strip-Integral Equations

The morphology applies mainly to differential equations, and the proposed sub-classification is not adapted to the discussion of numerical methods for integral equations. First-order differential equations assume the propagation of information "signals" from one end of the domain, where the dependent variables are known, towards the other end. For equations with one independent variable like the 2D 1-strip-integral equation, the dependent variables are known at an initial point, and the solution is calculated along the line defined by the independent variable. For equations with two independent variables such as in the 3D strip-integral formulations, the dependent variables must be known along two lines intersecting at

one point in space, and the solution is sought for the domain included between these two lines. Therefore, a natural numerical scheme is obtained by a marching solution technique using an approximation of the first-order derivatives by backward difference with respect to the point of the domain where the dependent variables are to be calculated.

The most popular marching schemes belong to the Runge-Kutta family [37]. For the present work, the second-order Runge-Kutta method was chosen because of its easy implementation and sufficient accuracy. Fourth-order Runge-Kutta methods provide a higher accuracy, which is not necessary here because of the limited precision of the known parameters and the relatively small number of calculation steps.

The 2D 1-strip-integral formulation gives one ordinary differential equation of the following form:

$$\frac{d\phi}{dx} = f(x, \phi) \quad (2.19)$$

where ϕ is the dependent variable and x is the independent variable along the line of integration. The Runge-Kutta method is thus expressed as:

$$\phi_i^* = \phi_{i-1} + \Delta x f(x_{i-1}, \phi_{i-1}) \quad (2.20a)$$

$$\phi_i = \phi_{i-1} + 0.5 \Delta x \{ f(x_{i-1}, \phi_{i-1}) + f(x_i, \phi_i^*) \} \quad (2.20b)$$

Assuming ϕ_0 known at $x=x_0$, the function ϕ is evaluated at each successive step x_i along the line of integration.

For the 3D strip-integral formulations, a set of partial differential equations is obtained:

$$\sum_k C^{*k} \frac{\partial \phi^k}{\partial x} = f(X, Z, \phi^l, \phi^m) \quad l=1,N \quad m=1,N \quad m \neq l \quad (2.21)$$

where ϕ^k are the dependent variables, X and Z are the independent variables defining the mesh, and N is the number of dependent variables in the equations. The first part of the integration of the Runge-Kutta method is written as:

$$\sum C^{lk} \phi_i^{k*} = \sum C^{lk} \phi_{i-1}^k + \Delta x f^l(X_{i-1}, Z_{i-1}, \phi_{i-1}^l, \phi_{i-1}^m) \quad (2.22a)$$

This linear set of N algebraic equations is solved by Gauss elimination, giving the intermediate solution for all ϕ_i^k at (X_i, Z_i) . The second part of the integration then becomes:

$$\sum C^k \phi_i^k = \sum C^k \phi_{i-1}^k + 0.5 \Delta x \{ f^l(X_{i-1}, Z_{i-1}, \phi_{i-1}^l, \phi_{i-1}^m) + f^l(X_i, Z_i, \phi_i^l, \phi_i^m) \} \quad (2.22b)$$

This linear set of N algebraic equations is also solved by Gauss elimination, and the numerically "exact" values of ϕ_i^k are now known at (X_i, Z_i) . The solution is first computed for all nodes along the first streamline adjacent to the limiting external streamline where the values of the dependent variables are known, and then for the following streamlines until the end of the domain is reached. The Courant-Friedrichs-Levi (CFL) condition must always be satisfied, which means that $\Delta X = X_{i,j} - X_{i-1,j}$ must be small enough for the domain of influence to be included between two adjacent external streamlines separated by a distance $\Delta Z = Z_{i-1,j} - Z_{i-1,j-1}$.

Reynolds Averaged Navier-Stokes Equations

As mentioned above, the categorization of a numerical method is discussed with respect to the discretization and the solution technique. The discretization is the process of transforming the derivatives into finite differences and the continuous space into a grid of nodes where the dependent variables are to be evaluated. Three general types of method exist for differential equations: the Finite Difference method, the Finite Volume method, and the Finite Element method.

The Finite Difference method performs the finite differentiation directly on the derivatives of the differential equations. The finite difference equations are written for each node of the discretized domain, and special cases arise near the boundaries where the derivatives must be approximated using other differencing schemes depending on the boundary conditions. For a physical domain with curved or non-aligned boundaries, a transformation of the coordinates system must be performed in order to obtain a regular computational domain. Many mapping methods exist either algebraic or differential, and the most popular methods are based on the work of Thompson [38], which uses the solution of partial differential equations of the Poisson type to obtain boundary-fitted coordinates. The disadvantage of this approach is that the differential equations must be written in the new coordinates system, making the formulation mathematically more complex.

The Finite Volume method uses the conservation principles (mass and momentum, plus energy when required) applied to small control volumes to obtain the equations written in

integral form. The computational domain is constructed by the assembly of the small "blocks" together to fit the entire physical domain. The integral equations are discretized, and the velocity components are evaluated at the nodes, while the shear stresses can be specified along the edges of the control volumes of the boundaries of the domain.

The Finite Element method is a generalization of traditional variational methods [39]. The differential equations are transformed using a variational method which seeks the function that minimizes the quadratic functional. The classical variational methods seeks an exact solution of this function, which cannot be obtained for the Navier-Stokes equations. The Galerkin technique uses approximate functions, which are a linear combination of values of the dependent variables. The domain is represented as a collection of sub-domains of geometrically simple shape, called finite elements. Each element is composed of a set of nodes where the solution is evaluated, and the approximate functions are chosen as polynomials with the coefficients being the unknown values of the dependent variables at the nodes. The assembly of the elements gives a set of non-linear algebraic equations to be solved simultaneously by Gauss elimination after integration of the boundary conditions. The variational formulation of the Finite Element method for flow problems leads to two types of boundary conditions: essential when values for the velocity components are specified; and natural when values for the shear stresses are imposed along a boundary.

For the present work, the Finite Element method (FEM) was chosen because of the advantages related to the geometrical modeling and to the implementation of the boundary conditions. The Finite Element method has been studied extensively in the past, and many good references offer a complete description of the mathematical developments [39,40,41]. A brief overview of the formulation employed in this work is presented in the next paragraphs. The reader interested in learning more about the basic concepts of the Finite Element method is invited to consult the above-mentioned references.

The present implementation of the FEM uses a penalty function to enforce the continuity equation constraint through the pressure term [42,43]. The continuity equation is written as:

$$u_{i,j} = -\frac{p}{\lambda_p} \quad (2.23)$$

where λ_p , a positive number, is called the penalty parameter. The right-hand side is different from zero but must remain small to satisfy the condition of incompressibility. The value of the penalty parameter depends on the accuracy of the computer, or more precisely on the word length in bytes to store the numbers. It must be as large as possible, but within the limitation of the machine accuracy to avoid an ill-conditioned matrix due to round-off errors. A value in the range 10^6 - 10^{10} usually proves effective for double precision calculations (word length of 8 bytes). Thus, the pressure is eliminated as a dependent variable in the mathematical formulation reducing the unknowns to the velocity components. This proves to be especially important for 3D calculations to reduce the storage requirements and the calculation time. The pressure is evaluated at the post-processing step using:

$$p = -\lambda_p u_{i,i} \quad (2.24)$$

Using the Divergence theorem, the variational formulation assumes the following form:

$$\int_D \{ \delta u_i \rho u_j u_{i,j} + \delta u_{i,j} (\mu + \mu_T) (u_{i,j} + u_{j,i}) + \lambda_p \delta u_{i,i} u_{i,i} \} dD = \int_S \delta u_i t_i dS \quad (2.25)$$

with

$$t_i = [-p + (\mu + \mu_T) (u_{i,j} + u_{j,i})] n_j \quad (2.26)$$

where t_i are the surface tractions and n_j are the normal components. The pressure appears in the formulation but only implicitly in the right-hand side through the surface tractions.

The integration of the previous equations for all the elements of the domain results in a system of non-linear algebraic equations of the form:

$$[K(U)] \{U\} = \{F\} \quad (2.27)$$

where $[K]$ is the global system matrix, $\{U\}$ is the global vector of unknown velocities, and $\{F\}$ is the global vector of known boundary conditions. The global system matrix is obtained by the summation of the convective, viscous, and penalty matrices. The construction of the penalty matrix uses a consistent approach, which is more accurate when using distorted isoparametric elements [44].

As mentioned previously, one of the main advantages of the FEM is the flexibility of imposing natural boundary conditions. Two cases are of interest: imposing shear stresses on solid surfaces, and using traction-free conditions at boundaries where the velocity components

are not known. An example of the first case is naturally the new treatment of the near-wall region for turbulent flows presented in the previous sections. The wall shear stress is directly imposed along the body surface, and the velocity field is computed with a slip velocity at the wall. For the second case, many situations take advantage of traction-free conditions. First, at a line of symmetry, the velocity component normal to the line is set to zero, while the traction along the line is also set to zero. Second, for an external flow, there is no "natural" boundary away from the body, but the computational domain must be restricted to finite dimensions. Therefore, the outer limit of the domain is set at a location where the viscous effects are small, and the traction-free conditions are used for all components of tractions. The traction-free condition proves to be less constraining than the imposition of velocities at an outer boundary in the case of external flows [45]. Finally, for external and internal flows, the extent of the computational domain must be limited in the direction of the flow. Boundary conditions are usually not known at the outlet and traction-free conditions provide a natural extrapolation of the flow conditions just before the outlet without inducing large disturbances. The combination of essential and natural boundary conditions is one of the biggest assets of the Finite Element method [46].

Looking back at the classification shown in Table 2.5, it can be seen that the formulation of the Finite Element method does not fall under the sub-classification used for the Discretization category. The differencing process is not done with respect to a point of the domain but is rather obtained by the use of interpolation functions for each element. No upwinding is used for the solution of flows at steady-state. The conservation of mass and momentum is intrinsic. And as shown above, the treatment of difficult boundary geometries is done naturally and efficiently without using coordinates transformation or any other approximate and complex techniques.

The next category in the classification concerns the solution technique. The linearized set of non-linear algebraic equations is solved by Lower-Upper (LU) decomposition for all velocity components simultaneously. An iterative strategy is used because of the non-linearity of the equations. The method of successive substitutions without acceleration is used for in the first iterations until the residual is small enough to bring the intermediate solution inside the radius of convergence of the Newton-Raphson method. The successive substitutions are normally used for 2 or 3 iterations depending on the quality of the initial solution, and the Newton-Raphson method then converges quadratically to the numerically "exact" solution.

When the velocity field has been obtained, the pressure is determined at the post-processing step using equation (2.24).

The implementation of the Finite Element method as described above was performed in the program FIDAP developed by Fluid Dynamics International, Inc. [47]. This program is mainly composed of three modules: FIPREP, for geometric modeling, grid generation, and preparation of the input files; FIDAP, for the construction and resolution of the system of equations; and FIPOST, for the graphical analysis of the solution. These modules were installed on an IBM 3090 mainframe computer with Vector Facilities and Extended Architecture. The extended architecture is particularly useful for 3D FEM simulations giving access to 999 megabytes of virtual memory. All calculations were performed on this computer system although the 2D computational procedure and the 3D strip-integral method can be run on workstations and even on some high-end personal computers.

Now that the main concepts and ideas have been introduced, the technical details of the three computational procedures will be presented along with the validation of the numerical predictions obtained for the benchmark test cases.

CHAPTER 3

THREE-DIMENSIONAL STRIP-INTEGRAL METHOD

A new strip-integral method was developed for solving three-dimensional turbulent boundary-layers. It is an extension of the strip-integral formulation for 2D turbulent boundary-layers developed by Moses [22]. The present method takes advantage of the strip-integral formulation by eliminating the use of empirical relations as for the entrainment coefficient, the skin friction coefficient, or any other coefficients and functions. The turbulence modeling is completely "open" as in differential equations. The mathematical developments of the method are presented in the first sections, while the numerical predictions are contained in the last section.

3.1 Integral Equations

The integral equations are obtained by applying the principles of conservation of mass and momentum to a three-dimensional control volume of finite height (H) and infinitesimal base (dx by dz), neglecting the pressure gradient normal to the wall. In Cartesian coordinates, the equations are:

$$\frac{\partial}{\partial x} \int_0^H u^2 dy + \frac{\partial}{\partial z} \int_0^H uw dy - u_H \left[\frac{\partial}{\partial x} \int_0^H u dy + \frac{\partial}{\partial z} \int_0^H w dy \right] = -\frac{H}{\rho} \frac{\partial p}{\partial x} + \frac{(\tau_{xH} - \tau_{xw})}{\rho} \quad (3.1a)$$

$$\frac{\partial}{\partial z} \int_0^H w^2 dy + \frac{\partial}{\partial x} \int_0^H uw dy - w_H \left[\frac{\partial}{\partial x} \int_0^H u dy + \frac{\partial}{\partial z} \int_0^H w dy \right] = -\frac{H}{\rho} \frac{\partial p}{\partial z} + \frac{(\tau_{zH} - \tau_{zw})}{\rho} \quad (3.1b)$$

where $u(y)$ and $w(y)$ are the components of a parametrized 3D velocity profile, u_H and w_H are the velocity components at the upper limit of the strip, p is the pressure, ρ is the density, τ_{xH} and τ_{zH} are the shear stress components at the upper limit of the strip, and τ_{xw} and τ_{zw} are the wall shear stress components.

Based on the experience of other researchers [33], it was decided to use a non-orthogonal streamline coordinates system (see Fig. 3.1). One axis is set along the external streamlines, while the direction of the other axis depends on the geometry and the flow conditions.

Thus, the equations become:

$$\begin{aligned} & \left[\frac{1}{q} \frac{\partial}{\partial X} \left(\frac{q}{h_x} \int_0^H \bar{U}^2 dy \right) + \frac{1}{q} \frac{\partial}{\partial Z} \left(\frac{q}{h_z} \int_0^H \bar{U} \bar{W} dy \right) - \frac{\bar{U}_H}{q} \left[\frac{\partial}{\partial X} \left(\frac{q}{h_x} \int_0^H \bar{U} dy \right) + \frac{\partial}{\partial Z} \left(\frac{q}{h_z} \int_0^H \bar{W} dy \right) \right] \right] \\ & + K_1 \int_0^H \bar{U}^2 dy + K_2 \int_0^H \bar{W}^2 dy + K_3 \int_0^H \bar{U} \bar{W} dy = \frac{(\bar{\tau}_{xH} - \bar{\tau}_{xw})}{\rho} + H U_e^2 K_1 + \frac{H U_e}{h_x} \frac{\partial U_e}{\partial X} \end{aligned} \quad (3.2a)$$

$$\begin{aligned} & \left[\frac{1}{q} \frac{\partial}{\partial Z} \left(\frac{q}{h_z} \int_0^H \bar{W}^2 dy \right) + \frac{1}{q} \frac{\partial}{\partial X} \left(\frac{q}{h_x} \int_0^H \bar{U} \bar{W} dy \right) - \frac{\bar{W}_H}{q} \left[\frac{\partial}{\partial X} \left(\frac{q}{h_x} \int_0^H \bar{U} dy \right) + \frac{\partial}{\partial Z} \left(\frac{q}{h_z} \int_0^H \bar{W} dy \right) \right] \right] \\ & + L_1 \int_0^H \bar{U}^2 dy + L_2 \int_0^H \bar{W}^2 dy + L_3 \int_0^H \bar{U} \bar{W} dy = \frac{(\bar{\tau}_{zH} - \bar{\tau}_{zw})}{\rho} + H U_e^2 L_1 \end{aligned} \quad (3.2b)$$

with $q = h_x h_z \sin \lambda$ $K_1 = -\cos \lambda L_1$ $L_2 = -\cos \lambda K_2$

$$\begin{aligned} K_2 &= \frac{1}{q \sin \lambda} \left[\frac{\partial(h_x \cos \lambda)}{\partial Z} - \frac{\partial h_z}{\partial X} \right] & K_3 &= \frac{1}{q \sin \lambda} \left[(1 + \cos^2 \lambda) \frac{\partial h_x}{\partial Z} - 2 \cos \lambda \frac{\partial h_z}{\partial X} \right] \\ L_1 &= \frac{1}{q \sin \lambda} \left[\frac{\partial(h_z \cos \lambda)}{\partial X} - \frac{\partial h_x}{\partial Z} \right] & L_3 &= \frac{1}{q \sin \lambda} \left[(1 + \cos^2 \lambda) \frac{\partial h_z}{\partial X} - 2 \cos \lambda \frac{\partial h_x}{\partial Z} \right] \end{aligned}$$

where X and Z are the non-orthogonal coordinates, h_x and h_z are the metrics of the transformation, λ is the angle between the non-orthogonal axes, U_e is the edge velocity, \bar{U} and \bar{W} are the non-orthogonal velocity components, \bar{U}_H and \bar{W}_H are the non-orthogonal velocity components at the upper limit of the strip, $\bar{\tau}_{xH}$ and $\bar{\tau}_{zH}$ are the non-orthogonal shear stress components at the upper limit of the strip, and $\bar{\tau}_{xw}$ and $\bar{\tau}_{zw}$ are the non-orthogonal wall shear stress components. The pressure gradient was transformed using the equations for the inviscid solution in non-orthogonal coordinates. The inviscid solution, which is used in the integral method through the intermediate of the edge velocity and the description of the external streamlines, is obtained from experimental data when available or from an inviscid calculation. The metrics, h_x and h_z , and λ are computed numerically at the pre-processing step. The use of non-orthogonal coordinates and the numerical calculation of the metrics insure complete freedom in the creation of the computational domain.

3.2 Velocity Profile

The integral methods depend primarily on the parametrization of the velocity profiles. Here, a practical 4-parameter velocity profile was chosen for reasons mentioned previously. The total velocity is divided into 2 components: the first component is in the direction of the tangent to the external streamlines, and the second component is perpendicular to the first one [33]. Therefore, the velocity profile is expressed in streamline orthogonal coordinates and must be transformed to the non-orthogonal coordinates system before integration. In the streamwise direction, the Law of the Wake is constructed from the Johnston Law of the Wall and the Moses wake function. The crosswise velocity is obtained by the Johnston triangular model. The orthogonal components of the velocity profile are written as:

$$\frac{U}{U_e} = A \cos \beta_w \ln(C_{LW} A Re_\delta \eta) - B \eta^2 (3-2\eta) \quad (3.3)$$

$$\text{and} \quad \frac{W}{U_e} = \frac{U}{U_e} \tan \beta_w \quad \text{for } \eta < \eta_{mc} \quad (3.4a)$$

$$\text{or} \quad \frac{W}{U_e} = C_{mc} \left(1 - \frac{U}{U_e}\right) \quad \text{for } \eta > \eta_{mc} \quad (3.4b)$$

$$\text{with} \quad B = A \cos \beta_w \ln(C_{LW} A Re_\delta) - 1 \quad C_{mc} = \frac{W_{mc}}{U_e - U_{mc}}$$

$$\text{and} \quad C_{LW} = 3.06 \quad \eta = \frac{y}{\delta} \quad Re_\delta = \frac{\rho U_e \delta}{\mu} \quad A = \frac{1}{\kappa} \sqrt{\frac{\tau_w}{\rho U_e^2}}$$

where U is the streamwise velocity component, W is the crosswise velocity component, U_e is the edge velocity, A is a normalized wall shear stress, β_w is the wall crossflow angle, δ is the boundary-layer thickness, η_{mc} is the location of maximum crosswise velocity, and U_{mc} and W_{mc} are respectively the streamwise and crosswise velocity at this location. A comparison was made with the velocity profiles at 2 stations for the Van den Berg-Elsenaar experiment. Figures 3.2 and 3.4 show an excellent agreement for the streamwise velocity, while the adequacy of the triangular model is demonstrated in Figures 3.3 and 3.5.

3.3 Turbulence Model

Contrary to other integral methods, the shear stresses at the top of the inner control volume appear directly in the strip-integral formulation. The Boussinesq assumption relates the shear stresses to the velocity gradients in orthogonal streamline coordinates:

$$\tau_{xH} = \mu_{T_x} \frac{\partial U}{\partial y} \quad (3.5a)$$

$$\tau_{zH} = \mu_{T_z} \frac{\partial W}{\partial y} \quad (3.5b)$$

with

$$\mu_{T_z} = C_{zx} \mu_{T_x}$$

μ_{T_x} is the streamwise eddy viscosity and μ_{T_z} is the crosswise eddy viscosity. Previous experiments have shown that the ratio of eddy viscosities (C_{zx}) can be smaller or greater than 1.0, because of the anisotropy of the turbulent shear stress. The influence of C_{zx} was studied for one test-case, and the analysis is presented in the last section. It should be noted that a value of 1.0 (isotropic) would be adequate when no information is available about the flow.

The streamwise eddy viscosity is defined by the Clauser outer region model [25]. This model has proven adequate for two-dimensional analyses, and the extension to a 3D analysis is straightforward:

$$\mu_{T_x} = 0.0168 \rho U_e \delta_1 \quad (3.6)$$

where δ_1 is the streamwise displacement thickness. A model for the inner region is not required because the shear stresses are computed at the upper limit of the inner strip, which is always chosen in the outer region of the boundary-layer. The turbulence model is simple and adequate for 3D analyses, but, if necessary, a more sophisticated model can be implemented easily without changing the basic formulation.

3.4 Set of Differential Equations

Two momentum integral equations were written in non-orthogonal streamline coordinates for an arbitrary control volume, and a velocity profile was formulated in orthogonal streamline coordinates using four parameters. Four equations are obtained by using two strips: the first strip goes from the wall up to a location inside the boundary-layer (inner strip), which is arbitrary; and the second strip is chosen as the entire boundary-layer. At the edge of the boundary-layer, the upper limit velocity becomes the edge velocity and the upper limit shear stress components are zero. The following integral equations are then obtained:

$$\begin{aligned} \frac{\partial G_{C1}}{\partial X} - \frac{\bar{U}_H}{U_e} \frac{\partial G_{A1}}{\partial X} + \frac{G_{C1}}{Re_{\delta 1}} \frac{\partial (Re_{\delta 1})}{\partial X} - \frac{\bar{U}_H}{U_e} \frac{G_{A1}}{Re_{\delta 1}} \frac{\partial (Re_{\delta 1})}{\partial X} = F_{X1} = \frac{h_x (\bar{\tau}_{XH} - \bar{\tau}_{XW})}{\mu U_e Re_{\delta 1}} \\ + \eta_H \left(\frac{1}{U_e} \frac{\partial U_e}{\partial X} + h_x K_1 \right) - h_x (K_1 G_{C1} + K_2 G_{E1} + K_3 G_{D1}) \\ - \frac{h_x}{q U_e} \left\{ G_{C1} \frac{\partial (q U_e)}{\partial X} \frac{\partial (q)}{h_x} - \bar{U}_H G_{A1} \frac{\partial (q)}{\partial X} \frac{\partial (q)}{h_x} \right\} - \frac{h_x}{q U_e Re_{\delta 1}} \left\{ \frac{\partial (q U_e Re_{\delta 1} G_{D1})}{\partial Z} \frac{\partial (q)}{h_z} - \bar{U}_H \frac{\partial (q Re_{\delta 1} G_{B1})}{\partial Z} \frac{\partial (q)}{h_z} \right\} \end{aligned} \quad (3.7a)$$

$$\begin{aligned} \frac{\partial G_{D1}}{\partial X} - \frac{\bar{W}_H}{U_e} \frac{\partial G_{A1}}{\partial X} + \frac{G_{D1}}{Re_{\delta 1}} \frac{\partial (Re_{\delta 1})}{\partial X} - \frac{\bar{W}_H}{U_e} \frac{G_{A1}}{Re_{\delta 1}} \frac{\partial (Re_{\delta 1})}{\partial X} = F_{Z1} = \frac{h_x (\bar{\tau}_{ZH} - \bar{\tau}_{ZW})}{\mu U_e Re_{\delta 1}} \\ + \eta_H h_x L_1 - h_x (L_1 G_{C1} + L_2 G_{E1} + L_3 G_{D1}) \\ - \frac{h_x}{q U_e} \left\{ G_{D1} \frac{\partial (q U_e)}{\partial X} \frac{\partial (q)}{h_x} - \bar{W}_H G_{A1} \frac{\partial (q)}{\partial X} \frac{\partial (q)}{h_x} \right\} - \frac{h_x}{q U_e Re_{\delta 1}} \left\{ \frac{\partial (q U_e Re_{\delta 1} G_{E1})}{\partial Z} \frac{\partial (q)}{h_z} - \bar{W}_H \frac{\partial (q Re_{\delta 1} G_{B1})}{\partial Z} \frac{\partial (q)}{h_z} \right\} \end{aligned} \quad (3.7b)$$

$$\begin{aligned} \frac{\partial G_{C2}}{\partial X} - \frac{\partial G_{A2}}{\partial X} + \frac{(G_{C2} - G_{A2})}{Re_{\delta 1}} \frac{\partial (Re_{\delta 1})}{\partial X} = F_{X2} = \frac{-h_x \bar{\tau}_{XW}}{\mu U_e Re_{\delta 1}} \\ + \left(\frac{1}{U_e} \frac{\partial U_e}{\partial X} + h_x K_1 \right) - h_x (K_1 G_{C2} + K_2 G_{E2} + K_3 G_{D2}) \\ - \frac{h_x}{q U_e} \left\{ G_{C2} \frac{\partial (q U_e)}{\partial X} \frac{\partial (q)}{h_x} - U_e G_{A2} \frac{\partial (q)}{\partial X} \frac{\partial (q)}{h_x} \right\} - \frac{h_x}{q U_e Re_{\delta 1}} \left\{ \frac{\partial (q U_e Re_{\delta 1} G_{D2})}{\partial Z} \frac{\partial (q)}{h_z} - U_e \frac{\partial (q Re_{\delta 1} G_{B2})}{\partial Z} \frac{\partial (q)}{h_z} \right\} \end{aligned} \quad (3.7c)$$

$$\begin{aligned} \frac{\partial G_{D2}}{\partial X} + \frac{G_{D2}}{Re_{\delta 1}} \frac{\partial (Re_{\delta 1})}{\partial X} = F_{Z2} = \frac{-h_x \bar{\tau}_{ZW}}{\mu U_e Re_{\delta 1}} + h_x L_1 - h_x (L_1 G_{C2} + L_2 G_{E2} + L_3 G_{D2}) \\ - \frac{h_x G_{D2}}{q U_e} \frac{\partial (q U_e)}{\partial X} \frac{\partial (q)}{h_x} - \frac{h_x}{q U_e Re_{\delta 1}} \frac{\partial (q U_e Re_{\delta 1} G_{E2})}{\partial Z} \frac{\partial (q)}{h_z} \end{aligned} \quad (3.7d)$$

with

$$\begin{aligned} G_{A1} &= \int_0^{\eta_H} \frac{\bar{U}}{U_e} d\eta & G_{A2} &= \int_0^1 \frac{\bar{U}}{U_e} d\eta \\ G_{B1} &= \int_0^{\eta_H} \frac{\bar{W}}{U_e} d\eta & G_{B2} &= \int_0^1 \frac{\bar{W}}{U_e} d\eta \end{aligned}$$

$$\begin{aligned}
 G_{C1} &= \int_0^{\eta_H} \left(\frac{\bar{U}}{U_\theta} \right)^2 d\eta & G_{C2} &= \int_0^1 \left(\frac{\bar{U}}{U_\theta} \right)^2 d\eta \\
 G_{D1} &= \int_0^{\eta_H} \frac{\bar{U}\bar{W}}{U_\theta^2} d\eta & G_{D2} &= \int_0^1 \frac{\bar{U}\bar{W}}{U_\theta^2} d\eta \\
 G_{E1} &= \int_0^{\eta_H} \left(\frac{\bar{W}}{U_\theta} \right)^2 d\eta & G_{E2} &= \int_0^1 \left(\frac{\bar{W}}{U_\theta} \right)^2 d\eta
 \end{aligned}$$

The transformation between orthogonal streamline coordinates and non-orthogonal streamline coordinates yields the following relations:

$$\begin{aligned}
 \bar{U} &= U - \frac{W}{\tan \lambda} & \text{and} & & \bar{W} &= \frac{W}{\sin \lambda} \\
 \bar{\tau}_x &= \tau_x - \frac{\tau_z}{\tan \lambda} & \text{and} & & \bar{\tau}_z &= \frac{\tau_z}{\sin \lambda}
 \end{aligned}$$

and

$$G_{A1} = F_{A1} - \frac{F_{B1}}{\tan \lambda} \quad (3.8a)$$

$$G_{B1} = \frac{F_{B1}}{\sin \lambda} \quad (3.8b)$$

$$G_{C1} = F_{C1} - \frac{2F_{D1}}{\tan \lambda} + \frac{F_{E1}}{\tan^2 \lambda} \quad (3.8c)$$

$$G_{D1} = \frac{1}{\sin \lambda} \left(F_{D1} - \frac{F_{E1}}{\tan \lambda} \right) \quad (3.8d)$$

$$G_{E1} = \frac{F_{E1}}{\sin^2 \lambda} \quad (3.8e)$$

$$G_{A2} = F_{A2} - \frac{F_{B2}}{\tan \lambda} \quad (3.9a)$$

$$G_{B2} = \frac{F_{B2}}{\sin \lambda} \quad (3.9b)$$

$$G_{C2} = F_{C2} - \frac{2F_{D2}}{\tan \lambda} + \frac{F_{E2}}{\tan^2 \lambda} \quad (3.9c)$$

$$G_{D2} = \frac{1}{\sin \lambda} \left(F_{D2} - \frac{F_{E2}}{\tan \lambda} \right) \quad (3.9d)$$

$$G_{E2} = \frac{F_{E2}}{\sin^2 \lambda} \quad (3.9e)$$

with

$$F_{A1} = \int_0^{\eta_H} \frac{U}{U_\theta} d\eta$$

$$F_{A2} = \int_0^1 \frac{U}{U_\theta} d\eta$$

$$\begin{aligned}
 F_{B1} &= \int_0^{\eta_H} \frac{W}{U_e} d\eta & F_{B2} &= \int_0^1 \frac{W}{U_e} d\eta \\
 F_{C1} &= \int_0^{\eta_H} \left(\frac{U}{U_e}\right)^2 d\eta & F_{C2} &= \int_0^1 \left(\frac{U}{U_e}\right)^2 d\eta \\
 F_{D1} &= \int_0^{\eta_H} \frac{UW}{U_e^2} d\eta & F_{D2} &= \int_0^1 \frac{UW}{U_e^2} d\eta \\
 F_{E1} &= \int_0^{\eta_H} \left(\frac{W}{U_e}\right)^2 d\eta & F_{E2} &= \int_0^1 \left(\frac{W}{U_e}\right)^2 d\eta
 \end{aligned}$$

Using the expressions for the velocity from equations (3.3), (3.4a) and (3.4b), one finds:

$$F_{A2} = (1 - C_{FAa2}) + A \cos \beta_w (C_{FAa2} \ln(C_{LW} A Re_\delta) + C_{FAb2}) \quad (3.10)$$

with

$$\begin{aligned}
 C_{FAa2} &= \frac{1}{2} \\
 C_{FAb2} &= -1
 \end{aligned}$$

$$\begin{aligned}
 F_{C2} &= C_{FCa2} + 2A \cos \beta_w (C_{FCc2} \ln(C_{LW} A Re_\delta) + C_{FCb2}) \\
 &+ A^2 \cos^2 \beta_w (C_{FCf2} \ln^2(C_{LW} A Re_\delta) + C_{FCe2} \ln(C_{LW} A Re_\delta) + C_{FCd2})
 \end{aligned} \quad (3.11)$$

with

$$\begin{aligned}
 C_{FCa2} &= \frac{13}{35} \\
 C_{FCb2} &= \frac{-5}{24} \\
 C_{FCc2} &= \frac{9}{70} \\
 C_{FCd2} &= 2 \\
 C_{FCe2} &= \frac{-19}{12} \\
 C_{FCf2} &= \frac{13}{35}
 \end{aligned}$$

$$F_{B2} = F_{B0} + C_{mc} (1 - \eta_{mc} - F_{A2} + F_{A0}) \quad (3.12)$$

$$F_{D2} = F_{D0} + C_{mc} (F_{A2} - F_{A0} - F_{C2} + F_{C0}) \quad (3.13)$$

$$F_{E2} = F_{E0} + C_{mc}^2 (1 - \eta_{mc} - 2(F_{A2} - F_{A0}) + F_{C2} - F_{C0}) \quad (3.14)$$

and $F_{A1} = (\eta_H - C_{FAa1}) + A \cos \beta_w (C_{FAa1} \ln(C_{Lw} A Re_\delta) + C_{FAb1})$ (3.15)

with $C_{FAa1} = \eta_H - \eta_H^3 (2 - \eta_H)$

$$C_{FAb1} = \eta_H (\ln \eta_H - 1)$$

$$F_{C1} = C_{FCa1} + 2A \cos \beta_w (C_{FCc1} \ln(C_{Lw} A Re_\delta) + C_{FCb1}) + A^2 \cos^2 \beta_w (C_{FCf1} \ln^2(C_{Lw} A Re_\delta) + C_{FCe1} \ln(C_{Lw} A Re_\delta) + C_{FCd1})$$
 (3.16)

with $C_{FCa1} = \eta_H^5 \left(\frac{9}{5} - 2\eta_H + \frac{4}{7} \eta_H^2 \right)$

$$C_{FCb1} = \eta_H^3 \left(\ln \eta_H - \frac{1}{3} - \frac{1}{2} \eta_H \left(\ln \eta_H - \frac{1}{4} \right) \right)$$

$$C_{FCc1} = \eta_H^3 \left(1 - \frac{1}{2} \eta_H - \frac{9}{5} \eta_H^2 + 2\eta_H^3 - \frac{4}{7} \eta_H^4 \right)$$

$$C_{FCd1} = \eta_H (\ln^2 \eta_H - 2 \ln \eta_H + 2)$$

$$C_{Fce1} = 2\eta_H (\ln \eta_H - 1 - \eta_H^2 (\ln \eta_H - \frac{1}{3})) + \frac{1}{2} \eta_H (\ln \eta_H - \frac{1}{4})$$

$$C_{FCf1} = \eta_H \left(1 - 2\eta_H^2 + \eta_H^3 + \frac{9}{5} \eta_H^4 - 2\eta_H^5 + \frac{4}{7} \eta_H^6 \right)$$

and $F_{B1} = F_{A1} \tan \beta_w$ (3.17a)

$$F_{D1} = F_{C1} \tan \beta_w \quad \text{for } \eta_H < \eta_{mc} \quad (3.18a)$$

$$F_{E1} = F_{D1} \tan \beta_w \quad (3.19a)$$

or $F_{B1} = F_{B0} + C_{mc} (\eta_H - \eta_{mc} - F_{A1} + F_{A0})$ (3.17b)

$$F_{D1} = F_{D0} + C_{mc} (F_{A1} - F_{A0} - F_{C1} + F_{C0}) \quad \text{for } \eta_H > \eta_{mc} \quad (3.18b)$$

$$F_{E1} = F_{E0} + C_{mc}^2 (\eta_H - \eta_{mc} - 2(F_{A1} - F_{A0}) + F_{C1} - F_{C0}) \quad (3.19b)$$

and $F_{A0} = (\eta_{mc} - C_{FAa0}) + A \cos \beta_w (C_{FAa0} \ln(C_{Lw} A Re_\delta) + C_{FAb0})$ (3.20)

with $C_{FAa0} = \eta_{mc} - \eta_{mc}^3 (2 - \eta_{mc})$

$$C_{FAb0} = \eta_{mc} (\ln \eta_{mc} - 1)$$

$$\begin{aligned}
F_{C0} &= C_{FCa0} + 2A \cos \beta_w (C_{FCc0} \ln(C_{LW} A Re_\delta) + C_{FCb0}) \\
&+ A^2 \cos^2 \beta_w (C_{FCf0} \ln^2(C_{LW} A Re_\delta) + C_{FCe0} \ln(C_{LW} A Re_\delta) + C_{FCd0})
\end{aligned} \tag{3.21}$$

with

$$C_{FCa0} = \eta_{mc}^5 \left(\frac{9}{5} - 2\eta_{mc} + \frac{4}{7}\eta_{mc}^2 \right)$$

$$C_{FCb0} = \eta_{mc}^3 \left(\ln \eta_{mc} - \frac{1}{3} - \frac{1}{2}\eta_{mc} \left(\ln \eta_{mc} - \frac{1}{4} \right) \right)$$

$$C_{FCc0} = \eta_{mc}^3 \left(1 - \frac{1}{2}\eta_{mc} - \frac{9}{5}\eta_{mc}^2 + 2\eta_{mc}^3 - \frac{4}{7}\eta_{mc}^4 \right)$$

$$C_{FCd0} = \eta_{mc} \left(\ln^2 \eta_{mc} - 2 \ln \eta_{mc} + 2 \right)$$

$$C_{FCe0} = 2\eta_{mc} \left(\ln \eta_{mc} - 1 - \eta_{mc}^2 \left(\ln \eta_{mc} - \frac{1}{3} \right) + \frac{1}{2}\eta_{mc} \left(\ln \eta_{mc} - \frac{1}{4} \right) \right)$$

$$C_{FCf0} = \eta_{mc} \left(1 - 2\eta_{mc}^2 + \eta_{mc}^3 + \frac{9}{5}\eta_{mc}^4 - 2\eta_{mc}^5 + \frac{4}{7}\eta_{mc}^6 \right)$$

$$\text{and} \quad F_{B0} = F_{A0} \tan \beta_w \tag{3.22}$$

$$F_{D0} = F_{C0} \tan \beta_w \tag{3.23}$$

$$F_{E0} = F_{D0} \tan \beta_w \tag{3.24}$$

The transformation of the X-derivatives in the left-hand side of equations (3.7a) to (3.7d) yields the following relations:

$$\frac{\partial G_{A2}}{\partial X} = \frac{\partial F_{A2}}{\partial X} - \frac{1}{\tan \lambda} \frac{\partial F_{B2}}{\partial X} + \frac{G_{B2}}{\sin \lambda} \frac{\partial \lambda}{\partial X} \tag{3.25}$$

$$\frac{\partial G_{C2}}{\partial X} = \frac{\partial F_{C2}}{\partial X} - \frac{2}{\tan \lambda} \frac{\partial F_{D2}}{\partial X} + \frac{1}{\tan^2 \lambda} \frac{\partial F_{E2}}{\partial X} + \frac{2G_{D2}}{\sin \lambda} \frac{\partial \lambda}{\partial X} \tag{3.26}$$

$$\frac{\partial G_{D2}}{\partial X} = \frac{1}{\sin \lambda} \left\{ \frac{\partial F_{D2}}{\partial X} - \frac{1}{\tan \lambda} \frac{\partial F_{E2}}{\partial X} + (G_{E2} - \cos \lambda G_{D2}) \frac{\partial \lambda}{\partial X} \right\} \tag{3.27}$$

and

$$\frac{\partial G_{A1}}{\partial X} = \frac{\partial F_{A1}}{\partial X} - \frac{1}{\tan \lambda} \frac{\partial F_{B1}}{\partial X} + \frac{G_{B1}}{\sin \lambda} \frac{\partial \lambda}{\partial X} \tag{3.28}$$

$$\frac{\partial G_{C1}}{\partial X} = \frac{\partial F_{C1}}{\partial X} - \frac{2}{\tan \lambda} \frac{\partial F_{D1}}{\partial X} + \frac{1}{\tan^2 \lambda} \frac{\partial F_{E1}}{\partial X} + \frac{2G_{D1}}{\sin \lambda} \frac{\partial \lambda}{\partial X} \tag{3.29}$$

$$\frac{\partial G_{D1}}{\partial X} = \frac{1}{\sin \lambda} \left\{ \frac{\partial F_{D1}}{\partial X} - \frac{1}{\tan \lambda} \frac{\partial F_{E1}}{\partial X} + (G_{E1} - \cos \lambda G_{D1}) \frac{\partial \lambda}{\partial X} \right\} \tag{3.30}$$

The expressions for the derivatives of equations (3.10) to (3.19) are used to obtain the expanded expressions of the derivatives in equations (3.25) to (3.30), which are then introduced in equations (3.7a) to (3.7d) yielding the following matrix form for the final set of equations:

$$C_{j1} \frac{\partial A}{\partial X} + C_{j2} \frac{\partial \beta_w}{\partial X} + \frac{C_{j3}}{Re_\delta} \frac{\partial Re_\delta}{\partial X} + C_{j4} \frac{\partial \eta_{mc}}{\partial X} = F_j \quad j=1,4 \quad (3.31)$$

The right-hand sides contain all derivatives with respect to the crosswise direction, and all derivatives with respect to the streamwise direction for the known variables. The coefficients and the right-hand sides are functions of the four unknowns, the edge velocity, and the form of the mesh, which is described by the shape of the external streamlines and the metrics of the transformation to non-orthogonal coordinates. The solution of the matrix system by Gauss elimination leads to the following expressions for each derivative:

$$\frac{\partial \eta_{mc}}{\partial X} = f^1(X, Z, A, \beta_w, Re_\delta, \eta_{mc}) = \frac{C'_{33} F_4 - C'_{43} F_3}{C'_{33} C'_{44} - C'_{43} C'_{34}} \quad (3.32a)$$

$$\frac{1}{Re_\delta} \frac{\partial Re_\delta}{\partial X} = f^2(X, Z, A, \beta_w, Re_\delta, \eta_{mc}) = \frac{F_3}{C'_{33}} - \frac{C'_{34}}{C'_{33}} \frac{\partial \eta_{mc}}{\partial X} \quad (3.32b)$$

$$\frac{\partial \beta_w}{\partial X} = f^3(X, Z, A, \beta_w, Re_\delta, \eta_{mc}) = \frac{F_2}{C'_{22}} - \frac{C'_{23}}{C'_{22} Re_\delta} \frac{\partial Re_\delta}{\partial X} - \frac{C'_{24}}{C'_{22}} \frac{\partial \eta_{mc}}{\partial X} \quad (3.32c)$$

$$\frac{\partial A}{\partial X} = f^4(X, Z, A, \beta_w, Re_\delta, \eta_{mc}) = \frac{F_1}{C_{11}} - \frac{C_{12}}{C_{11}} \frac{\partial \beta_w}{\partial X} - \frac{C_{13}}{C_{11} Re_\delta} \frac{\partial Re_\delta}{\partial X} - \frac{C_{14}}{C_{11}} \frac{\partial \eta_{mc}}{\partial X} \quad (3.32d)$$

with
$$C'_{jm} = C_{jm} - \frac{C_{j1}}{C_{11}} C_{1m} \quad F_j = F_j - \frac{C_{j1}}{C_{11}} F_1 \quad j=2,4 \quad m=2,4$$

and
$$C''_{jm} = C'_{jm} - \frac{C'_{j2}}{C'_{22}} C'_{2m} \quad F'_j = F_j - \frac{C'_{j2}}{C'_{22}} F_2 \quad j=3,4 \quad m=3,4$$

3.5 Numerical Scheme

The above differential equations are hyperbolic [33]. The characteristics at a point over the surface are all located between the external streamlines and the wall streamlines (also called skin friction lines). The shape of the characteristics and the orientation of one with respect to the other affect the discretization of the equations and the implementation of the boundary conditions. The main principles to keep in mind are: the numerical domain of dependence must include the physical domain of dependence (CFL condition), and boundary conditions are needed along the sides where the flow comes into the computational domain.

From the initial station along the wall where the skin friction coefficient (and therefore A), the wall crossflow angle, the boundary-layer thickness and the location of maximum crosswise velocity are known, the values of the four variables are computed at the following stations by marching in space along each external streamline. The solution of the set of 4 first-order differential equations was achieved by the second-order Runge-Kutta scheme. The first part of the integration is:

$$\eta_{mc}^*_{i,k} = \eta_{mc}^*_{i-1,k} + \Delta x f^1_{i-1,k} \quad (3.33a)$$

$$Re_{\delta}^*_{i,k} = Re_{\delta}^*_{i-1,k} + \Delta x Re_{\delta}^*_{i-1,k} f^2_{i-1,k} \quad (3.33b)$$

$$\beta_w^*_{i,k} = \beta_w^*_{i-1,k} + \Delta x f^3_{i-1,k} \quad (3.33c)$$

$$A^*_{i,k} = A_{i-1,k} + \Delta x f^4_{i-1,k} \quad (3.33d)$$

The second part of the integration is then:

$$\eta_{mc}^*_{i,k} = \eta_{mc}^*_{i-1,k} + 0.5 \Delta x \{ f^1_{i-1,k} + f^{1*}_{i,k} \} \quad (3.34a)$$

$$Re_{\delta}^*_{i,k} = Re_{\delta}^*_{i-1,k} + 0.5 \Delta x \{ Re_{\delta}^*_{i-1,k} f^2_{i-1,k} + Re_{\delta}^*_{i,k} f^{2*}_{i,k} \} \quad (3.34b)$$

$$\beta_w^*_{i,k} = \beta_w^*_{i-1,k} + 0.5 \Delta x \{ f^3_{i-1,k} + f^{3*}_{i,k} \} \quad (3.34c)$$

$$A_{i,k} = A_{i-1,k} + 0.5 \Delta x \{ f^4_{i-1,k} + f^{4*}_{i,k} \} \quad (3.34d)$$

3.6 STRIP3D Results

Van den Berg-Elsenaar Flow

The flow over a flat surface with a 35° sweep angle under infinite swept-wing conditions in an adverse-pressure gradient was investigated by Van den Berg and Elsenaar [48,49]. The information about the computational domain is presented in Figure 3.6. The flow characteristics are computed for the first 8 stations (following the original numbering convention of the investigators). Separation occurs near station 9, and the present method can not be applied for separated flows. The width of the computational region is somewhat artificial because the infinite swept-wing conditions mean that there is no variation in the spanwise direction (parallel to the leading edge).

The complete results are shown in Figures 3.7 to 3.10, along with the experimental measurements and the predictions of the integral methods of Cousteix et al, Cross, and Smith, as presented in Ref. 21. The three integral methods make use of the entrainment equation. Cousteix et al use functions based on local similarity to model the entrainment coefficient, and an empirical relation for the skin friction coefficient. The numerical integration is done with the fourth-order Runge-Kutta scheme. Cross uses an algebraic equation for the entrainment velocity, and Coles' velocity profiles. Smith's method solves a differential equation to evaluate the entrainment coefficient, represents the velocity by the Power Law and Mager's relation, and uses Green's formula for the skin friction coefficient. The numerical integration in Cross' and Smith's methods is done with the second-order Runge-Kutta scheme.

The first simulation was performed neglecting the crosswise derivatives. The solution was computed along a streamline using 71 nodes, $\eta_H=0.25$, and $C_{zX}=1.0$. A good agreement is globally obtained. A relative error of about 20% is found for the wall crossflow angle at the last station. As opposed to most other numerical methods, the wall crossflow angle does not start to decrease after $x=1.12$. The general trend is well represented when approaching separation, even if a simple turbulence model is used for the present method. The results for the wall crossflow angle show a wavy character making the error larger near $x=0.82$ and $x=1.02$. This behavior can be explained by the strong dependency of the wall crossflow angle on the location of maximum crosswise velocity, which in turn is numerically sensitive.

Calculations were also performed including the crosswise derivatives. The solution was computed on the adjacent streamline for two different crosswise step sizes: 0.01 and 0.001. For these calculations, the hyperbolic character of the equations becomes important. The streamwise step size must be set depending on the crosswise step size following the CFL condition. The solutions were obtained using 101 nodes for $\Delta Z=0.01$, and 441 nodes for $\Delta Z=0.001$. As expected, the agreement with the measurements is better for a smaller step size.

Figures 3.11 to 3.14 show the influence of the upper limit of the inner strip on the results for all parameters. The crosswise derivatives are set to zero, and the same node distribution is used. The variation with η_H is stronger for the wall crossflow angle at the end of the domain, but generally, the influence of η_H is not critical for values in the present range.

Müller-Krause Flow

The second case studied is the flow over a flat surface with an adverse-pressure gradient in the streamwise direction, and an induced pressure gradient in the crosswise direction. This flow was investigated by Müller and Krause [50]. The information concerning the geometry of the computational domain is presented in Figure 3.15.

The predictions for all parameters along a line parallel to the z-axis are respectively shown in Figures 3.16 to 3.19 for $x=0.4$, and in Figures 3.20 to 3.23 for $x=0.6$, along with the experimental measurements and the predictions of three other numerical methods, as presented in Ref. 21. The upper limit of the inner strip is located at 0.35, and the eddy viscosity ratio is set to 1.2, following the recommendation of Müller. A relatively coarse mesh was used: 81 nodes in the streamwise direction and 41 nodes in the crosswise direction. Again here, the results show a wavy character depending on the location of maximum crosswise velocity. The values of η_{mc} used as boundary conditions along the inside streamline were extracted from the measured velocity profiles. These values are approximate, and they have a strong influence on the solution near the inside streamline.

The 3D strip-integral method produces similar results compared to Cross' integral method. The present predictions are also equivalent or better at a fraction of the cost, compared to the differential methods of Müller, and Patel et al. Müller's method solves the boundary-layer equations in Cartesian coordinates using an isotropic eddy-viscosity model

based on Michel's mixing length and Van Driest damping factor, and the numerical solution is obtained by semi-implicit schemes. Patel's method makes use of the equations of motion written in orthogonal coordinates using transformation and redistribution, and solved by the Crank-Nicolson scheme.

As for the Van den Berg-Elsenaar case, the influence of the inner strip upper limit on the skin friction coefficient and the wall crossflow angle was studied, and the results are shown in Figures 3.24 and 3.25 for the line $x=0.4$, and in Figures 3.26 and 3.27 for the line $x=0.6$. The same node distribution was also used. The influence of η_H is more important for the present case, and larger values give better overall results.

The influence of the eddy viscosity ratio was also studied. The results for the skin friction coefficient and wall crossflow angle are shown in Figures 3.28 and 3.29 for $x=0.4$, and in Figures 3.30 and 3.31 for $x=0.6$. Three values were used: 1.0, 1.2, and 1.4. The eddy viscosity ratio has no influence on the skin friction coefficient, but the wall crossflow angle is strongly dependent on this parameter. At $x=0.4$, a value of 1.4 gives better results, while a value of 1.0 is more appropriate at $x=0.6$. When no information is available about the shear stresses, a value of unity (isotropic case) would prove adequate.

CHAPTER 4

TWO-DIMENSIONAL NAVIER-STOKES COMPUTATIONAL PROCEDURE

The new approach to treat the near-wall region was implemented in a computational procedure solving the Reynolds Averaged Navier-Stokes equations for flows in or about 2D geometries. The procedure is based on the Finite Element method using a natural boundary condition for the wall shear stress which is obtained from the solution of a 1-strip-integral equation for the inner region. The mathematical developments of the method are presented in the first two sections, while the procedure is described in the third section and the numerical predictions are shown in the last section.

4.1 2D Navier-Stokes Solver

Equations

The mathematical model consists of the continuity equation and the momentum equations:

$$\frac{\partial u}{\partial x} + \frac{\partial v}{\partial y} = 0 \quad (4.1a)$$

$$\rho \left(u \frac{\partial u}{\partial x} + v \frac{\partial u}{\partial y} \right) = -\frac{\partial p}{\partial x} + \frac{\partial}{\partial x} \left[(\mu + \mu_T) 2 \frac{\partial u}{\partial x} \right] + \frac{\partial}{\partial y} \left[(\mu + \mu_T) \left(\frac{\partial u}{\partial y} + \frac{\partial v}{\partial x} \right) \right] \quad (4.1b)$$

$$\rho \left(u \frac{\partial v}{\partial x} + v \frac{\partial v}{\partial y} \right) = -\frac{\partial p}{\partial y} + \frac{\partial}{\partial y} \left[(\mu + \mu_T) 2 \frac{\partial v}{\partial y} \right] + \frac{\partial}{\partial x} \left[(\mu + \mu_T) \left(\frac{\partial u}{\partial y} + \frac{\partial v}{\partial x} \right) \right] \quad (4.1c)$$

where u and v are the mean velocity components in the x and y directions respectively, p is the mean pressure, ρ is the density, μ is the laminar viscosity, and μ_T is the eddy viscosity.

Eddy Viscosity Model

An algebraic eddy viscosity model is used. Only a model for the outer region of the boundary-layer is required in this approach. The model developed by Clauser [25] was chosen:

$$\mu_T = 0.0168 \rho U_e \delta^* \quad (4.2)$$

where U_e is the velocity at the edge of the boundary-layer and δ^* is the displacement thickness. This turbulence model has proven to be effective in the past and it was confirmed in the present work. It is important to note that, although an algebraic eddy viscosity model was used here because of its easy implementation at this development stage, other models can be used with the appropriate differential equations combined with the present treatment of the near-wall region.

Finite Element Method

The Finite Element method is used to solve the previous equations using a penalty approach to eliminate the pressure at the solution step and reduce the number of dependent variables to the two velocity components. The pressure is evaluated at the post-processing step. The assembly of the element matrices for all the elements gives the global system matrix in which the pressure matrix is constructed using a consistent approach in order to avoid the spurious pressure checkerboard mode. The linear set of non-linear equations is solved by LU decomposition in an out-of-core profile algorithm. The non-linear character of the equations requires an iterative strategy to converge to the final solution. The method of successive substitutions is employed in the initial iterations until the residual falls in the radius of convergence of the Newton-Raphson method, which converges quadratically to the numerically "exact" solution.

For 2D problems, one of the best elements is the 9-node quadrilateral, which assumes biquadratic velocity and linear discontinuous pressure interpolation functions. This element was chosen for the discretization in the present work. This FEM formulation and the solution techniques have been implemented in the excellent software package FIDAP [47], and this program is used for all calculations presented in the last section.

Boundary Conditions

As mentioned previously, one of the advantages of the Finite Element method is the implementation of the boundary conditions. One can specify values for the velocity components (essential conditions) or values for the surface tractions (natural conditions). An exact or approximate velocity profile is imposed at the inlet, therefore the values for the two velocity components are used as boundary conditions. Because of the slip velocity assumed in the treatment of the near-wall region, the velocity profile at the inlet must be modified near the

wall to satisfy the condition of a pseudolaminar velocity profile which sets the velocity gradient at the wall to be equal to the ratio of the wall shear stress and the eddy viscosity. On all solid surfaces, the wall shear stress is imposed along with the zero normal velocity condition. The traction-free boundary conditions are used at the outlet of the domain and for an external flow outer boundary enforcing a natural extrapolation scheme.

4.2 2D Near-Wall Formulation

Integral Equation

The conservation of mass and the conservation of momentum along the x-axis are imposed on a control volume of finite height (H) and infinitesimal base (dx) neglecting the pressure variation normal to the wall. The integral equation is written as:

$$\frac{d}{dx} \int_0^H u^2 dy - u_H \frac{d}{dx} \int_0^H u dy = -\frac{H}{\rho} \frac{dp}{dx} + \frac{\tau_H - \tau_w}{\rho} \quad (4.3)$$

where $u(y)$ is a parametrized velocity profile, u_H and τ_H are respectively the velocity and the shear stress at the upper limit of the inner strip, and τ_w is the wall shear stress.

Velocity Profile

The range of applicability of an integral method depends on the velocity profile, or more specifically on the shape of the profile. Good predictions do not require a perfect representation of the velocity because the profile is integrated, and part of the error is smeared out. For the inner region of 2D turbulent flows over a smooth surface, a universal empirical relation is available: the Law of the Wall. This equation gives a good representation of the velocity except in the laminar sub-layer, which is small and can thus be neglected in the evaluation of the integrals.

Using the displacement thickness as characteristic dimension, the Law of the Wall is written as

$$\frac{u}{U_e} = A \ln(C_{LW} A Re_{\delta^*} \eta) \quad (4.4)$$

with $C_{LW} = 3.06$ $\eta = \frac{y}{\delta^*}$ $Re_{\delta^*} = \frac{\rho U_e \delta^*}{\mu}$ $A = \frac{1}{\kappa} \sqrt{\frac{\tau_w}{\rho U_e^2}}$

The parameter A can be interpreted as a normalized wall shear stress.

Differential Equation

Equation 4.3 can be rearranged as follows:

$$\frac{d}{dx} \left[U_e \text{Re}_{\delta^*} \int_0^{\eta_H} \left(\frac{u}{U_e} \right)^2 d\eta \right] - u_H \frac{d}{dx} \left[\text{Re}_{\delta^*} \int_0^{\eta_H} \frac{u}{U_e} d\eta \right] = - \frac{\eta_H \text{Re}_{\delta^*} dp}{\rho U_e dx} + \frac{\tau_H - \tau_w}{\mu} \quad (4.5)$$

Evaluating the integrals using equation 4.4, the following relations are obtained:

$$F_1 = \int_0^{\eta_H} \frac{u}{U_e} d\eta = A \eta_H (F_3 - 1) \quad (4.6a)$$

$$F_2 = \int_0^{\eta_H} \left(\frac{u}{U_e} \right)^2 d\eta = A^2 \eta_H (F_3^2 - 2F_3 + 2) \quad (4.6b)$$

with
$$F_3 = \ln(C_{LW} A \text{Re}_{\delta^*} \eta_H) \quad (4.6c)$$

Therefore,

$$\frac{dF_1}{dx} = \eta_H F_3 \frac{dA}{dx} + \frac{A \eta_H d\text{Re}_{\delta^*}}{\text{Re}_{\delta^*} dx} \quad (4.7a)$$

$$\frac{dF_2}{dx} = \frac{2(A F_1 + F_2)}{A} \frac{dA}{dx} + \frac{2A F_1 d\text{Re}_{\delta^*}}{\text{Re}_{\delta^*} dx} \quad (4.7b)$$

Isolating the normalized wall shear stress derivative, one obtains:

$$\frac{dA}{dx} = \frac{1}{F_4} \left(\frac{\tau_H - \tau_w}{\mu U_e \text{Re}_{\delta^*}} - \frac{\eta_H dp}{\rho U_e^2 dx} - \frac{F_2 dU_e}{U_e dx} - \frac{A \eta_H F_3}{\text{Re}_{\delta^*}} \left(A F_3 - \frac{u_H}{U_e} \right) \frac{d\text{Re}_{\delta^*}}{dx} \right) \quad (4.8)$$

where
$$F_4 = \frac{2(A F_1 + F_2)}{A} - \eta_H F_3 \frac{u_H}{U_e} \quad (4.9)$$

The right-hand side contains information readily available from the Finite Element solution of the Navier-Stokes equations except for the unknown normalized wall shear stress.

The choice of location of the upper limit of the inner strip (η_{1i}) is arbitrary, and values in the range [2.0,3.0] proved effective for the problems considered in this work.

Numerical Scheme

From the inlet (initial station along the wall) where the skin friction coefficient (and therefore A) is known, the values of A at the following stations are computed by marching in space along the wall. The solution of the first-order differential equation of the form

$$\frac{dA}{dx} = f(x, A) \quad (4.10)$$

was achieved by the second order Runge-Kutta scheme:

$$A_i^* = A_{i-1} + \Delta x f(x_{i-1}, A_{i-1}) \quad (4.11a)$$

$$A_i = A_{i-1} + 0.5 \Delta x \{ f(x_{i-1}, A_{i-1}) + f(x_i, A_i^*) \} \quad (4.11b)$$

4.3 2D Computational Procedure

The Finite Element method combined with the inner strip integral formulation was implemented in a procedure called FENSIE (Finite Element Navier-Stokes Integral Equation). First, an inviscid solution is computed when required; it depends on the information available about the geometry and the flow conditions for the problem considered. It also depends on the method available to obtain the initial guess for the wall shear stress and the eddy viscosity. An integral method, like the Moses strip-integral method, can provide very good first approximations reducing the number of iterations to reach the numerically "exact" solution. If an integral method is used, an inviscid solution is needed to provide an approximate edge velocity distribution. The inviscid flow field is also a better initial velocity field to start the computation of the Navier-Stokes solution compared to a zero initial velocity field, so it can considerably decrease the time for convergence.

The Navier-Stokes solution is then computed using the approximate distribution for the wall shear stress and the eddy viscosity. For each station along the surface, the velocity profile is then integrated to get the updated displacement thickness, and consequently an improved eddy viscosity distribution for the next Navier-Stokes computation. At the same time, the values for the velocity and the shear stress at the upper limit of the inner strip are extracted from the

velocity field. The pressure gradient at mid-strip is also extracted from the pressure field. With this information, a corrected wall shear stress distribution is computed with the inner strip integral method. This procedure is repeated until convergence.

4.4 2D FENSIE Results

Wieghardt-Tillman Flow

The first case studied is the flow over a thin flat plate with the experimental measurements obtained by Wieghardt and Tillmann [51]. Information concerning the geometry of the computational domain, the flow conditions, and the boundary conditions is shown in Figure 4.1. A relatively coarse mesh is used for the discretization of the domain in the transverse direction. Convergence was achieved in two procedure-iterations starting with an initial guess obtained from the Moses strip-integral method. A version of the Moses method was implemented in a program called STRIP2D, and the integral predictions are compared with the present predictions. The results for the skin friction coefficient are shown in Figure 4.2, while Figure 4.3 presents the results for the displacement thickness. The FENSIE predictions are in good agreement with the measurements. They are similar to the STRIP2D integral predictions, which is not surprising because integral methods prove to be accurate for turbulent boundary-layer flows with "simple" strains.

Samuel-Joubert Flow

The second experiment used for the validation is the flow over a flat surface with a moderate adverse-pressure gradient designed by Samuel and Joubert [52]. Information concerning the geometry of the computational domain, the flow conditions, and the boundary conditions is shown in Figure 4.4. Here, the number of nodes in the transverse direction was increased to insure an adequate representation of the flow near the top and bottom walls. Convergence was also achieved in two iterations starting with a Moses method initial distribution. The results for the skin friction coefficient are shown in Figure 4.5, and Figure 4.6 presents the results for the displacement thickness. These figures show good agreement except near the end of the domain when the pressure gradient becomes stronger and the flow approaches separation.

Schubauer-Klebanoff Flow

The FENSIE procedure was also applied to the flow about an airfoil-like body with a strong adverse-pressure gradient studied by Schubauer and Klebanoff [53]. Information about the computational domain, the flow conditions, and the boundary conditions is presented in Figure 4.7. Convergence was also achieved in two iterations starting with a Moses method initial distribution. The results for the skin friction coefficient and the displacement thickness are shown in Figures 4.8 and 4.9. An excellent agreement is achieved with a relatively coarse mesh over the entire domain even when approaching separation. This case gives a good example of the importance of solving the Navier-Stokes equations for flows with "extra" effects. The STRIP2D integral results deviates considerably near the end of the domain when approaching separation, while the FENSIE predictions for the skin friction coefficient are in excellent agreement with the experimental measurements.

CHAPTER 5

THREE-DIMENSIONAL NAVIER-STOKES COMPUTATIONAL PROCEDURE

The new approach to treat the near-wall region was implemented in a computational procedure for solving the Reynolds Averaged Navier-Stokes equations for flows in or about 3D geometries. The procedure is based on the Finite Element method using natural wall boundary conditions which are obtained from the solution of two 1-strip-integral equations for the inner region. The mathematical developments of the method are presented in the first two sections, while the procedure is explained in the third section and the numerical predictions are contained in the last section.

5.1 3D Navier-Stokes Solver

Equations

The mathematical model consists of the continuity equation and the momentum equations:

$$\frac{\partial u}{\partial x} + \frac{\partial v}{\partial y} + \frac{\partial w}{\partial z} = 0 \quad (5.1a)$$

$$\begin{aligned} \rho \left(u \frac{\partial u}{\partial x} + v \frac{\partial u}{\partial y} + w \frac{\partial u}{\partial z} \right) &= -\frac{\partial p}{\partial x} + \frac{\partial}{\partial x} \left[(\mu + \mu_T) 2 \frac{\partial u}{\partial x} \right] \\ &+ \frac{\partial}{\partial y} \left[(\mu + \mu_T) \left(\frac{\partial u}{\partial y} + \frac{\partial v}{\partial x} \right) \right] + \frac{\partial}{\partial z} \left[(\mu + \mu_T) \left(\frac{\partial u}{\partial z} + \frac{\partial w}{\partial x} \right) \right] \end{aligned} \quad (5.1b)$$

$$\begin{aligned} \rho \left(u \frac{\partial v}{\partial x} + v \frac{\partial v}{\partial y} + w \frac{\partial v}{\partial z} \right) &= -\frac{\partial p}{\partial y} + \frac{\partial}{\partial y} \left[(\mu + \mu_T) 2 \frac{\partial v}{\partial y} \right] \\ &+ \frac{\partial}{\partial x} \left[(\mu + \mu_T) \left(\frac{\partial u}{\partial y} + \frac{\partial v}{\partial x} \right) \right] + \frac{\partial}{\partial z} \left[(\mu + \mu_T) \left(\frac{\partial v}{\partial z} + \frac{\partial w}{\partial y} \right) \right] \end{aligned} \quad (5.1c)$$

$$\begin{aligned} \rho \left(u \frac{\partial w}{\partial x} + v \frac{\partial w}{\partial y} + w \frac{\partial w}{\partial z} \right) &= -\frac{\partial p}{\partial z} + \frac{\partial}{\partial z} \left[(\mu + \mu_T) 2 \frac{\partial w}{\partial z} \right] \\ &+ \frac{\partial}{\partial x} \left[(\mu + \mu_T) \left(\frac{\partial u}{\partial z} + \frac{\partial w}{\partial x} \right) \right] + \frac{\partial}{\partial y} \left[(\mu + \mu_T) \left(\frac{\partial v}{\partial z} + \frac{\partial w}{\partial y} \right) \right] \end{aligned} \quad (5.1d)$$

where u , v and w are the mean velocity components in the x , y and z directions respectively, p is the mean pressure, ρ is the density, μ is the laminar viscosity, and μ_T is the eddy viscosity.

Eddy Viscosity Model

The eddy viscosity is only required in the outer region of the boundary-layer. The model developed by Clauser [25] for 2D flows is extended as a three-dimensional model:

$$\mu_T = 0.0168 \rho U_e \delta_1 \quad (5.2)$$

where U_e is the velocity at the edge of the boundary-layer and δ_1 is the streamwise displacement thickness. Again, one should note that although an algebraic eddy viscosity model was used here because of its easy implementation at this stage, other models can be used with the appropriate differential equations combined with the present treatment of the near-wall region.

Finite Element Method

The Finite Element method is used to solve the previous equations using a penalty approach to eliminate the pressure at the solution step and reduce the number of dependent variables to the three velocity components. This approach is especially useful for 3D simulations to reduce the storage requirements. The pressure is evaluated at the post-processing step. The assembly of the element matrices for all the elements gives the global system matrix in which the pressure matrix is constructed using a consistent approach in order to avoid the spurious pressure checkerboard mode. The linear set of non-linear equations is solved by LU decomposition in an out-of-core profile algorithm. The non-linear character of the equations requires an iterative strategy to converge to the final solution. The method of successive substitutions is employed for the first iterations until the residual falls in the radius of convergence of the Newton-Raphson method, which converges quadratically to the numerically "exact" solution.

For 3D problems, one of the best elements is the 27-node brick, which assumes triquadratic velocity and linear discontinuous pressure interpolation functions. But, in order to reduce the bandwidth and consequently the storage requirements, the 8-node brick, which assumes trilinear velocity and constant pressure, is chosen for the discretization. This FEM formulation and the solution techniques have been implemented in the excellent software package FIDAP [47], and this program is used for all calculations presented in the last section.

Boundary Conditions

As mentioned previously, one of the advantages of the Finite Element method is the implementation of the boundary conditions. One can specify values for the velocity components (essential conditions) or values for the surface tractions (natural conditions). An exact or approximate velocity profile is imposed at the inlet, and therefore the values for the three velocity components are used as boundary conditions. Because of the slip velocity assumed in the treatment of the near-wall region, the velocity profile at the inlet must be modified near the wall to satisfy the condition of pseudolaminar velocity profile, which sets the velocity gradients at the wall to be equal to the ratio of the wall shear stress component and the eddy viscosity in the streamwise and crosswise directions respectively. On all solid surfaces, the wall shear stress is imposed along with the zero normal velocity condition. The traction-free boundary conditions are used at the outlet of the domain and for an external flow outer boundary enforcing a natural extrapolation scheme.

Furthermore, for the studied cases presented in the last section, essential boundary conditions had to be imposed on the side boundaries because the computational domain is limited to a finite region inside the limiting physical boundaries. The velocity profiles obtained by the 3D Law of the Wake presented in Chapter 3 are used for all stations of the side boundaries.

5.2 3D Near-Wall Formulation

Integral Equations

The conservation of mass and the conservation of momentum along both axes, x and z, are imposed on a control volume of finite height (H) and infinitesimal base (dx by dz) neglecting the pressure variation normal to the wall. The integral equations written in Cartesian coordinates are then:

$$\frac{\partial}{\partial x} \int_0^H u^2 dy + \frac{\partial}{\partial z} \int_0^H uw dy - u_H \left[\frac{\partial}{\partial x} \int_0^H u dy + \frac{\partial}{\partial z} \int_0^H w dy \right] = -\frac{H}{\rho} \frac{\partial p}{\partial x} + \frac{(\tau_{xH} - \tau_{xw})}{\rho} \quad (5.3a)$$

$$\frac{\partial}{\partial z} \int_0^H w^2 dy + \frac{\partial}{\partial x} \int_0^H uw dy - w_H \left[\frac{\partial}{\partial x} \int_0^H u dy + \frac{\partial}{\partial z} \int_0^H w dy \right] = -\frac{H}{\rho} \frac{\partial p}{\partial z} + \frac{(\tau_{zH} - \tau_{zw})}{\rho} \quad (5.3b)$$

where $u(y)$ and $w(y)$ are the components of a parametrized 3D velocity profile, u_H and w_H are the velocity components at the upper limit of the inner strip, τ_{xH} and τ_{zH} are the shear stress components at the upper limit of the inner strip, and τ_{xw} and τ_{zw} are the wall shear stress components.

Based on the experience of other researchers [33], it was decided to use a non-orthogonal streamline coordinates system. One axis is set along the external streamlines while the direction of the other axis depends on the geometry and the flow conditions. Thus, the equations become:

$$\begin{aligned} & \frac{1}{q} \frac{\partial}{\partial X} \left(\frac{q}{h_x} \int_0^H \bar{U}^2 dy \right) + \frac{1}{q} \frac{\partial}{\partial Z} \left(\frac{q}{h_z} \int_0^H \bar{U} \bar{W} dy \right) - \frac{\bar{U}_H}{q} \left[\frac{\partial}{\partial X} \left(\frac{q}{h_x} \int_0^H \bar{U} dy \right) + \frac{\partial}{\partial Z} \left(\frac{q}{h_z} \int_0^H \bar{W} dy \right) \right] \\ & + K_1 \int_0^H \bar{U}^2 dy + K_2 \int_0^H \bar{W}^2 dy + K_3 \int_0^H \bar{U} \bar{W} dy = \frac{(\bar{\tau}_{xH} - \bar{\tau}_{xw})}{\rho} + \frac{H}{\rho} \left(a_1 \frac{\partial p}{\partial X} + a_2 \frac{\partial p}{\partial Z} \right) \end{aligned} \quad (5.4a)$$

$$\begin{aligned} & \frac{1}{q} \frac{\partial}{\partial Z} \left(\frac{q}{h_z} \int_0^H \bar{W}^2 dy \right) + \frac{1}{q} \frac{\partial}{\partial X} \left(\frac{q}{h_x} \int_0^H \bar{U} \bar{W} dy \right) - \frac{\bar{W}_H}{q} \left[\frac{\partial}{\partial X} \left(\frac{q}{h_x} \int_0^H \bar{U} dy \right) + \frac{\partial}{\partial Z} \left(\frac{q}{h_z} \int_0^H \bar{W} dy \right) \right] \\ & + L_1 \int_0^H \bar{U}^2 dy + L_2 \int_0^H \bar{W}^2 dy + L_3 \int_0^H \bar{U} \bar{W} dy = \frac{(\bar{\tau}_{zH} - \bar{\tau}_{zw})}{\rho} + \frac{H}{\rho} \left(b_1 \frac{\partial p}{\partial X} + b_2 \frac{\partial p}{\partial Z} \right) \end{aligned} \quad (5.4b)$$

with $q = h_x h_z \sin \lambda$ $K_1 = -\cos \lambda L_1$ $L_2 = -\cos \lambda K_2$

$$K_2 = \frac{1}{q \sin \lambda} \left[\frac{\partial(h_x \cos \lambda)}{\partial Z} - \frac{\partial h_z}{\partial X} \right] \quad K_3 = \frac{1}{q \sin \lambda} \left[(1 + \cos^2 \lambda) \frac{\partial h_x}{\partial Z} - 2 \cos \lambda \frac{\partial h_z}{\partial X} \right]$$

$$L_1 = \frac{1}{q \sin \lambda} \left[\frac{\partial(h_z \cos \lambda)}{\partial X} - \frac{\partial h_x}{\partial Z} \right] \quad L_3 = \frac{1}{q \sin \lambda} \left[(1 + \cos^2 \lambda) \frac{\partial h_z}{\partial X} - 2 \cos \lambda \frac{\partial h_x}{\partial Z} \right]$$

$$a_1 = \frac{-h_z}{q \sin \lambda} \quad a_2 = \frac{h_x \cos \lambda}{q \sin \lambda} \quad b_1 = \frac{h_z \cos \lambda}{q \sin \lambda} \quad b_2 = \frac{-h_x}{q \sin \lambda}$$

where X and Z are the non-orthogonal coordinates, h_x and h_z are the metrics of the transformation, λ is the angle between the non-orthogonal axes, \bar{U} and \bar{W} are the non-orthogonal velocity components, \bar{U}_H and \bar{W}_H are the non-orthogonal velocity components at the upper limit of the inner strip, $\bar{\tau}_{xH}$ and $\bar{\tau}_{zH}$ are the non-orthogonal shear stress components at the upper limit of the inner strip, and $\bar{\tau}_{xw}$ and $\bar{\tau}_{zw}$ are the non-orthogonal wall shear stress

components. The metrics, h_x and h_z , and λ are computed numerically at the pre-processing step. The use of non-orthogonal coordinates and the numerical calculation of the metrics insure complete freedom in the creation of the computational domain.

Velocity Profile

The applicability of an integral method depends on the assumed shape of the velocity profile. Good predictions do not require a perfect representation of the velocity because the profile is integrated and part of the error is smeared out. The usual way to express the 3D velocity profile is by streamline orthogonal coordinates [33]. The total velocity is divided into 2 components: the first component is in the direction of the tangent to the external streamlines; and the second component is perpendicular to the first one. Therefore, the velocity profile must be transformed to the non-orthogonal coordinates system before integration. Based on the conclusions of the excellent review of three-dimensional Laws of the Wall by Ölçmen and Simpson [34,35], it was decided to use the Johnston Law of the Wall [36], which assumes a triangular model for the crosswise velocity. The velocity profiles are written as:

$$\frac{U}{U_e} = A \cos \beta_w \ln(C_{LW} A Re_{\delta_1} \eta) \quad (5.5)$$

$$\text{and} \quad \frac{W}{U_e} = \frac{U}{U_e} \tan \beta_w \quad \text{for } \eta < \eta_{mc} \quad (5.6a)$$

$$\text{or} \quad \frac{W}{U_e} = C_{mc} \left(1 - \frac{U}{U_e}\right) \quad \text{for } \eta > \eta_{mc} \quad (5.6b)$$

$$\text{with} \quad C_{mc} = \frac{W_{mc}}{U_e - U_{mc}}$$

$$\text{and} \quad C_{LW} = 3.06 \quad \eta = \frac{y}{\delta_1} \quad Re_{\delta_1} = \frac{\rho U_e \delta_1}{\mu} \quad A = \frac{1}{\kappa} \sqrt{\frac{\tau_w}{\rho U_e^2}}$$

where U is the orthogonal streamwise velocity component, W is the orthogonal crosswise velocity component, U_e is the edge velocity, A is a normalized wall shear stress, β_w is the wall crossflow angle, δ_1 is the streamwise displacement thickness, η_{mc} is the location of maximum crosswise velocity, and U_{mc} and W_{mc} are respectively the orthogonal streamwise and crosswise velocity at this location.

Differential Equations

The two momentum integral equations written in non-orthogonal streamline coordinates can be rearranged as follows:

$$\frac{\partial G_{C1}}{\partial X} - \frac{\bar{U}_H}{U_e} \frac{\partial G_{A1}}{\partial X} = F_{X1} = \frac{h_x (\bar{\tau}_{xH} - \bar{\tau}_{xw})}{\mu U_e Re_{\delta 1}} + \frac{h_x \eta_H}{\rho U_e^2} \left(a_1 \frac{\partial p}{\partial X} + a_2 \frac{\partial p}{\partial Z} \right) - h_x (K_1 G_{C1} + K_2 G_{E1} + K_3 G_{D1})$$

$$- \frac{h_x}{q U_e Re_{\delta 1}} \left\{ G_{C1} \frac{\partial}{\partial X} \left(\frac{q U_e Re_{\delta 1}}{h_x} \right) - \bar{U}_H G_{A1} \frac{\partial}{\partial X} \left(\frac{q Re_{\delta 1}}{h_x} \right) + \frac{\partial}{\partial Z} \left(\frac{q U_e Re_{\delta 1} G_{D1}}{h_z} \right) - \bar{U}_H \frac{\partial}{\partial Z} \left(\frac{q Re_{\delta 1} G_{B1}}{h_z} \right) \right\} \quad (5.7a)$$

$$\frac{\partial G_{D1}}{\partial X} - \frac{\bar{W}_H}{U_e} \frac{\partial G_{A1}}{\partial X} = F_{Z1} = \frac{h_x (\bar{\tau}_{zH} - \bar{\tau}_{zw})}{\mu U_e Re_{\delta 1}} + \frac{h_x \eta_H}{\rho U_e^2} \left(b_1 \frac{\partial p}{\partial X} + b_2 \frac{\partial p}{\partial Z} \right) - h_x (L_1 G_{C1} + L_2 G_{E1} + L_3 G_{D1})$$

$$- \frac{h_x}{q U_e Re_{\delta 1}} \left\{ G_{D1} \frac{\partial}{\partial X} \left(\frac{q U_e Re_{\delta 1}}{h_x} \right) - \bar{W}_H G_{A1} \frac{\partial}{\partial X} \left(\frac{q Re_{\delta 1}}{h_x} \right) + \frac{\partial}{\partial Z} \left(\frac{q U_e Re_{\delta 1} G_{E1}}{h_z} \right) - \bar{W}_H \frac{\partial}{\partial Z} \left(\frac{q Re_{\delta 1} G_{B1}}{h_z} \right) \right\} \quad (5.7b)$$

with

$$G_{A1} = \int_0^{\eta_H} \frac{\bar{U}}{U_e} d\eta$$

$$G_{B1} = \int_0^{\eta_H} \frac{\bar{W}}{U_e} d\eta$$

$$G_{C1} = \int_0^{\eta_H} \left(\frac{\bar{U}}{U_e} \right)^2 d\eta$$

$$G_{D1} = \int_0^{\eta_H} \frac{\bar{U} \bar{W}}{U_e^2} d\eta$$

$$G_{E1} = \int_0^{\eta_H} \left(\frac{\bar{W}}{U_e} \right)^2 d\eta$$

The transformation between orthogonal streamline coordinates and non-orthogonal streamline coordinates gives the following relations:

$$\bar{U} = U - \frac{W}{\tan \lambda} \quad \text{and} \quad \bar{W} = \frac{W}{\sin \lambda}$$

$$\bar{\tau}_x = \tau_x - \frac{\tau_z}{\tan \lambda} \quad \text{and} \quad \bar{\tau}_z = \frac{\tau_z}{\sin \lambda}$$

and
$$G_{A1} = F_{A1} - \frac{F_{B1}}{\tan \lambda} \quad (5.8a)$$

$$G_{B1} = \frac{F_{B1}}{\sin \lambda} \quad (5.8b)$$

$$G_{C1} = F_{C1} - \frac{2F_{D1}}{\tan \lambda} + \frac{F_{E1}}{\tan^2 \lambda} \quad (5.8c)$$

$$G_{D1} = \frac{1}{\sin \lambda} \left(F_{D1} - \frac{F_{E1}}{\tan \lambda} \right) \quad (5.8d)$$

$$G_{E1} = \frac{F_{E1}}{\sin^2 \lambda} \quad (5.8e)$$

with
$$F_{A1} = \int_0^{\eta_H} \frac{U}{U_e} d\eta$$

$$F_{B1} = \int_0^{\eta_H} \frac{W}{U_e} d\eta$$

$$F_{C1} = \int_0^{\eta_H} \left(\frac{U}{U_e} \right)^2 d\eta$$

$$F_{D1} = \int_0^{\eta_H} \frac{UW}{U_e^2} d\eta$$

$$F_{E1} = \int_0^{\eta_H} \left(\frac{W}{U_e} \right)^2 d\eta$$

Using the expressions for the velocity from equations (5.5), (5.6a) and (5.6b), one finds:

$$F_{A1} = \eta_H F_1 \quad (5.9)$$

$$F_{C1} = \eta_H (F_1^2 + A^2 \cos^2 \beta_w) \quad (5.10)$$

and
$$F_{B1} = F_{A1} \tan \beta_w \quad (5.11a)$$

$$F_{D1} = F_{C1} \tan \beta_w \quad \text{for } \eta_H < \eta_{mc} \quad (5.12a)$$

$$F_{E1} = F_{D1} \tan \beta_w \quad (5.13a)$$

or
$$F_{B1} = F_{B0} + C_{mc} (\eta_H - \eta_{mc} - F_{A1} + F_{A0}) \quad (5.11b)$$

$$F_{D1} = F_{D0} + C_{mc} (F_{A1} - F_{A0} - F_{C1} + F_{C0}) \quad \text{for } \eta_H > \eta_{mc} \quad (5.12b)$$

$$F_{E1} = F_{E0} + C_{mc}^2 (\eta_H - \eta_{mc} - 2(F_{A1} - F_{A0}) + F_{C1} - F_{C0}) \quad (5.13b)$$

with $F_1 = A \cos \beta_w \{ \ln(C_{LW} A Re_{\delta 1} \eta_H) - 1 \}$ (5.14)

$$F_{A0} = \eta_{mc} F_0 \quad (5.15)$$

$$F_{B0} = F_{A0} \tan \beta_w \quad (5.16)$$

$$F_{C0} = \eta_{mc} (F_0^2 + A^2 \cos^2 \beta_w) \quad (5.17)$$

$$F_{D0} = F_{C0} \tan \beta_w \quad (5.18)$$

$$F_{E0} = F_{D0} \tan \beta_w \quad (5.19)$$

$$F_0 = A \cos \beta_w \{ \ln(C_{LW} A Re_{\delta 1} \eta_{mc}) - 1 \} \quad (5.20)$$

The transformation of the X-derivatives in the left-hand side of equations (5.7a) and (5.7b) gives the following relations:

$$\frac{\partial G_{A1}}{\partial X} = \frac{\partial F_{A1}}{\partial X} - \frac{1}{\tan \lambda} \frac{\partial F_{B1}}{\partial X} + \frac{G_{B1}}{\sin \lambda} \frac{\partial \lambda}{\partial X} \quad (5.21)$$

$$\frac{\partial G_{C1}}{\partial X} = \frac{\partial F_{C1}}{\partial X} - \frac{2}{\tan \lambda} \frac{\partial F_{D1}}{\partial X} + \frac{1}{\tan^2 \lambda} \frac{\partial F_{E1}}{\partial X} + \frac{2G_{D1}}{\sin \lambda} \frac{\partial \lambda}{\partial X} \quad (5.22)$$

$$\frac{\partial G_{D1}}{\partial X} = \frac{1}{\sin \lambda} \left\{ \frac{\partial F_{D1}}{\partial X} - \frac{1}{\tan \lambda} \frac{\partial F_{E1}}{\partial X} + (G_{E1} - \cos \lambda G_{D1}) \frac{\partial \lambda}{\partial X} \right\} \quad (5.23)$$

The expressions for the derivatives of equations (5.9) to (5.13) are used to obtain the expanded expressions of the derivatives in equations (5.21) to (5.23), which are then introduced in equations (5.7a) and (5.7b) giving the following matrix form for the final set of equations:

$$C_{j1} \frac{\partial A}{\partial X} + C_{j2} \frac{\partial \beta_w}{\partial X} = R_j \quad j=1,2 \quad (5.24)$$

The right-hand sides contain all derivatives with respect to the crosswise direction, and all derivatives with respect to the streamwise direction of the known variables. The coefficients and the right-hand sides are functions of the two unknowns, of information readily available from

the Finite Element solution of the Navier-Stokes equations, and of the form of the mesh, which is described by the shape of the external streamlines and the metrics of the transformation to non-orthogonal coordinates. The choice of location of the upper limit of the inner strip (η_H) is arbitrary, and values in the range [1.0,2.0] proved effective for the problems considered in this work.

The solution of the matrix system by Gauss elimination leads to the following expressions for each derivative:

$$\frac{\partial \beta_w}{\partial X} = f^1(X, Z, A, \beta_w) = \frac{C_{11}R_2 - C_{21}R_1}{C_{11}C_{22} - C_{21}C_{12}} \quad (5.25a)$$

$$\frac{\partial A}{\partial X} = f^2(X, Z, A, \beta_w) = \frac{R_1}{C_{11}} - \frac{C_{12}}{C_{11}} \frac{\partial \beta_w}{\partial X} \quad (5.25b)$$

Numerical Scheme

The previous set of equations is hyperbolic, and the characteristics are located between the external streamlines and the wall streamlines. The discretization of the surface must obey the CFL condition, which requires that the computational domain of dependence should include the physical domain of dependence. Starting from the initial location where the solution is known along the entire line, the solution is computed for the normalized wall shear stress and the wall crossflow angle over the wall using a space marching technique. Boundary conditions are also necessary at all locations where the flow enters the computational domain. The solution of the set of first-order differential equations is achieved by the second order Runge-Kutta scheme. The first part of integration is:

$$\beta_{w,i,k}^* = \beta_{w,i-1,k} + \Delta x f_{i-1,k}^1 \quad (5.26a)$$

$$A_{i,k}^* = A_{i-1,k} + \Delta x f_{i-1,k}^2 \quad (5.26b)$$

The second part of integration is then:

$$\beta_{w,i,k} = \beta_{w,i-1,k} + 0.5 \Delta x \{ f_{i-1,k}^1 + f_{i,k}^{1*} \} \quad (5.27a)$$

$$A_{i,k} = A_{i-1,k} + 0.5 \Delta x \{ f_{i-1,k}^2 + f_{i,k}^{2*} \} \quad (5.27b)$$

5.3 3D Computational Procedure

The 3D Finite Element method combined with the 3D inner strip integral formulation was implemented in a procedure called FENSIES (Finite Element Navier-Stokes Integral EquationS). First, an inviscid solution is computed when required; it depends on the information available about the geometry and the flow conditions for the problem considered. It also depends on the method available to obtain the initial guess for the wall shear stress and the eddy viscosity. An integral method, like the STRIP3D integral method presented in Chapter 3, can provide very good first approximations, reducing the number of iterations to reach the numerically "exact" solution. If an integral method is used, an inviscid solution is needed to provide an approximate edge velocity distribution. The inviscid flow field is also a better initial velocity field to start the computation of the Navier-Stokes solution compared to a zero initial velocity field, so it can considerably decrease the time for convergence.

The Navier-Stokes solution is then computed using the approximate distribution for the wall shear stress and the eddy viscosity. For each station along the surface, the velocity profile is then integrated to get the updated streamwise displacement thickness, and consequently an improved eddy viscosity distribution for the next Navier-Stokes computation. At the same time, the values for the velocity and shear stress components at the upper limit of the inner strip are extracted from the velocity field. The pressure gradient components at mid-strip are also extracted from the pressure field. With this information, a corrected wall shear stress distribution is computed with the inner strip integral method through the skin friction coefficient and wall crossflow angle. This procedure is repeated until convergence.

5.4 3D FENSIES Results

Van den Berg-Elsenaar Flow

The flow over a flat surface with a 35° sweep angle under infinite swept-wing conditions in an adverse-pressure gradient was investigated by Van den Berg and Elsenaar [48,49]. Information concerning the computational domain and the flow conditions is presented in Figure 5.1. The width of the region is 0.10 compared to the length, which is about 0.50. The flow was computed for the first 6 stations, and predictions are presented for the first iteration, starting with values for the wall shear stress and the eddy viscosity obtained by the STRIP3D method. The results for the skin friction coefficient, wall crossflow angle, and streamwise

displacement thickness along two streamlines are shown in Figs. 5.2 to 5.4, along with the experimental measurements, and the numerical results of the differential methods of Cebeci et al, and Patel et al. These methods solve the boundary-layer equations using the isotropic two-layer eddy-viscosity model of Cebeci, which includes the Van Driest damping factor and a low-Reynolds number correction. Cebeci's method uses transformed equations written in Cartesian coordinates solved by the Keller box scheme, using two-point differences and a Newton-Raphson procedure.

The 3D results do not show the same level of agreement with the measurements as for the 2D cases, but the predictions are similar to the results of the other differential methods. A few reasons might explain the disparities. First, the present results were obtained with a coarse discretization in the streamwise and crosswise directions. Second, the results are presented after one iteration. Third, the STRIP3D integral predictions were used to evaluate the velocity profiles for the stations at the inlet and on the side boundaries, where the values for the velocity components obtained by the 3D Law of the Wake were imposed as essential boundary conditions. The flow is somehow constrained by the conditions imposed from the boundary-layer solution. The computational domain was also restricted to a physical region of the flow where the "extra" effects are small, and the predictions are naturally similar to the integral method predictions for this turbulent boundary-layer flow. Therefore, no appreciable advantage is seen here from the resolution of the Navier-Stokes equations with the present near-wall treatment.

Müller-Krause Flow

The second case is the flow over a flat surface with an adverse-pressure gradient in the streamwise direction and an induced pressure gradient in the crosswise direction, studied by Müller and Krause [50]. Information concerning the geometry of the computational domain and the flow conditions is presented in Figure 5.5. The predictions are also presented after a single iteration, starting from the STRIP3D integral distribution for the wall shear stress and the eddy viscosity. The predictions for the skin friction coefficient, wall crossflow angle, and streamwise displacement thickness are respectively shown in Figures 5.6 to 5.8 for the line $x=0.4$, and in Figures 5.9 to 5.11 for the line $x=0.6$, along with the experimental measurements, and the predictions of three other numerical methods as presented in Ref. 21. Cross' integral method makes use of the entrainment equation with an algebraic equation for the entrainment velocity, and Coles' velocity profiles. The numerical integration is done with the second-order Runge-

Kutta scheme. Müller's method solves the boundary-layer equations in Cartesian coordinates using an isotropic eddy-viscosity model based on Michel's mixing length and Van Driest damping factor, and the numerical solution is obtained by semi-implicit schemes.

Here again, the same comments can be applied to the present analysis. The results for the parameters of the FENSIES solution show similar trends as the STRIP3D results due to the strong constraint of the boundary conditions imposed through the STRIP3D predictions.

CHAPTER 6

CONCLUSIONS AND PERSPECTIVES

New computational procedures have been developed for the simulation of incompressible wall-bounded turbulent flows in or about two-dimensional (2D) or three-dimensional (3D) geometries. The present methods are based mainly on two major ideas: the strip-integral method and Clauser's pseudolaminar velocity profile. The strip-integral method proves especially convenient, because integral equations can be obtained for as many control volumes as necessary depending on the number of parameters used in the formulation. This method may be formulated as an integral method, as done previously for 2D laminar and turbulent boundary-layers and as performed in the present work for 3D turbulent boundary-layers, or it may be integrated in a procedure for solving differential equations as done for the present 2D and 3D Navier-Stokes procedures. Clauser's idea is also useful because it enables the computation of turbulent flows by solving the flow with a minimum of nodes in the boundary-layer, while modeling the near-wall region to represent adequately the physics of the flow in the inner region.

The extension of the strip-integral method to 3D incompressible turbulent boundary-layer flows depend mainly on the parameterized velocity profile. One of the best representations of the 3D velocity in orthogonal streamline coordinates is provided by the Johnston Law of the Wall, which uses a triangular model for the crosswise velocity. This velocity profile is a function of the usual parameters (skin friction coefficient, wall crossflow angle, and boundary-layer thickness) and of the location of maximum crosswise velocity, which appears in the expression defining the crosswise velocity. The triangular model offers a good approximation of the crosswise velocity, but it tends to overestimate this component near the location of maximum crosswise velocity. This model shows also a strong dependence between the wall crossflow angle and the location of maximum crosswise velocity, which is numerically sensitive and produces a wavy character shown mainly in the predictions for the wall crossflow angle. Further studies are suggested to explain the numerical sensitivity and to find a smoother parametrized representation of the crosswise velocity near its maximum value.

The validation of the 3D strip-integral method also shows some of the deficiencies in the present formulation. First, for the Van den Berg-Elsenaar case, when the derivatives with

respect to the Z-axis are set to zero, which represents the real experimental conditions, the present results do not show the same level of agreement than the solutions obtained for small ΔZ not neglecting the Z-derivatives. The predictions are still better than the results obtained by Cousteix et al, or Smith, and are similar to Cross' predictions without as much empirical input. Second, the results for the Müller-Krause case show difficulties with the implementation of boundary conditions along the first streamline defining the computational domain. The values for all parameters are obtained from experimental measurements, and their relative inconsistency with the present model causes large oscillations in the predictions for the first streamlines. Third, the eddy viscosity ratio is chosen as a constant for the entire computational domain. A value of $C_{zx}=1.2$ was suggested by Müller and Krause for their experimental case. However, the present results for the wall crossflow angle show that $C_{zx}=1.4$ is a better choice at $x=0.4$, while $C_{zx}=1.0$ is better at $x=0.6$. Therefore, a more sophisticated model accounting implicitly for the anisotropy of the turbulent shear stress is recommended.

Globally, good numerical predictions have been obtained with the present 3D strip-integral method when compared to the results of other methods. One of the main advantages of the strip-integral method is the direct implementation of eddy viscosity models as in differential methods. The turbulence modeling is not hidden in opaque empirical correlations as in conventional integral methods.

Computational procedures solving the Reynolds Averaged Navier-Stokes equations have also been developed using a new treatment of the near-wall region. The flow is solved down to the wall with a slip velocity by imposing the wall shear stress as boundary condition. The approach can be seen as solving the flow for the outer region of the boundary-layer. Thus, only an outer region eddy viscosity model is required, and a small number of nodes is suitable to represent adequately the physics of the flow near solid surfaces, because of the reduced velocity gradient. This proves especially useful for three-dimensional calculations.

The wall shear stress distribution is updated by solving integral equations obtained from the enforcement of conservation of mass and momentum in an integral sense over a thin strip in the near-wall region. The formulation can be seen as a 1-strip-integral equation containing information readily available from the Navier-Stokes solution except for the wall shear stress. The interaction between the Navier-Stokes solver and the integral formulation converges to the numerically "exact" solution in a few iterations depending on the accuracy of the initial guess for the wall shear stress. The present treatment of the near-wall region is different from the

approach in wall-function methods. The velocity or the derivative of the velocity is not matched with the Law of the Wall at a fixed point above the wall, but the Law of the Wall is rather integrated over the inner strip, which tends to decrease the error due to modeling.

The numerical predictions obtained for the 2D benchmark experimental cases show good agreement with the measurements. Furthermore, the results for the Schubauer-Klebanoff experiment demonstrate an excellent agreement even when approaching separation. The present 2D Finite Element Navier-Stokes Integral Equation method is not restricted to boundary-layer flows, and can be applied to attached turbulent flows with "extra" effects, such as flows with curved surfaces and strong adverse-pressure gradient.

The 3D Navier-Stokes computational procedure was applied to the same flows used for the validation of the integral method. The present procedure does not show advantages over the integral method, because the experimental flows are of boundary-layer type, the initial and boundary conditions have been obtained directly from the strip-integral method, and the numerical results are presented after one iteration. At this validation stage, the results confirm the applicability of the present procedure using the new treatment of the near-wall region, but further simulations are necessary to evaluate the extent of applicability. First, previous calculations should be numerically converged to the final solutions for both cases. Second, the computational domain should be extended to cover a larger area of the physical domain. Finally, calculations should be performed for different grids using experimental values for the parameters at the boundaries of the computational domain.

The present work introduced new computational tools for the simulation of turbulent flows. The general strip-integral method shows great advantages over conventional integral methods, and one can see many possibilities for the implementation of this method to other flow applications. The new treatment of the near-wall region brings an important reduction in the number of nodes required to model the flow, and its implementation can easily be seen in procedures based on other types of differential methods.

REFERENCES

1. Anderson, D. A., Tannehill, J. C., Pletcher, R. H., *Computational Fluid Mechanics and Heat Transfer*, Hemisphere Publishing Corp., Washington, DC, 1984.
2. Chapman, D. R., "Computational Aerodynamics Development and Outlook," *AIAA Journal*, Vol. 17, No. 12, December 1979, pp. 1293-1313.
3. Chapman, D. R., "Computers and Wind-Tunnels," *Astronautics & Aeronautics*, Vol. 13, No. 4, April 1975, pp. 22-30.
4. Peterson, V. L., Bailey, F. R., "Close to Real Life," *Aerospace America*, Vol. 26, No. 7, July 1988, pp. 18-24.
5. Carpentier, J., "La Soufflerie Numérique," *La Recherche*, No. 219, March 1990, pp. 274-283.
6. Bradshaw, P. et al., "Experimental Data Needs for Computational Fluid Dynamics--A Position Paper," *Proceedings of the 1980-81 Stanford Conference*, Vol. I, 1981, pp. 23-39.
7. Hinze, J. O., *Turbulence*, 2nd ed., McGraw-Hill, New-York, NY, 1975.
8. Schlichting, H., *Boundary-Layer Theory*, 7th ed., McGraw-Hill, New-York, NY, 1979.
9. Schetz, J. A., *Foundations of Boundary Layer Theory for Momentum, Heat, and Mass Transfer*, Prentice-Hall, Englewood Cliffs, NJ, 1984.
10. Levine, R. D., "Supercomputers," *Scientific American*, Vol. 246, June 1982, pp.118-135.
11. Hillis, W. D., "The Connection Machine," *Scientific American*, Vol. 256, June 1987, pp. 108-115.
12. Boghosian, B. M., "Computational Physics on the Connection Machine," *Computers in Physics*, Jan/Feb 1990.

13. Rogallo, R. S., "Direct Simulation of Homogeneous Turbulence at Low Reynolds Numbers," Proceedings of the 1980-81 Stanford Conference, Vol. II, 1981, pp. 863-864.
14. Schumann, U., Friedrich, R., *Direct and Large Eddy Simulation of Turbulence*, Notes on Numerical Fluid Mechanics, Vol. 15, 1986.
15. Moin, P., Kim, J., "Large-Scale Numerical Simulation of Wall-Bounded Turbulent Shear Flows," Proceedings of the 1980-81 Stanford Conference, Vol. II, 1981, pp. 865-868.
16. Coles, D. E., Hirst, E. A., *Proceedings Computation of Turbulent Boundary Layers-1968 AFOSR-IFP-STANFORD Conference*, 2 Volumes, Stanford University, Stanford, CA, 1969.
17. Reynolds, W. C., "A Morphology of the Prediction Methods," Proceedings of the 1968 Stanford Conference, Vol. 1, 1969, pp. 1-15.
18. Kline, S. J., Cantwell, B. J., Lilley, G. M., *1980-81 AFOSR-HTTM-STANFORD Conference on Complex Turbulent Flows*, 3 Volumes, Stanford University, Stanford, CA, 1981.
19. Ferziger, J. H., Bardina, J., Allen, G., "Overview of Taxonomy: Morphology of the Flows and Computational Methods," Proceedings of the 1980-81 Stanford Conference, Vol. II, 1981, pp. 634-649.
20. Humphreys, D. A., Van den Berg, B., "Three-Dimensional Turbulent Boundary Layer," Proceedings of the 1980-81 Stanford Conference, Vol. I, 1981, pp. 162-169.
21. Van den Berg, B., Humphreys, D. A., Krause, E., Lindhout, J. P. F., *Three-Dimensional Turbulent Boundary Layers - Calculations and Experiments*, Notes on Numerical Fluid Mechanics, Vol. 19, 1988.
22. Moses, H. L., "A Strip-Integral Method for Predicting the Behavior of Turbulent Boundary Layers," Proceedings of the 1968 Stanford Conference, Vol. 1, 1969, pp. 76-82.

23. Caillé, J., Schetz, J. A., "Three-Dimensional Strip-Integral Method for Incompressible Turbulent Boundary Layers," *AIAA Journal*, Vol. 30, No. 5, May 1992, pp.1207-1213.
24. Caillé, J., Schetz, J. A., "New Wall Treatment for the Navier-Stokes Solution of Incompressible Turbulent Wall-Bounded Flows," AIAA Paper 91-1736 presented at the AIAA 22nd Fluid Dynamics, Plasma Dynamics, and Lasers Conference, Honolulu, HI, June 1991.
25. Clauser, F. H., *The Turbulent Boundary Layer*, Advances in Applied Mechanics, Vol. IV, Academic Press, New-York, 1956.
26. Devenport, W. J., Simpson, R. L., "Turbulence Structure near the Nose of a Wing Body Junction," AIAA Paper 87-1310 presented at the AIAA 19th Fluid Dynamics, Plasma Dynamics, and Lasers Conference, Honolulu, HI, June 1987.
27. Schetz, J. A., Favin, S., "Numerical Calculation of Turbulent Boundary Layer with Suction or Injection and Binary Diffusion," *Astronautica Acta*, Vol. 16, No. 6, December 1971, pp. 339-351.
28. Patankar, S. V., Spalding, D. B., "A Calculation Procedure for Heat Transfer by Forced Convection Through Two-Dimensional Uniform-Property Turbulent Boundary Layers on Smooth Impermeable Walls," Proceedings of the 3rd International Heat Transfer Conference (A. I. Ch. E.), Chicago, Vol. II, 1966, pp. 50-63.
29. Cousteix, J., "Integral Techniques," Proceedings of the 1980-81 Stanford Conference, Vol. II, 1981, pp. 650-671.
30. Humphreys, D. A., Lindhout, J. P. F., "Calculation Methods for Three-Dimensional Turbulent Boundary Layers," *Progress in Aerospace Sciences*, Vol. 25, 1988, pp. 107-129.
31. Abbott, D. E., "Application of the Method of Weighted Residuals to the Turbulent Boundary-Layer Equations," Proceedings of the 1968 Stanford Conference, Vol. 1, 1969, pp. 16-29.

32. Pallone, A., "Nonsimilar Solutions of Compressible-Laminar Boundary-Layer Equations with Applications to Upstream-Transpiration Cooling Problem," *Journal of Aerospace Sciences*, Vol. 28, No. 6, June 1961, pp. 449-456.
33. Cousteix, J., Michel, R., "Three-Dimensional Turbulent Boundary Layer Calculations," *Perspectives in Turbulence Studies*, Intl. Symp. DFVLR Research Center, Göttingen, May 11-12, 1987, pp. 439-472.
34. Ölçmen, S., "An Experimental Investigation of a Pressure-Driven Three-Dimensional Turbulent Boundary Layer," Ph.D. Dissertation, Virginia Polytechnic Institute and State University, 1990.
35. Ölçmen, S., Simpson, R. L., "Some Near Wall Features of Three-Dimensional Turbulent Boundary Layers," *Fourth Symposium on Numerical and Physical Aspects of Aerodynamic Flows*, Long Beach, California, January, 1989.
36. Johnston, J. P., "On the Three-Dimensional Turbulent Boundary Layer Generated by Secondary Flow," *Journal of Basic Engineering*, Vol. 82, March 1960, pp. 233-248.
37. Gerald, C. F., Wheatley, P. O., *Applied Numerical Analysis*, 4th ed., Addison-Wesley Publishing Co., Reading, MA, 1989.
38. Thompson, J. F., "Numerical Solution of Flow Problems using Body Fitted Coordinate Systems," in *Computational Fluid Dynamics*, Vol. 1, Hemisphere Publishing Corp., Washington, DC, 1980.
39. Reddy, J. N., *An Introduction to the Finite Element Method*, McGraw-Hill, New-York, NY, 1984 (2nd ed., 1993).
40. Zienkiewicz, O. C., *The Finite Element Method*, 3rd ed., McGraw-Hill, New-York, NY, 1977.
41. Taylor, C., Hughes, T. J. R., *Finite Element Programming of the Navier-Stokes Equations*, Pineridge Press, Swansea, U.K., 1980.

42. Reddy, J. N., "On Penalty Function Methods in the Finite Element Analysis of Flow Problems," *International Journal for Numerical Methods in Fluids*, Vol. 2, No. 2, 1982, pp. 151-171.
43. Reddy, J. N., "Penalty-Finite-Element Analysis of 3-D Navier-Stokes Equations," *Computer Methods in Applied Mechanics and Engineering*, Vol. 35, 1982, pp. 87-106.
44. Engelman, M. S., Sani, R. L., Gresho, P. M., Bercovier, M., "Consistent vs Reduced Quadrature Penalty Methods for Incompressible Media using Several Old and New Elements," *International Journal for Numerical Methods in Fluids*, Vol. 2, No. 1, 1982, pp. 25-42.
45. Caillé, J., Schetz, J. A., "Finite-Element Navier-Stokes Analysis of the Flow About a Finite Plate," *AIAA Journal*, Vol. 27, No. 8, August 1989, pp. 1089-1096.
46. Engelman, M. S., Sani, R. L., Gresho, P. M., "The Implementation of Normal and/or Tangential Boundary Conditions in Finite Element Codes for Incompressible Fluid Flow," *International Journal for Numerical Methods in Fluids*, Vol. 2, 1982, pp. 225-238.
47. Engelman, M. S., "FIDAP: A Fluid Dynamics Analysis Program," *Advances in Engineering Software*, Vol. 4, 1982.
48. Van den Berg, B., Elsenaar, A., *Measurements in a Three-Dimensional Incompressible Turbulent Boundary Layer in an Adverse Pressure Gradient under Infinite Swept Wing Conditions*, NLR TR 72092 U, 1972.
49. Van den Berg, B. et al., "Measurements in an Incompressible Three-Dimensional Turbulent Boundary Layer, under Infinite Swept-Wing Conditions, and Comparison with Theory," *Journal of Fluid Mechanics*, Vol. 70, Part 1, 1975, pp. 127-148.
50. Müller, U. R., "Measurements of the Reynolds Stresses and the Meanflow Field in a Three-Dimensional Pressure-Driven Boundary Layer," *Journal of Fluid Mechanics*, Vol. 119, 1982, pp. 121-153.
51. Wiegardt, K., Tillmann, W., "On the Turbulent Friction Layer for Rising Pressure," *NACA TM 1314* (translation), 1951.

52. Samuel, A. E., Joubert, P. N., "A Boundary Layer Developing in an Increasingly Adverse Pressure Gradient," *Journal of Fluid Mechanics*, Vol. 66, part 3, 1974, pp. 481-505.
53. Schubauer, G. B., Klebanoff, P. S., "Investigation of Separation of the Turbulent Boundary Layer," NACA TN 2133, 1950.

Table 2.1 Primary Classification of Mathematical and Turbulence Models. (from Ref. 19)

Level	Method
1	Correlations
2	Integral Methods
3	One-point Closures
4	Two-point Closures
5	Large-Eddy Simulation
6	Full Simulation

Table 2.2 Classification of One-Point Closure Methods Based on the Treatment of Reynolds Stresses. (from Ref. 19)

Treatment of Reynolds Stresses
Boussinesq (eddy viscosity)
Algebraic
Differential
Reynolds-stress
Other

Table 2.3 Classification of Turbulence Models Using the Boussinesq Assumption. (from Ref. 19)

Equations		Label
μ_T prescribed		0
ODE for l_m		1/2
PDE for k	l_m prescribed	1
PDE for ω	l_m prescribed	1
PDE for k	ODE for l_m	1 1/2
PDE for k	PDE for ε	2
PDE for k	PDE for ω	2
PDE for k	PDE for l_m	2
PDE for $k^2 l_m$	PDE for ε	2

ODE: ordinary differential equation

PDE: partial differential equation

l_m : mixing length

k : turbulent kinetic energy

ω : specific dissipation rate

ε : turbulent dissipation rate

Table 2.4 Classification of Near Solid Wall Treatments. (from Ref. 19)

Treatment of Near Solid Wall	
No-slip velocity	with explicit damping
	without explicit damping
Law of the Wall	with explicit damping
	without explicit damping
Not applicable	
Other	

Table 2.5 Classification of Numerical Methods. (from Ref. 19)

Discretization	Solution technique
<u>Method employed</u> Finite difference - regular grid Staggered grid Finite Volume - regular grid Finite Element	<u>Strategy</u> Once through Iterative (not time like) Implicit - Backward Implicit - Crank-Nicolson Implicit - other
<u>Treatment of convective terms</u> Central differencing Upwind differencing Artificial diffusivity Hybrid (combination of any of the above) Quadratic upwind Skew upwind	<u>Dependent variables</u> Solved for simultaneously Solved for separately
<u>Conserved quantities</u> Mass, momentum and/or energy Non-conservative or mass only	<u>Pressure determined by</u> Poisson equation Corrective algorithm Equation of state
<u>Treatment of difficult boundary geometries</u> Asymmetric "stars" Boundary-fitted coordinates Coordinate transformations	<u>Iteration method</u> Point substitution Line substitution Matrix inversion ADI <u>Relaxation</u> Over-relaxation Under-relaxation

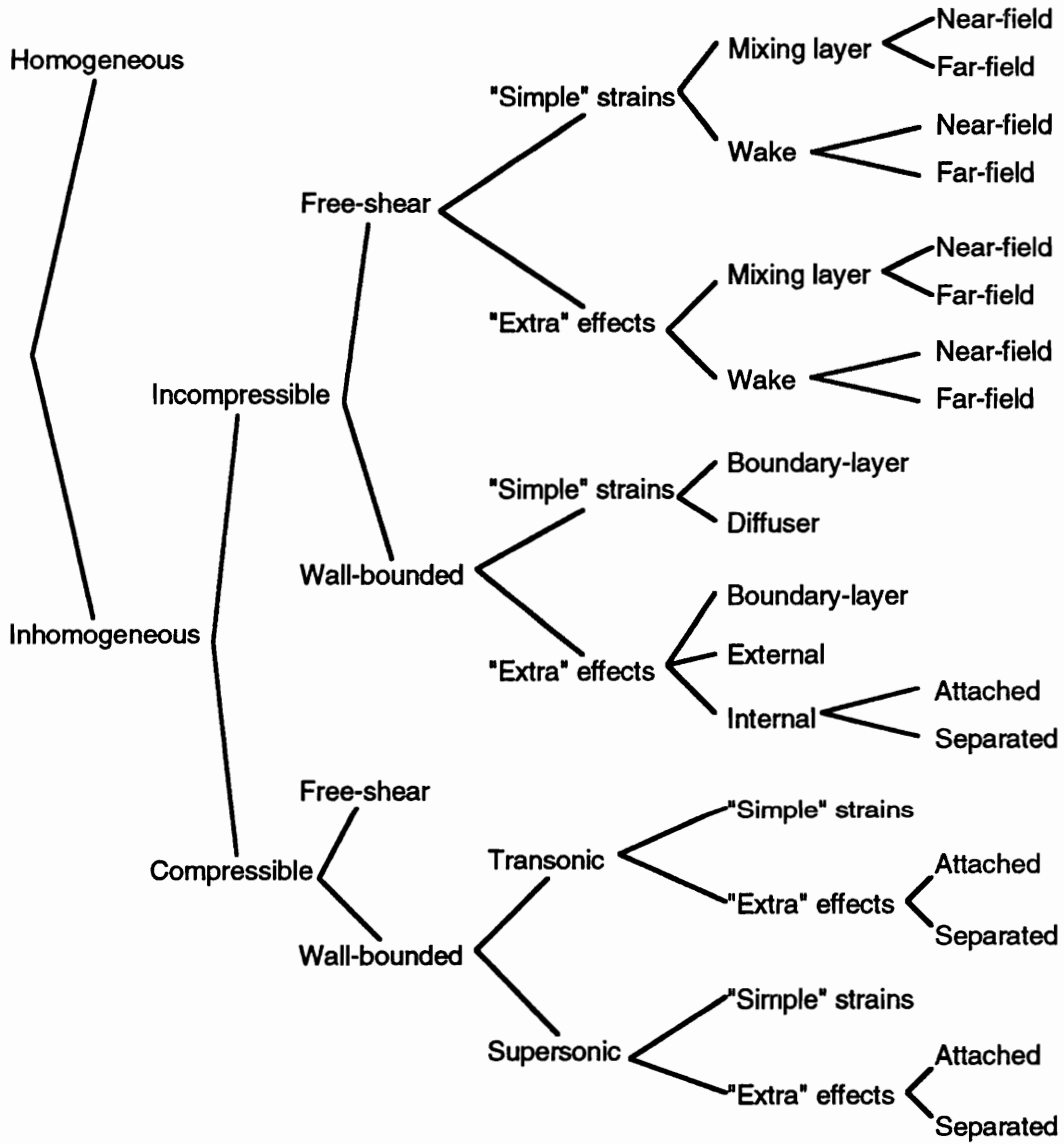


Figure 2.1 Morphology of Flows. (from Ref. 19)

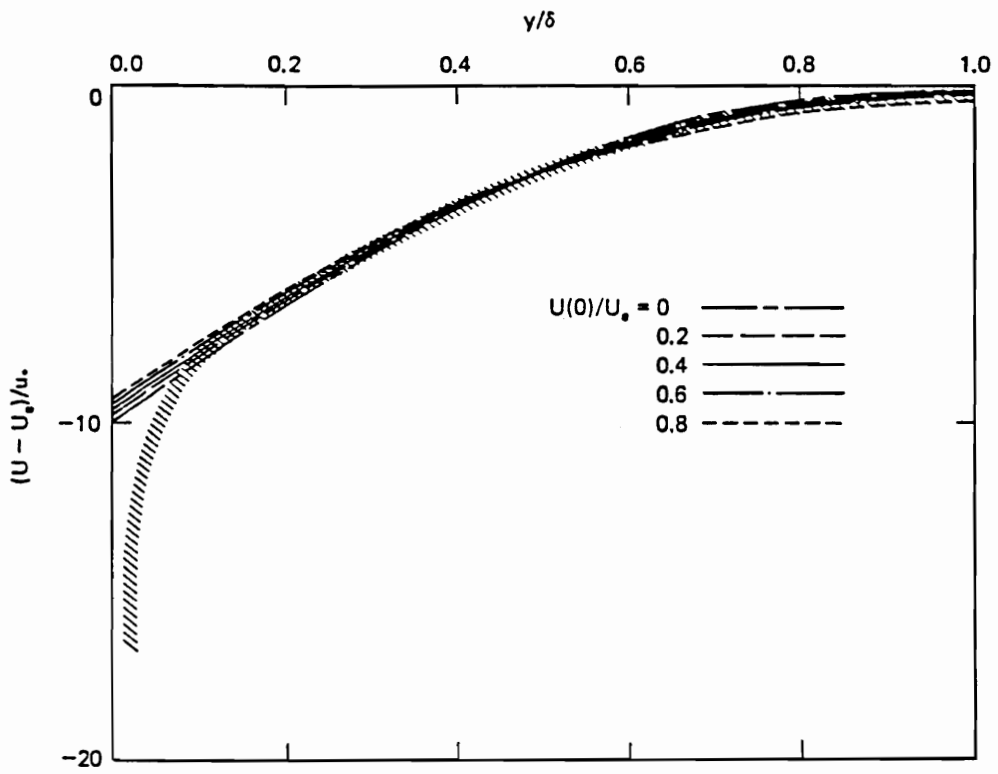


Figure 2.2 Clauser Pseudolaminar Velocity Profiles on Defect Law Plot. (from Ref. 9)

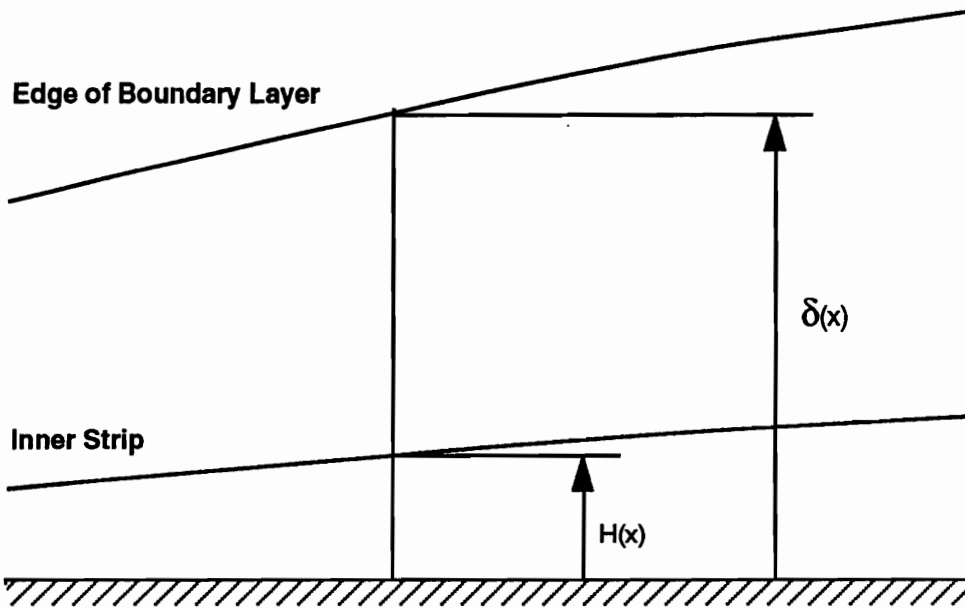


Figure 2.3 Schematic Diagram of Inner Strip In Boundary-Layer.

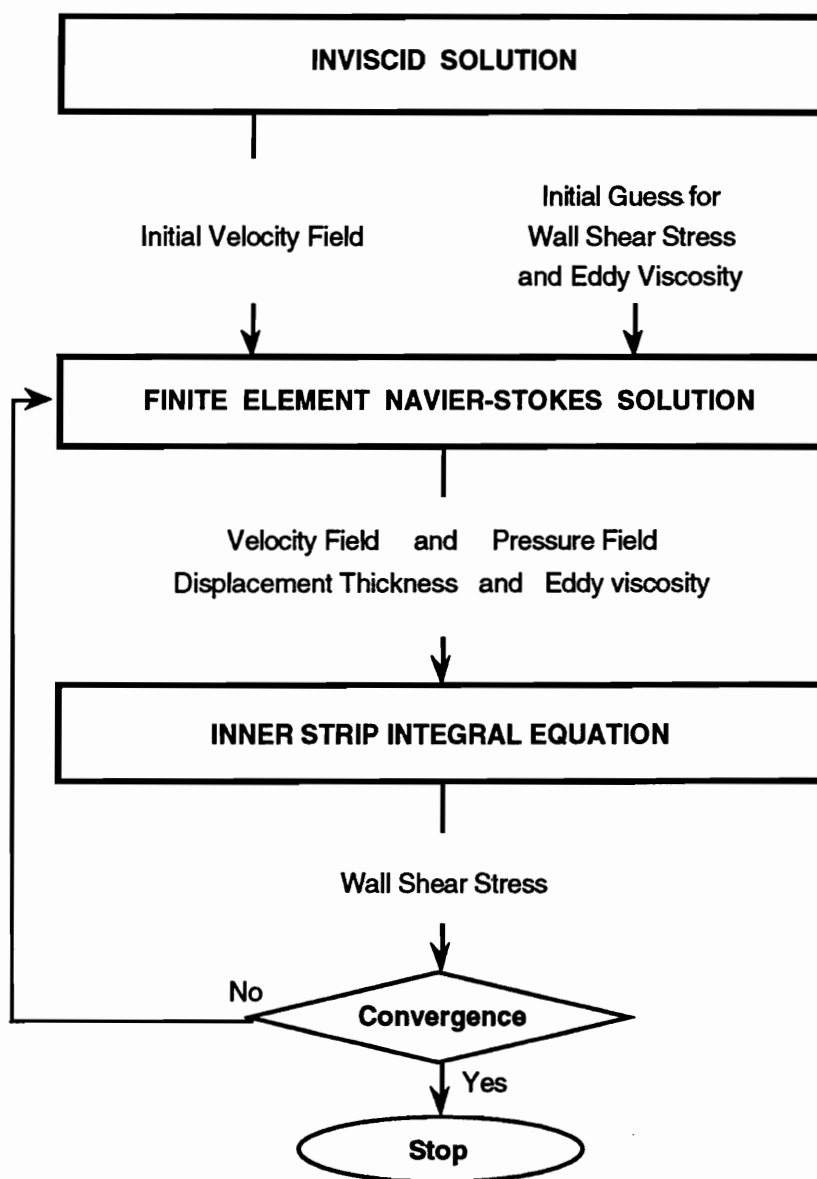


Figure 2.4 Flowchart of Computational Procedures for the Reynolds Averaged Navier-Stokes Equations.

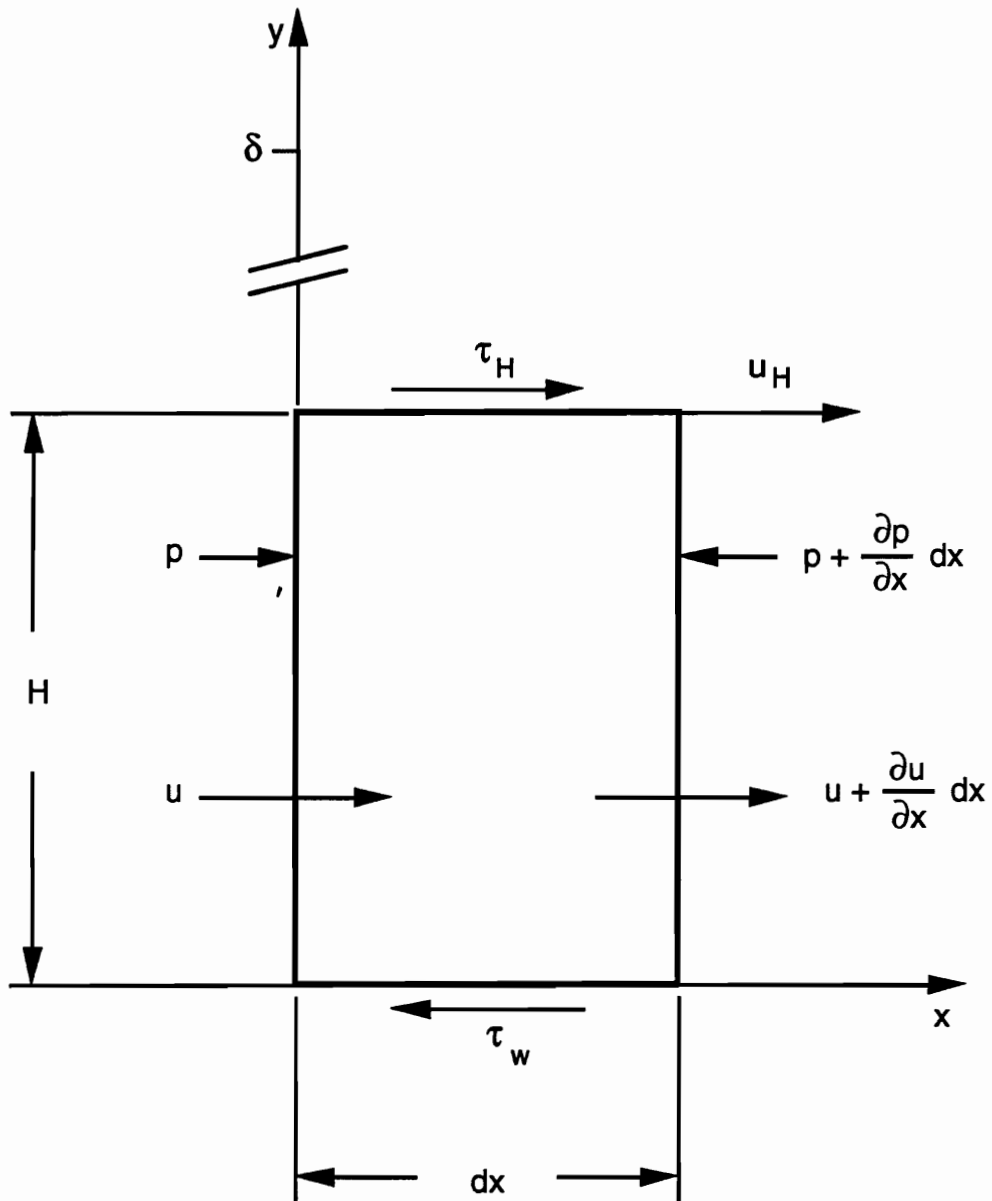


Figure 2.5 Two-Dimensional Control Volume of Finite Height (H) and Infinitesimal Base (dx).

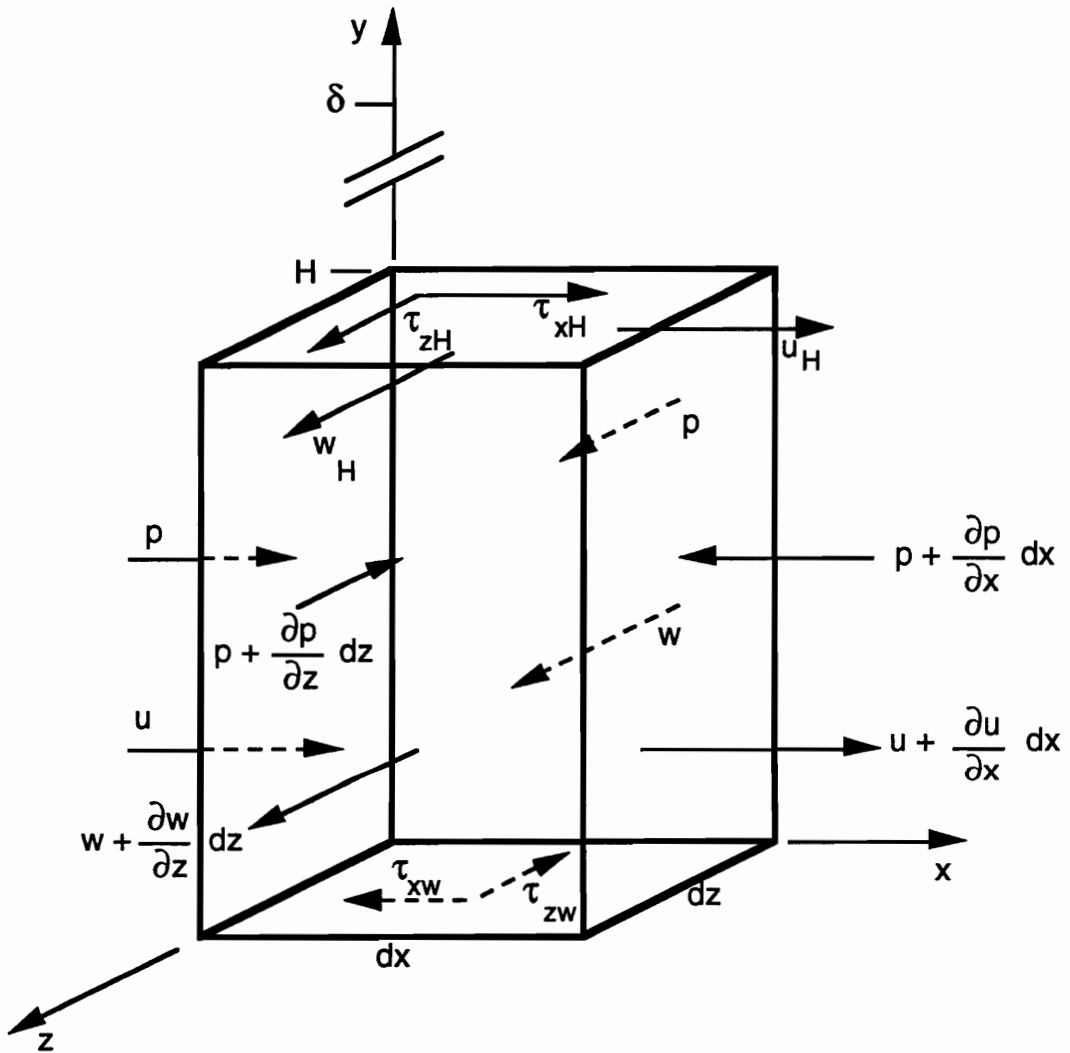


Figure 2.6 Three-Dimensional Control Volume of Finite Height (H) and Infinitesimal Base (dx by dz).

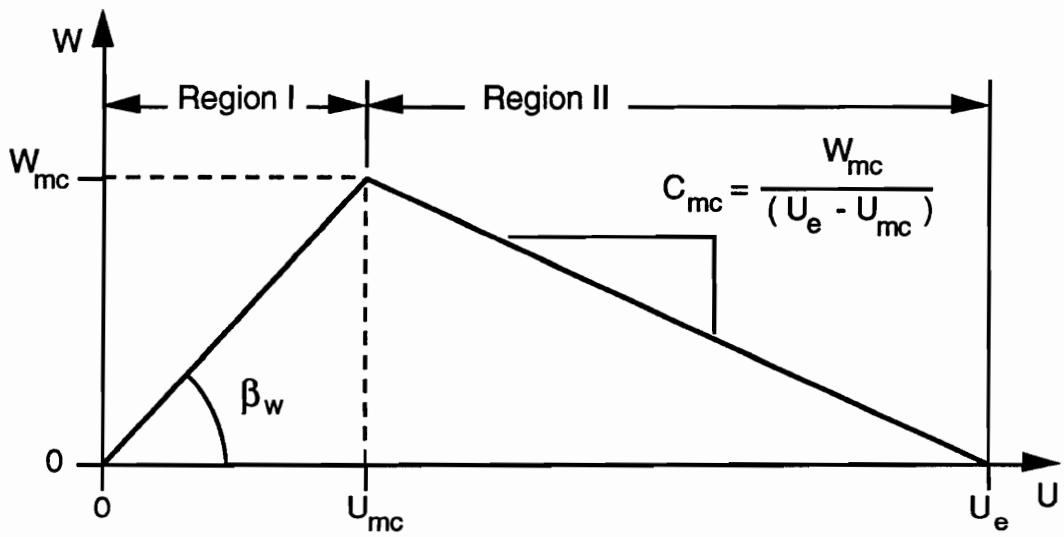


Figure 2.7 Johnston Triangular Model on Polar Plot.

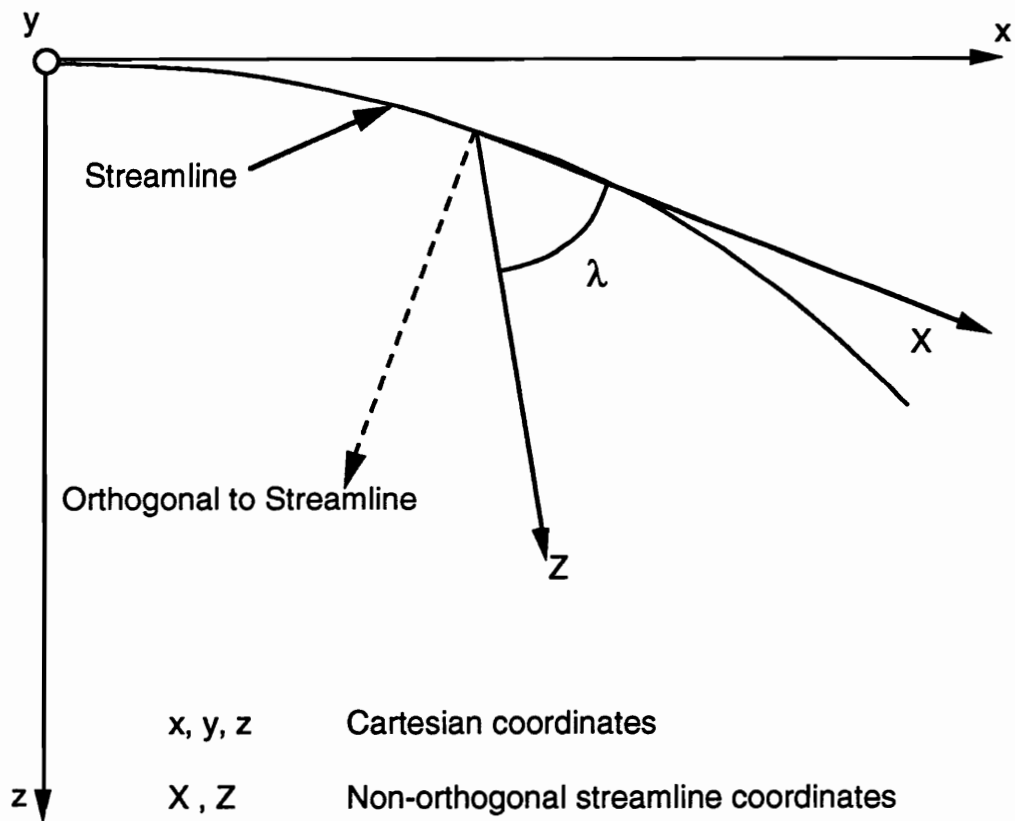


Figure 3.1 Schematic Diagram of Non-Orthogonal Coordinates System.

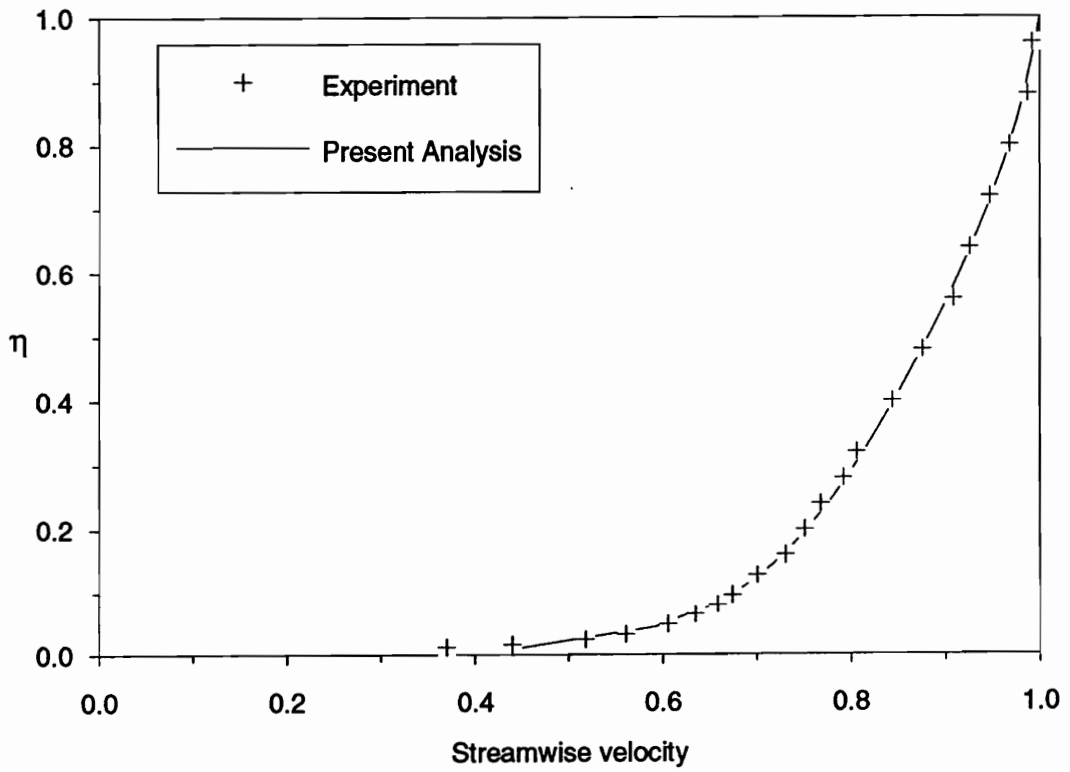


Figure 3.2 Comparison of Streamwise Velocity Profiles between the Present Analytical Model and Experimental Measurements for the Van den Berg-Elsenaar Flow at Station 1.

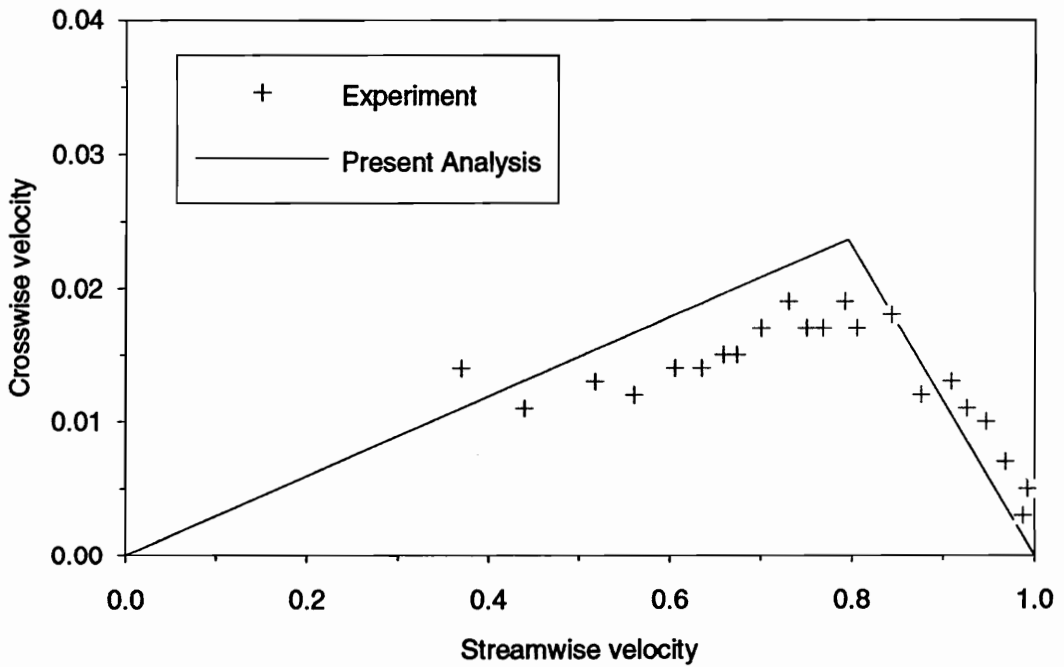


Figure 3.3 Comparison of Crosswise Velocity Profiles on Polar Plot between the Present Analytical Model and Experimental Measurements for the Van den Berg-Elsenaar Flow at Station 1.

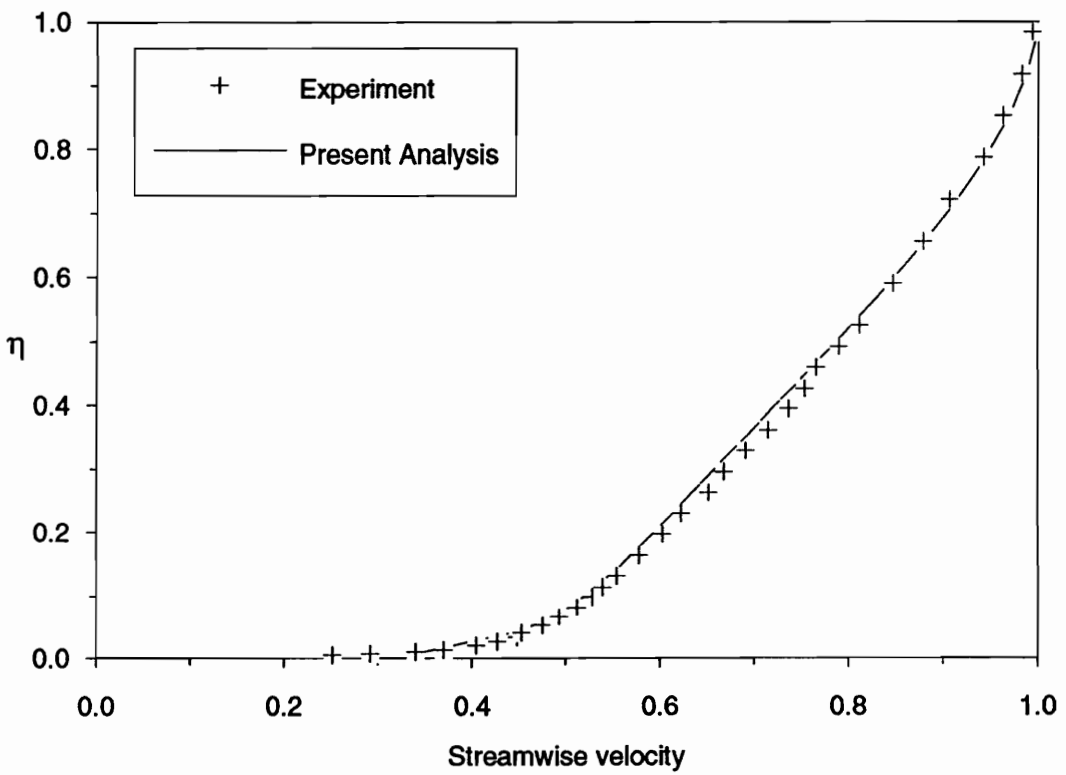


Figure 3.4 Comparison of Streamwise Velocity Profiles between the Present Analytical Model and Experimental Measurements for the Van den Berg-Elsenaar Flow at Station 6.

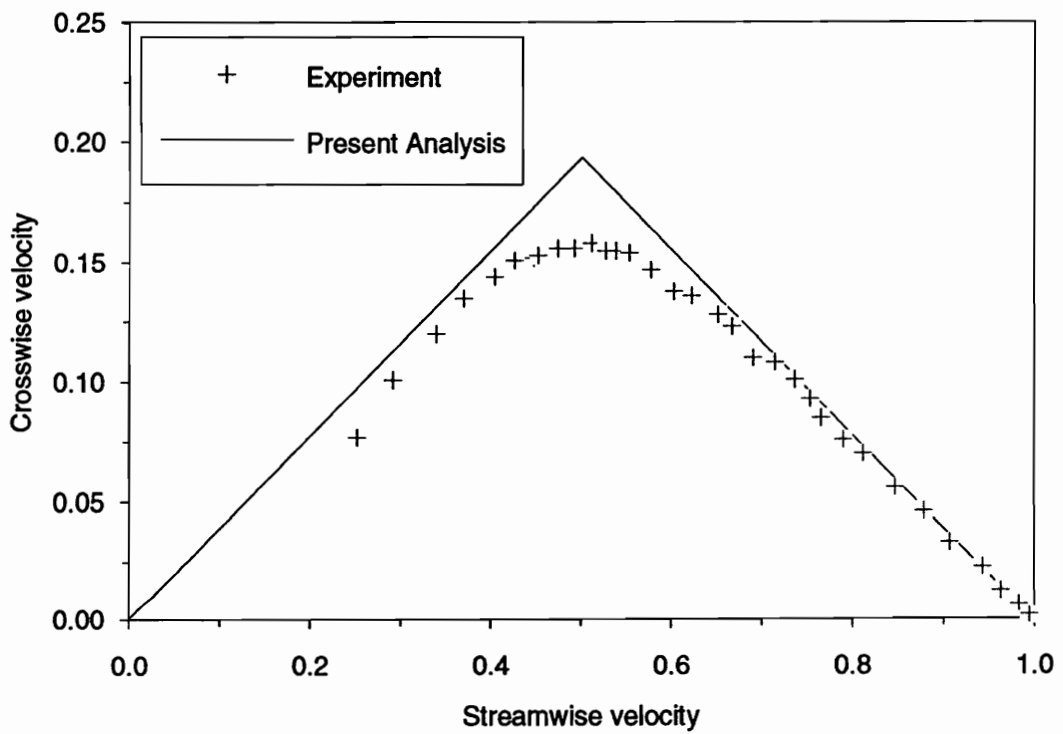


Figure 3.5 Comparison of Crosswise Velocity Profiles on Polar Plot between the Present Analytical Model and Experimental Measurements for the Van den Berg-Elsenaar Flow at Station 6.

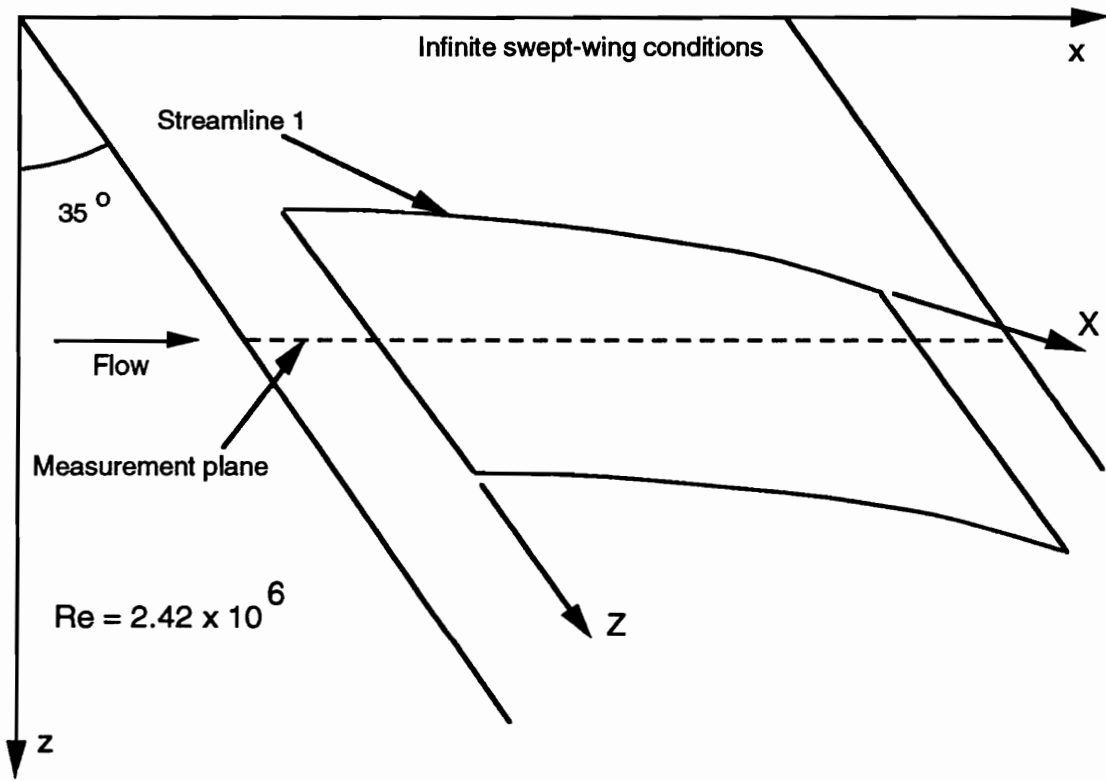


Figure 3.6 Van den Berg-Elsenaar - Computational Domain and Flow Conditions.

Van den Berg-Elsenaar Case

$Re = 2.42 \times 10^6$

$N_x = 71$

$\eta_H = 0.25$

$C_{zx} = 1.0$

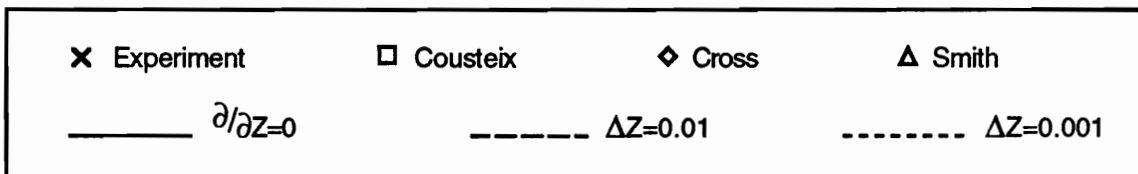
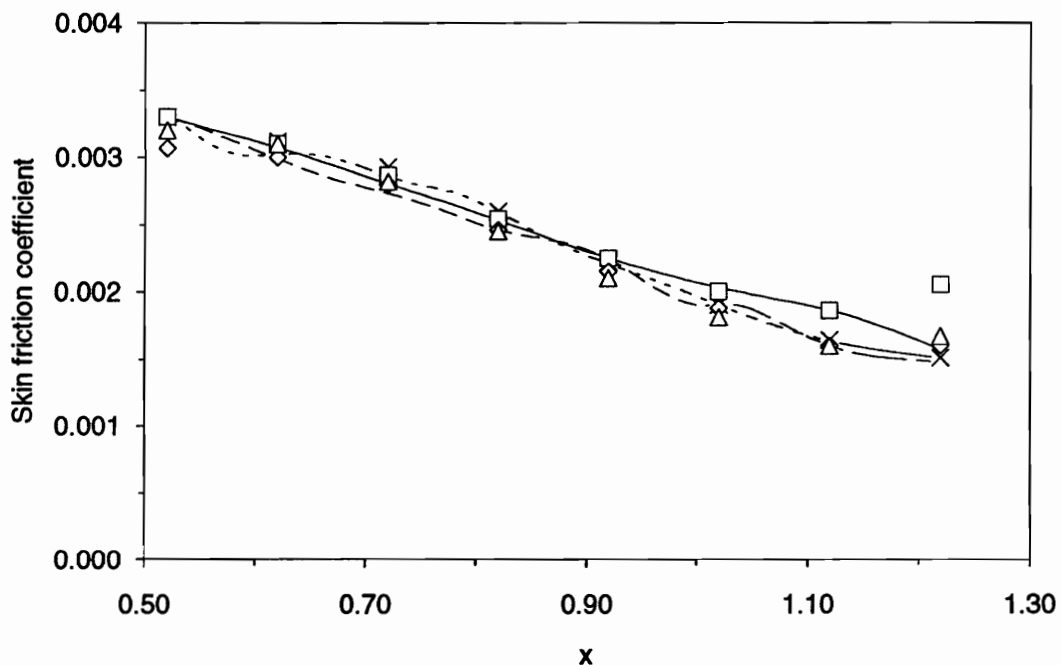
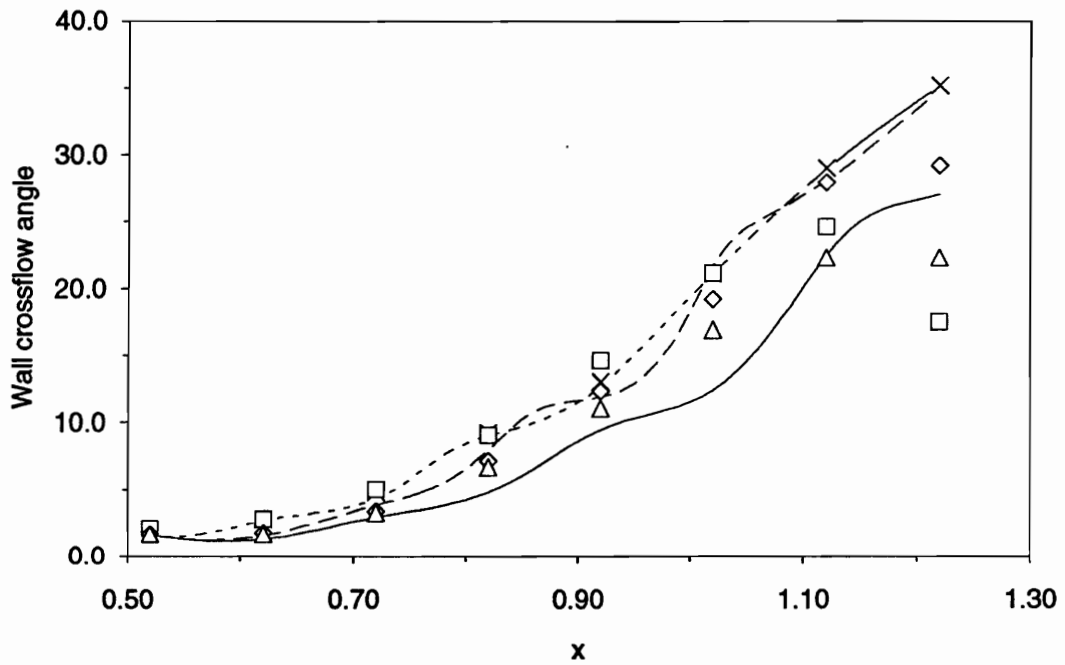


Figure 3.7 Van den Berg-Elsenaar - Skin Friction Coefficient along the Measurement Plane.

Van den Berg-Elsenaar Case

 $Re = 2.42 \times 10^6$
 $N_x = 71$
 $\eta_H = 0.25$
 $C_{zx} = 1.0$


× Experiment

□ Cousteix

◇ Cross

△ Smith

———— $\partial/\partial z=0$

----- $\Delta Z=0.01$

..... $\Delta Z=0.001$

Figure 3.8 Van den Berg-Elsenaar - Wall Crossflow Angle along the Measurement Plane.

Van den Berg-Elsenaar Case

$Re = 2.42 \times 10^6$

$N_x = 71$

$\eta_H = 0.25$

$C_{zx} = 1.0$

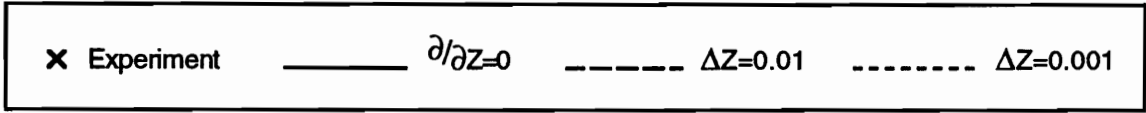
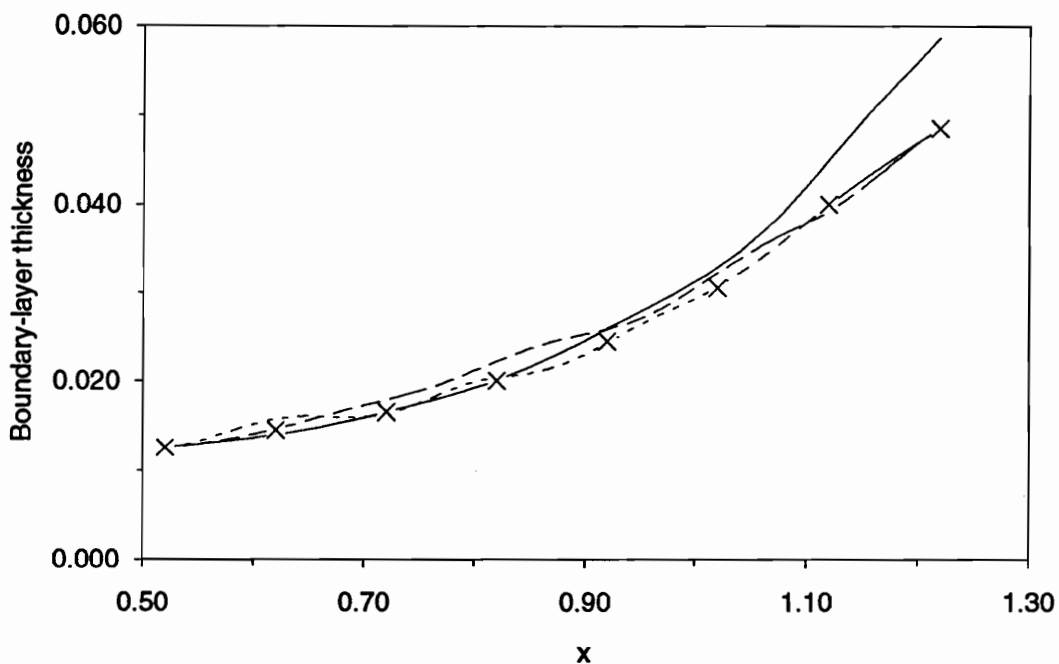


Figure 3.9 Van den Berg-Elsenaar - Boundary-Layer Thickness along the Measurement Plane.

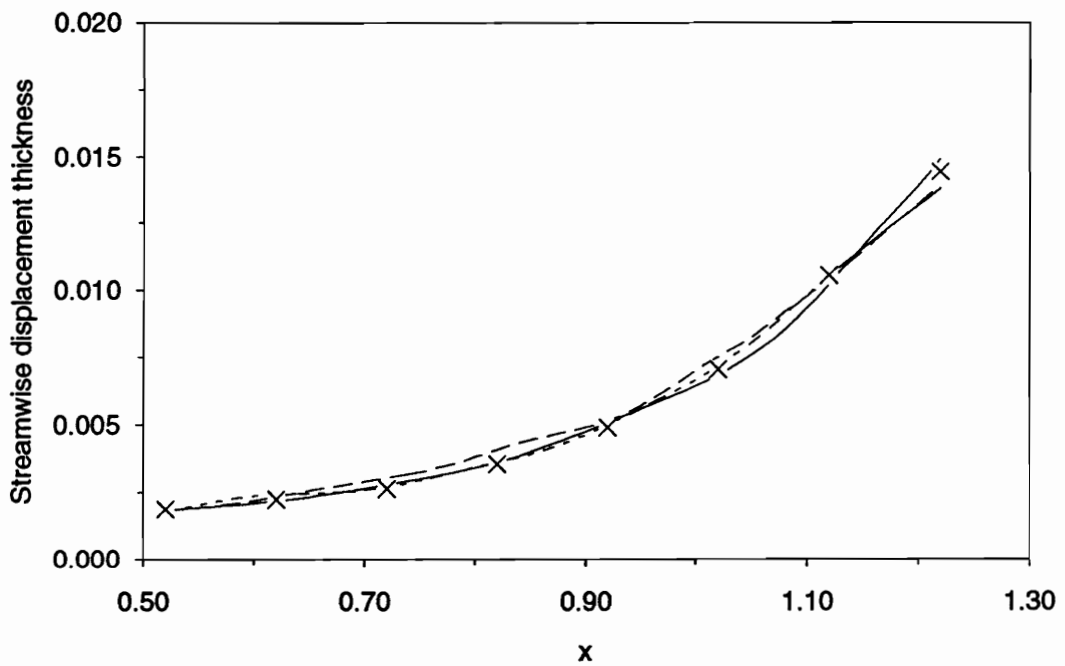
Van den Berg-Elsenaar Case

$Re = 2.42 \times 10^6$

$N_x = 71$

$\eta_H = 0.25$

$C_{zx} = 1.0$



x Experiment ——— $\partial/\partial z=0$ - - - - $\Delta Z=0.01$ ····· $\Delta Z=0.001$

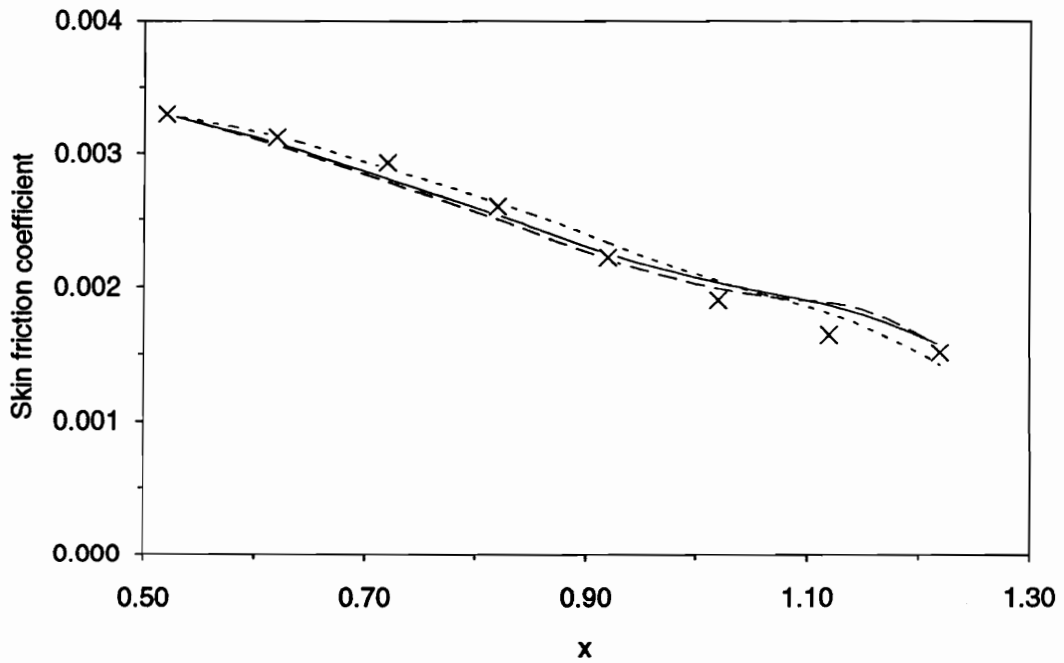
Figure 3.10 Van den Berg-Elsenaar - Streamwise Displacement Thickness along the Measurement Plane.

Van den Berg-Elsenaar Case

$$Re = 2.42 \times 10^6$$

$$N_x = 71$$

$$C_{zx} = 1.0$$



x Experiment $\eta_H=0.20$ ——— $\eta_H=0.25$ - - - $\eta_H=0.30$

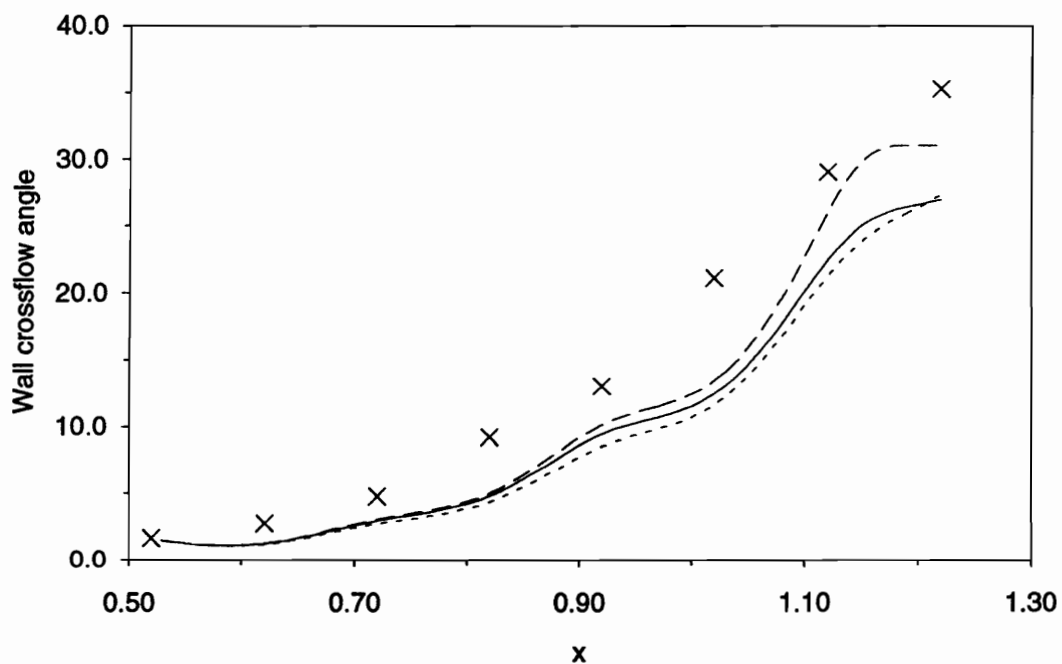
Figure 3.11 Van den Berg-Elsenaar - Influence of the Location of Inner Strip Upper Limit on the Results for the Skin Friction Coefficient along the Measurement Plane.

Van den Berg-Elsenaar Case

$Re = 2.42 \times 10^6$

$N_x = 71$

$C_{zx} = 1.0$



× Experiment $\eta_H=0.20$ ——— $\eta_H=0.25$ - - - - $\eta_H=0.30$

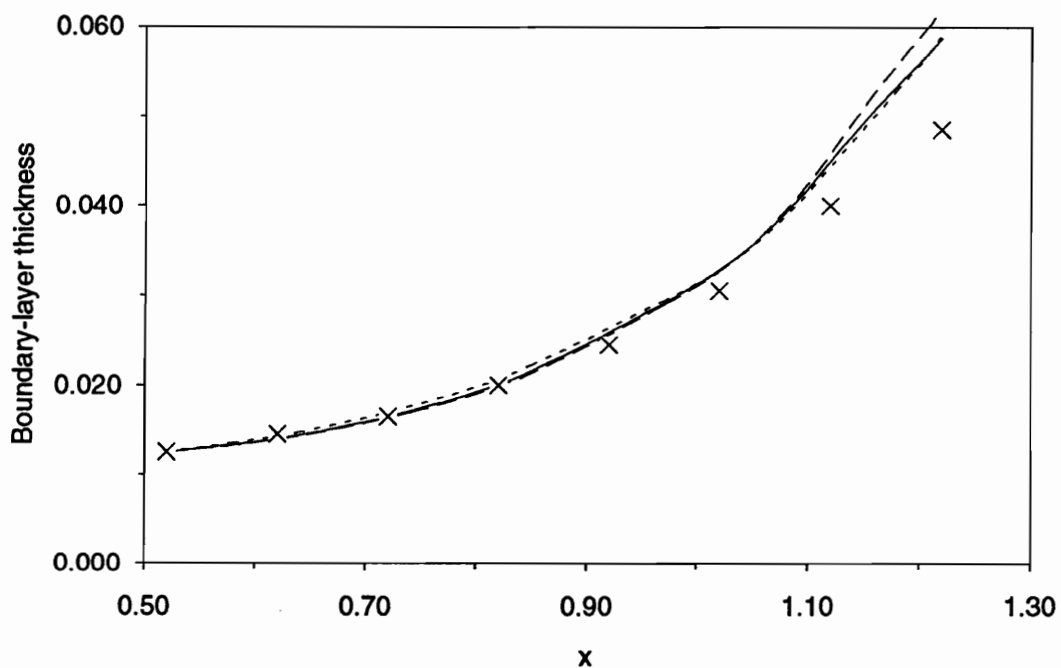
Figure 3.12 Van den Berg-Elsenaar - Influence of the Location of Inner Strip Upper Limit on the Results for the Wall Crossflow Angle along the Measurement Plane.

Van den Berg-Elsenaar Case

$$Re = 2.42 \times 10^6$$

$$N_x = 71$$

$$C_{zx} = 1.0$$



× Experiment $\eta_H=0.20$ ——— $\eta_H=0.25$ - - - $\eta_H=0.30$

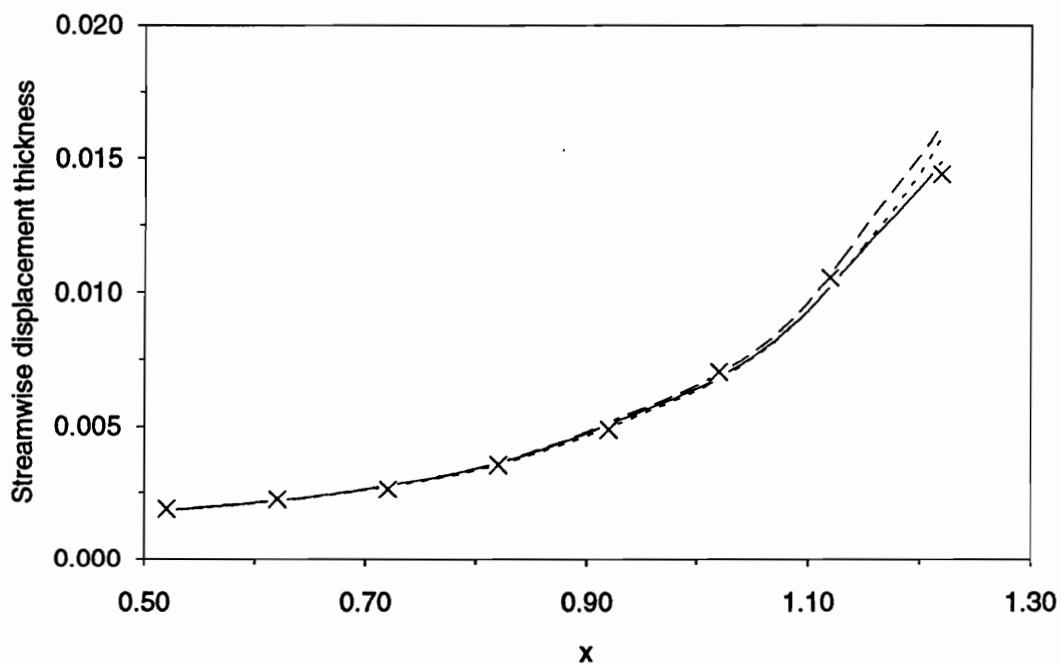
Figure 3.13 Van den Berg-Elsenaar - Influence of the Location of Inner Strip Upper Limit on the Results for the Boundary-Layer Thickness along the Measurement Plane.

Van den Berg-Elsenaar Case

$Re = 2.42 \times 10^6$

$N_x = 71$

$C_{zx} = 1.0$



× Experiment

----- $\eta_H=0.20$

————— $\eta_H=0.25$

- · - · - $\eta_H=0.30$

Figure 3.14 Van den Berg-Elsenaar - Influence of the Location of Inner Strip Upper Limit on the Results for the Streamwise Displacement Thickness along the Measurement Plane.

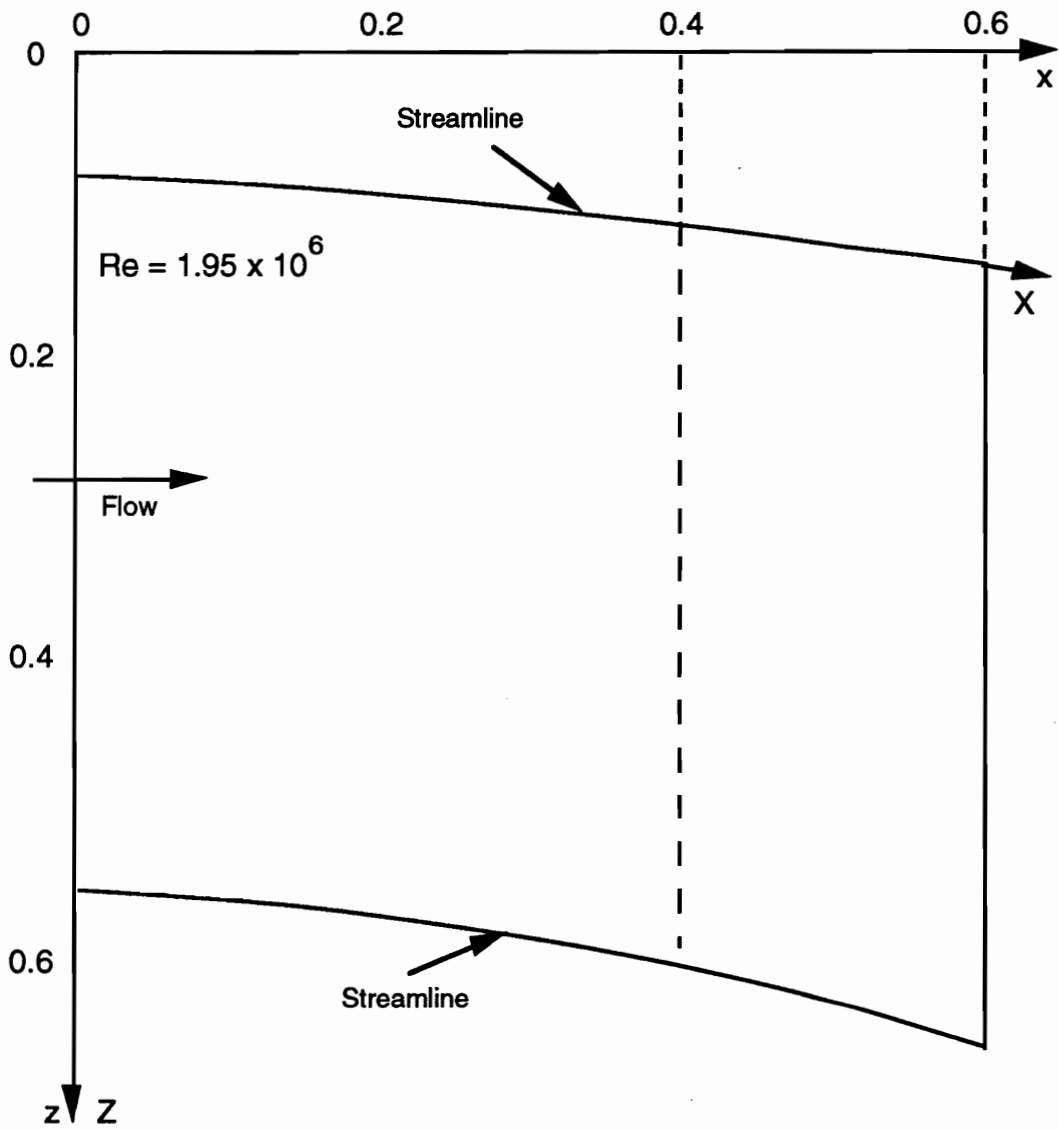


Figure 3.15 Müller-Krause - Computational Domain and Flow Conditions.

Müller-Krause Case - x=0.4

Re = 1.95×10^6

Mesh: 81 x 41

$\eta_H = 0.35$

$C_{zx} = 1.2$

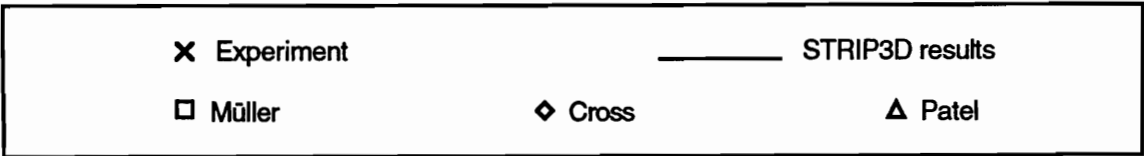
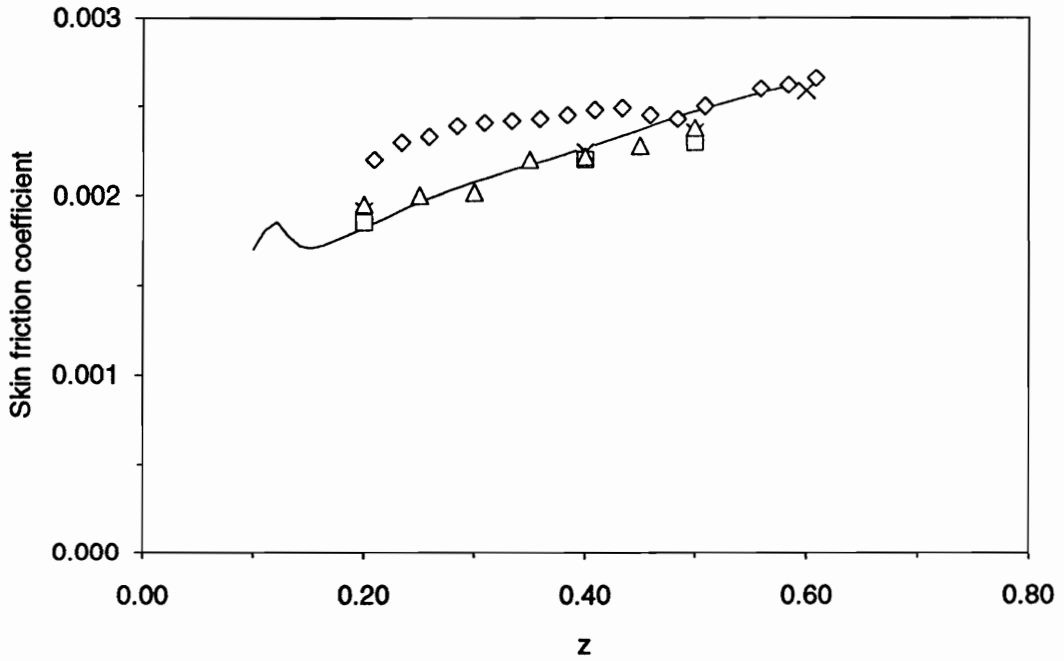


Figure 3.16 Müller-Krause - Skin Friction Coefficient along z-axis at x=0.4.

Müller-Krause Case - $x=0.4$

$Re = 1.95 \times 10^6$

Mesh: 81 x 41

$\eta_H = 0.35$

$C_{zx} = 1.2$

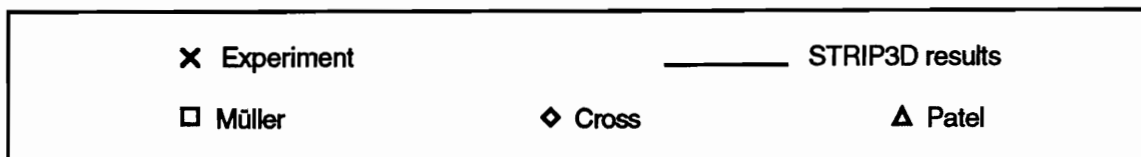
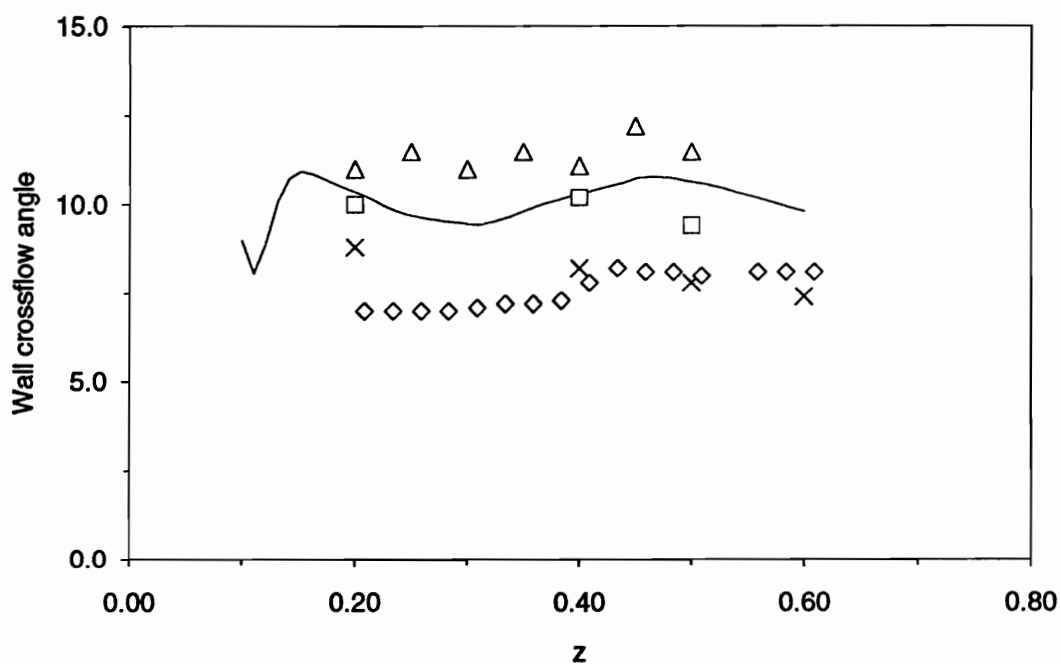


Figure 3.17 Müller-Krause - Wall Crossflow Angle along z-axis at $x=0.4$.

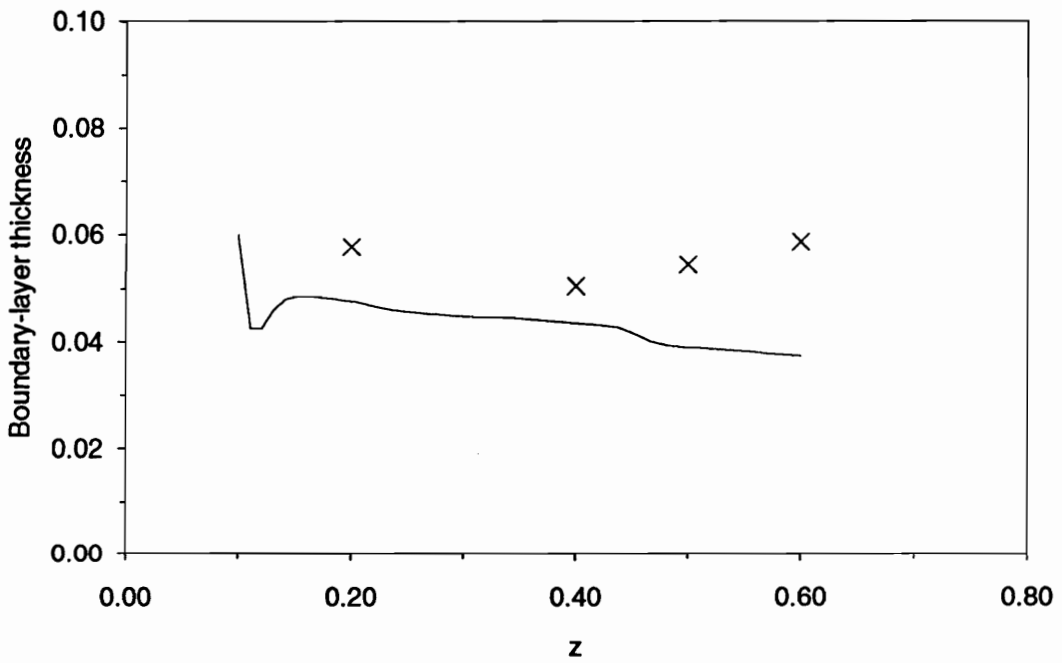
Müller-Krause Case - $x=0.4$

$Re = 1.95 \times 10^6$

Mesh: 81 x 41

$\eta_H = 0.35$

$C_{zx} = 1.2$



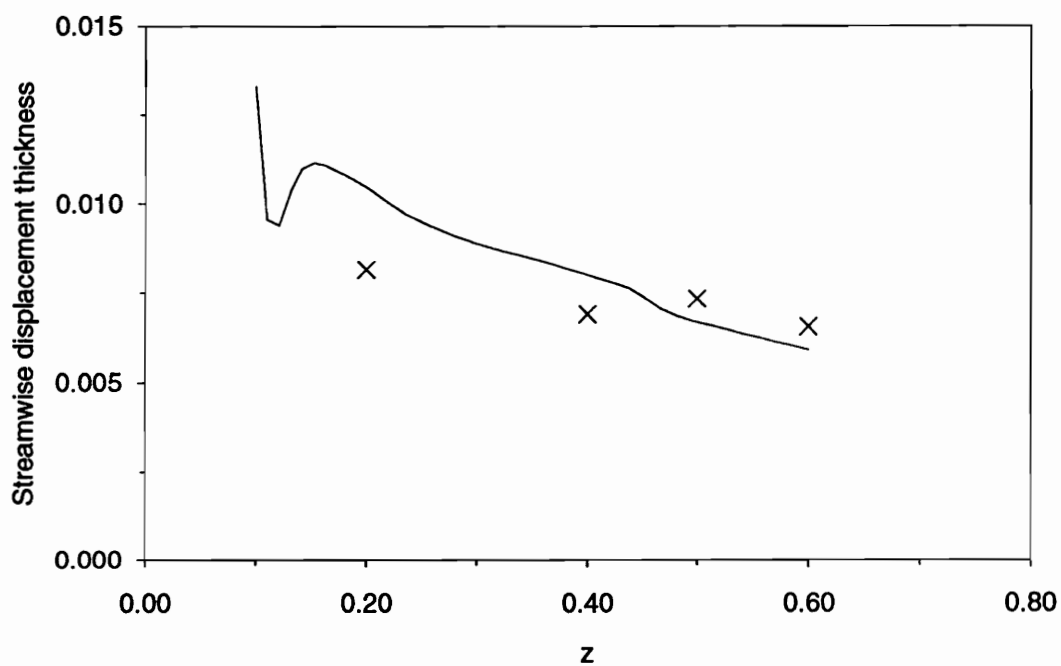
× Experiment

— STRIP3D results

Figure 3.18 Müller-Krause - Boundary-Layer Thickness along z-axis at $x=0.4$.

Müller-Krause Case - $x=0.4$ $Re = 1.95 \times 10^6$

Mesh: 81 x 41

 $\eta_H = 0.35$ $C_{zx} = 1.2$ **x** Experiment

—— STRIP3D results

Figure 3.19 Müller-Krause - Streamwise Displacement Thickness along z-axis at $x=0.4$.

Müller-Krause Case - $x=0.6$

$Re = 1.95 \times 10^6$

Mesh: 81 x 41

$\eta_H = 0.35$

$C_{zx} = 1.2$

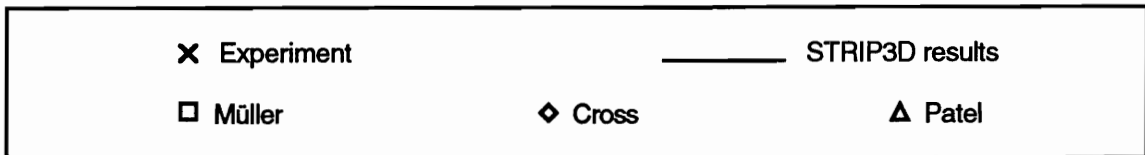
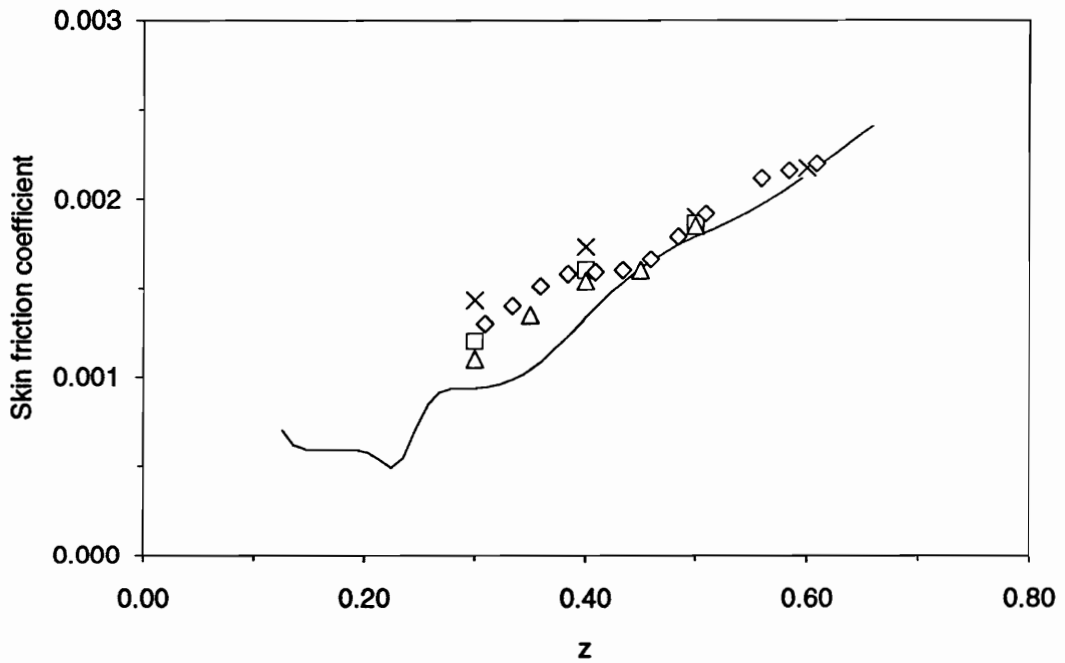


Figure 3.20 Müller-Krause - Skin Friction Coefficient along z-axis at $x=0.6$.

Müller-Krause Case - $x=0.6$

$Re = 1.95 \times 10^6$

Mesh: 81 x 41

$\eta_H = 0.35$

$C_{zx} = 1.2$

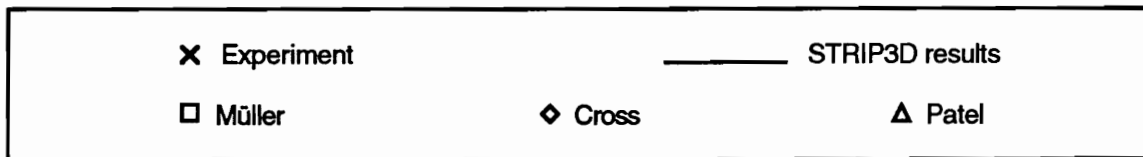
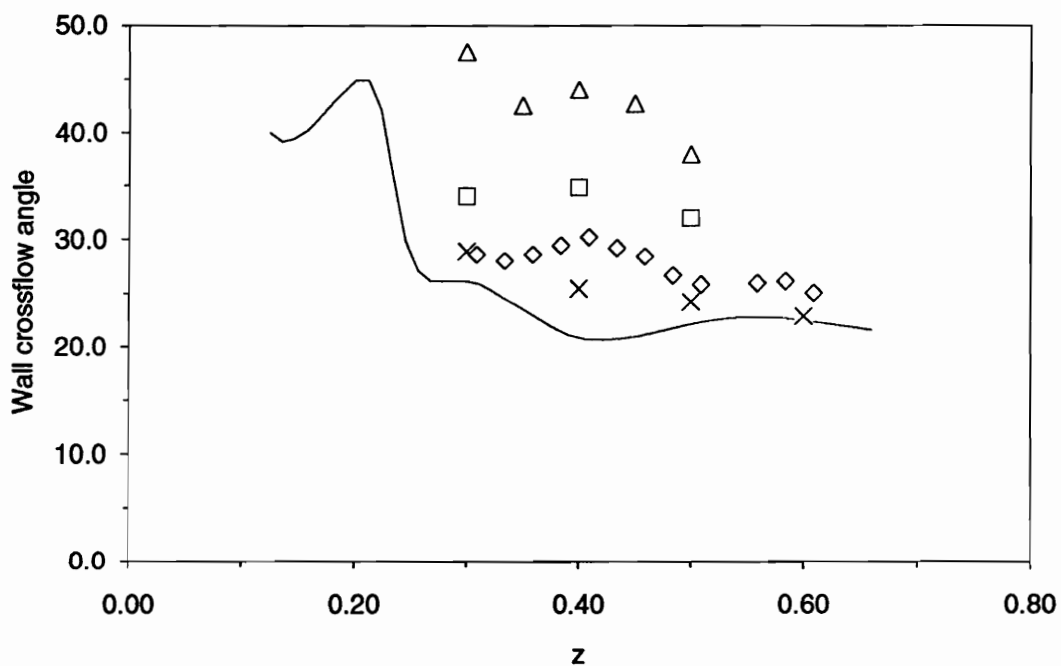


Figure 3.21 Müller-Krause - Wall Crossflow Angle along z-axis at $x=0.6$.

Müller-Krause Case - x=0.6

Re = 1.95×10^6

Mesh: 81 x 41

$\eta_H = 0.35$

$C_{zx} = 1.2$

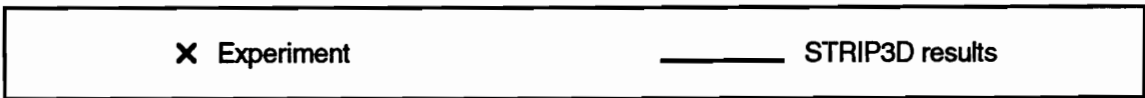
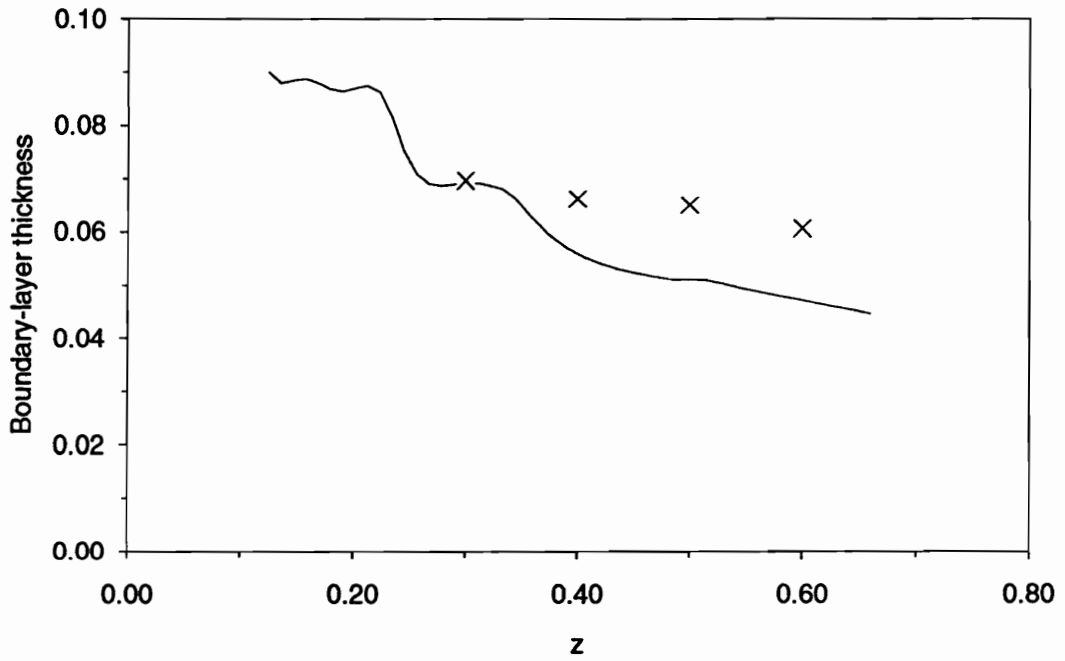


Figure 3.22 Müller-Krause - Boundary-Layer Thickness along z-axis at x=0.6.

Müller-Krause Case - x=0.6

Re = 1.95×10^6

Mesh: 81 x 41

$\eta_H = 0.35$

$C_{zx} = 1.2$

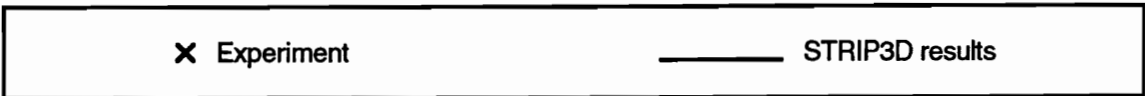
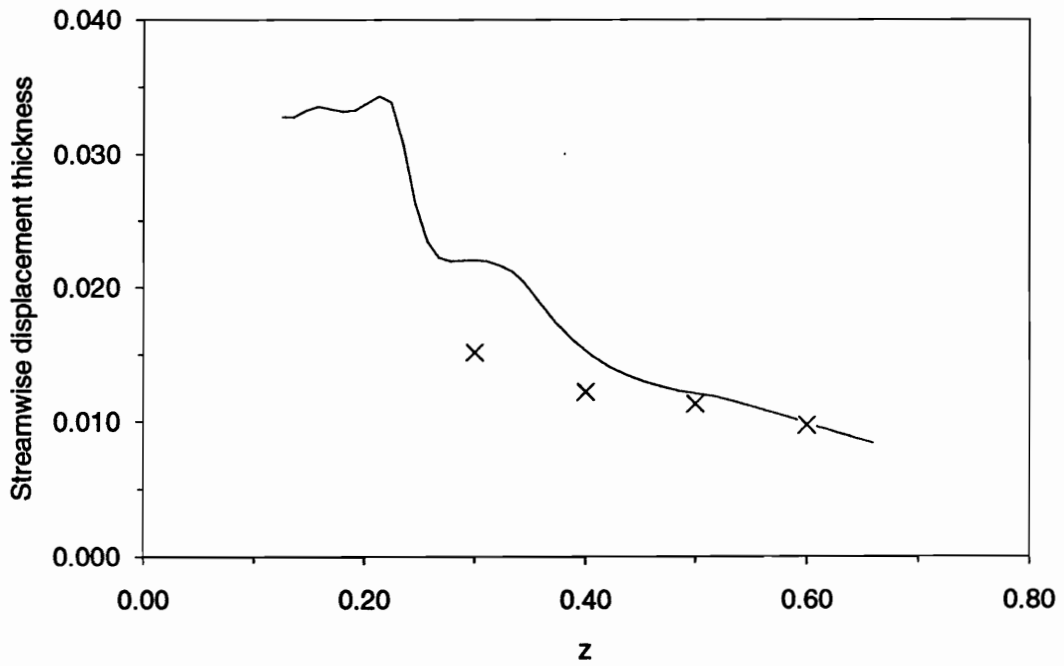


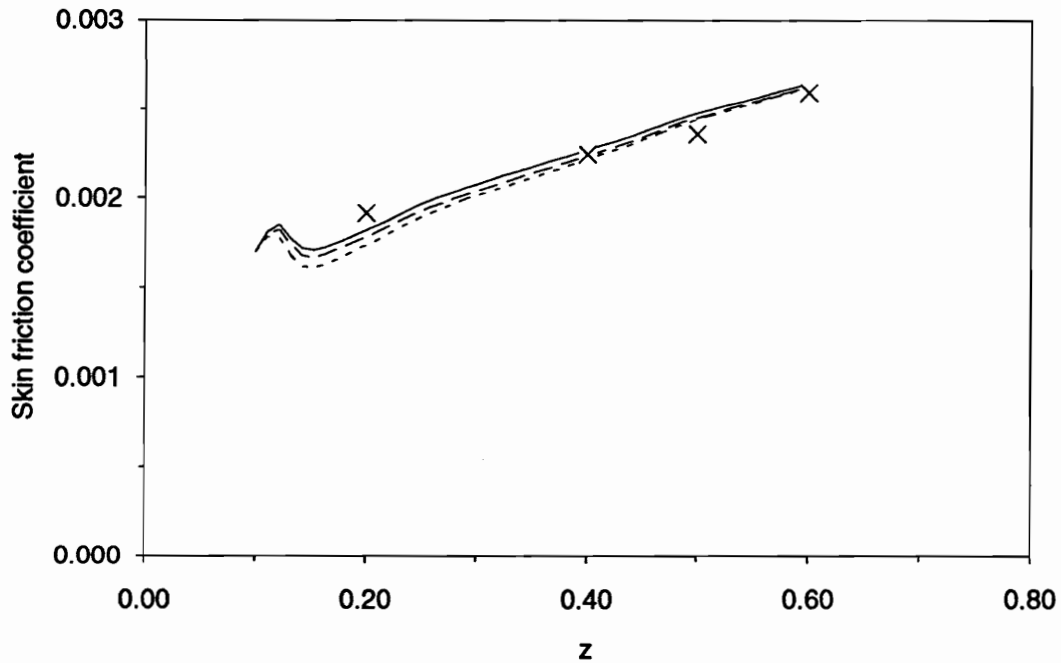
Figure 3.23 Müller-Krause - Streamwise Displacement Thickness along z-axis at x=0.6.

Müller-Krause Case - $x=0.4$

$Re = 1.95 \times 10^6$

Mesh: 81 x 41

$C_{zx} = 1.2$



$\eta_H=0.25$
 $\eta_H=0.30$
 $\eta_H=0.35$

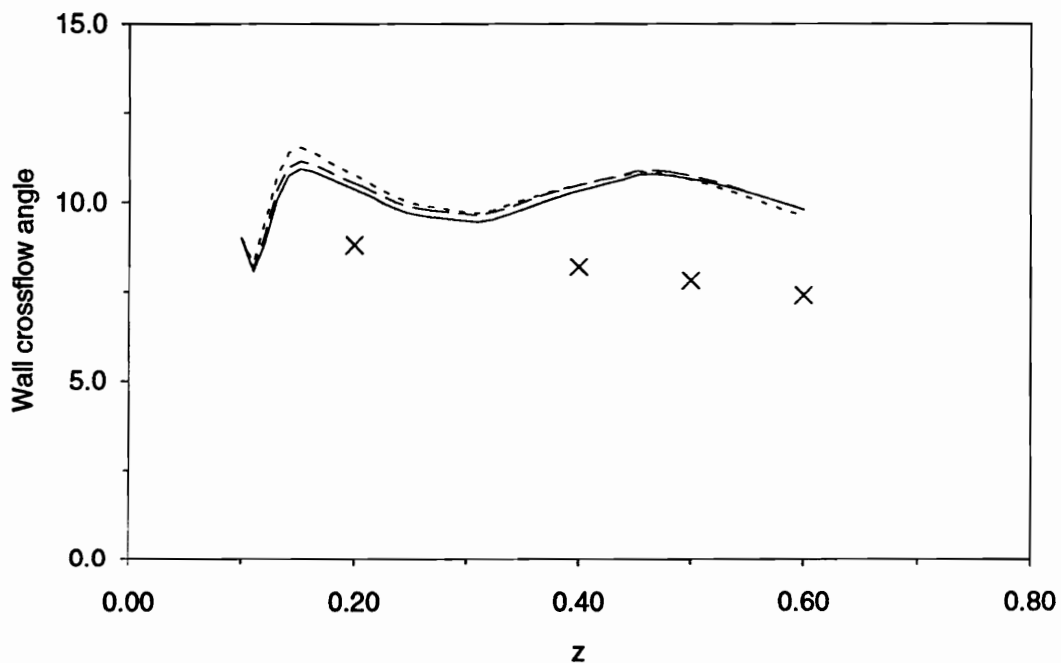
Figure 3.24 Müller-Krause - Influence of the Location of Inner Strip Upper Limit on the Results for the Skin Friction Coefficient along z-axis at $x=0.4$.

Müller-Krause Case - $x=0.4$

$Re = 1.95 \times 10^6$

Mesh: 81 x 41

$C_{zx} = 1.2$



x Experiment
 $\eta_H=0.25$
 - - - - $\eta_H=0.30$
 _____ $\eta_H=0.35$

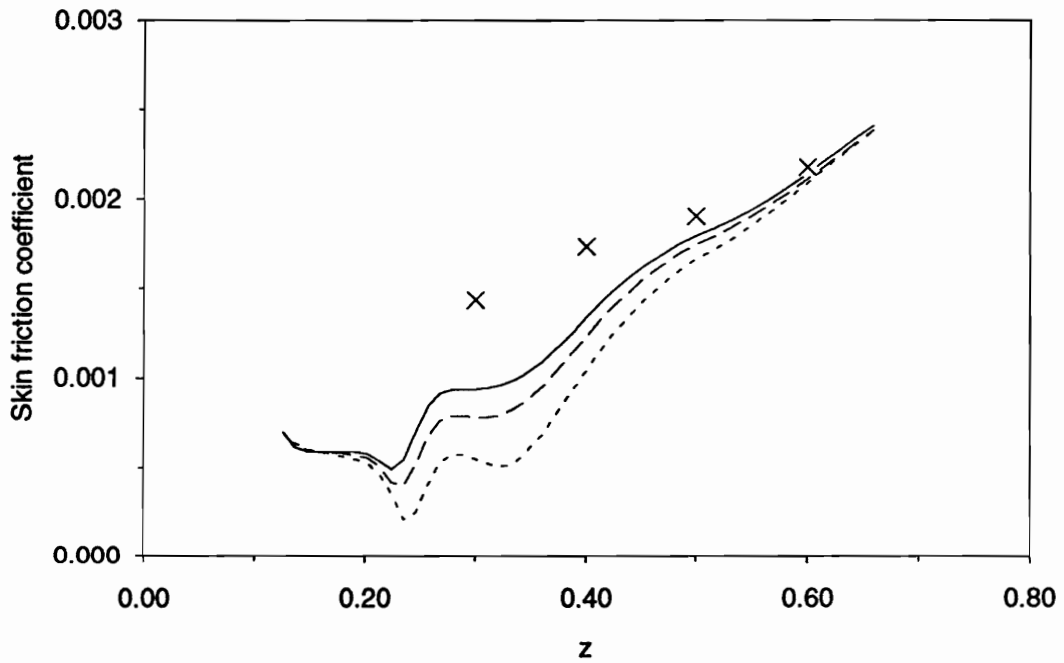
Figure 3.25 Müller-Krause - Influence of the Location of Inner Strip Upper Limit on the Results for the Wall Crossflow Angle along z-axis at $x=0.4$.

Müller-Krause Case - $x=0.6$

$Re = 1.95 \times 10^6$

Mesh: 81 x 41

$C_{zx} = 1.2$



X Experiment $\eta_H=0.25$ - - - - $\eta_H=0.30$ _____ $\eta_H=0.35$

Figure 3.26 Müller-Krause - Influence of the Location of Inner Strip Upper Limit on the Results for the Skin Friction Coefficient along z-axis at $x=0.6$.

Müller-Krause Case - x=0.6

Re = 1.95×10^6

Mesh: 81 x 41

$C_{Zx} = 1.2$

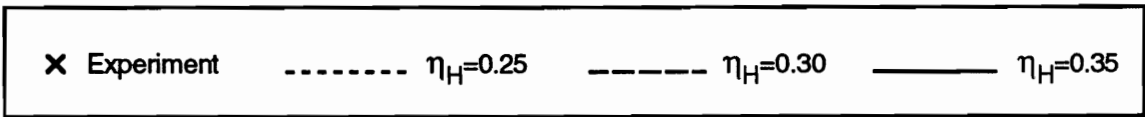
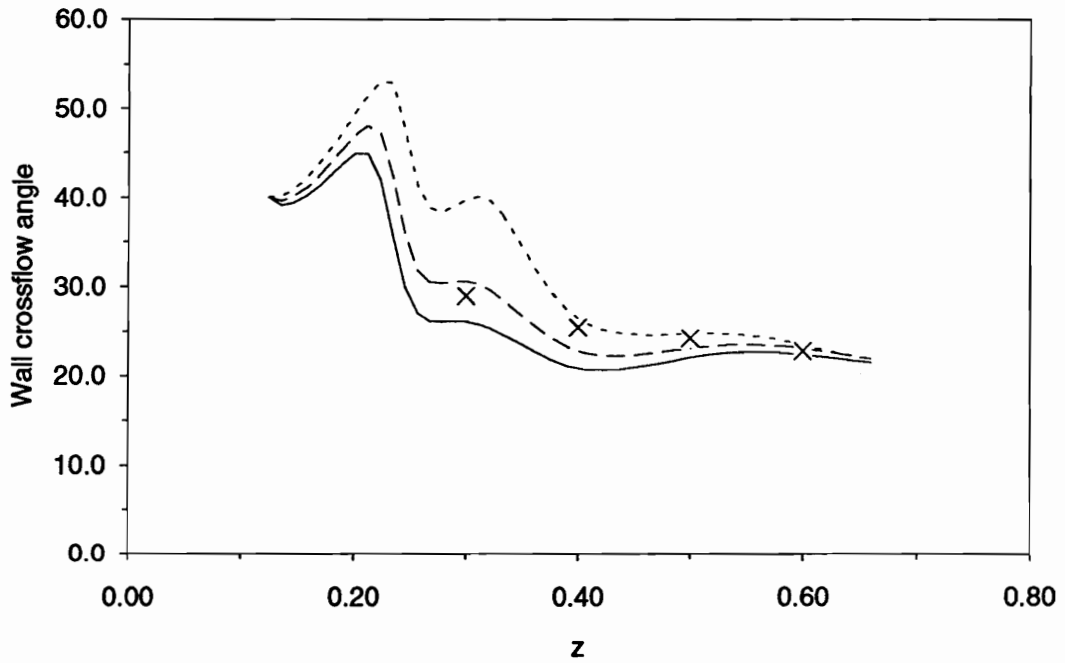


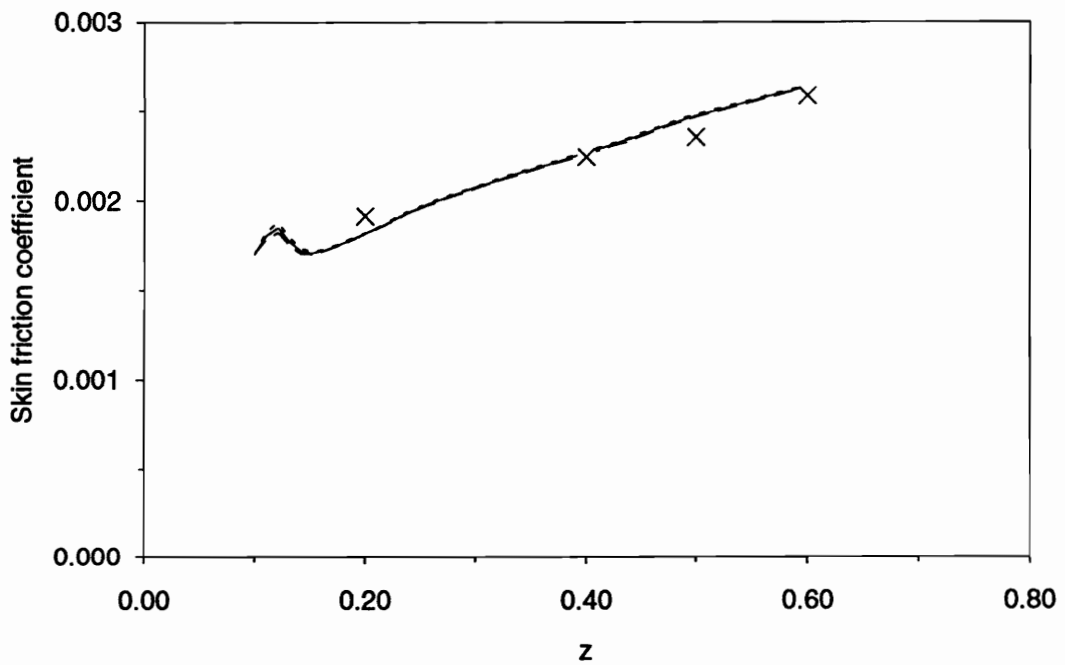
Figure 3.27 Müller-Krause - Influence of the Location of Inner Strip Upper Limit on the Results for the Wall Crossflow Angle along z-axis at x=0.6.

Müller-Krause Case - $x=0.4$

$Re = 1.95 \times 10^6$

Mesh: 81×41

$\eta_H = 0.35$



× Experiment $C_{zx}=1.0$ ——— $C_{zx}=1.2$ - - - - $C_{zx}=1.4$

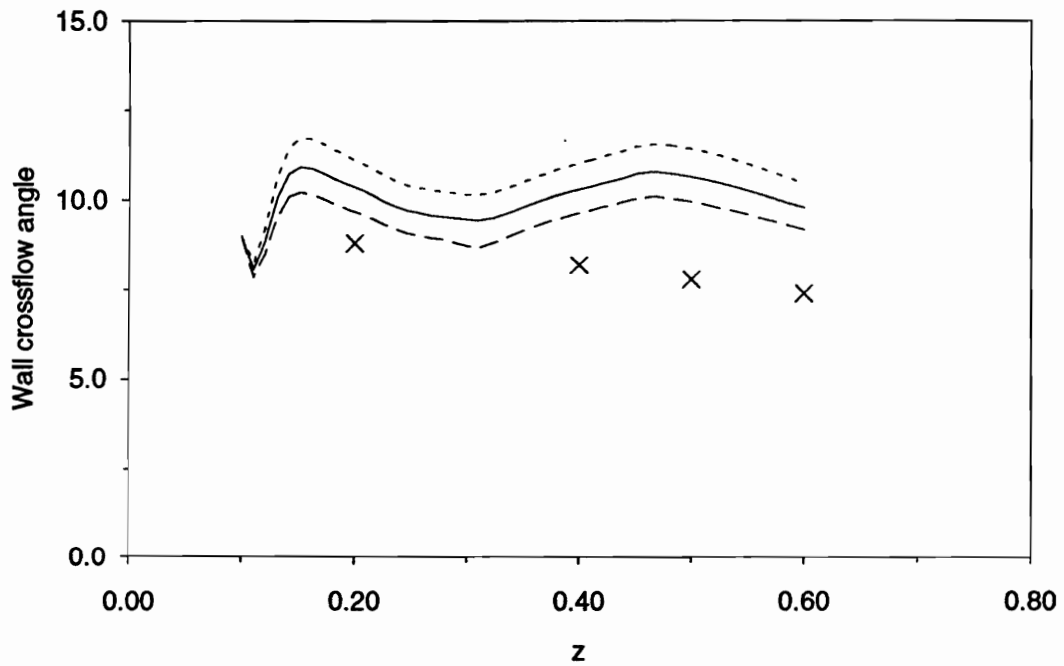
Figure 3.28 Müller-Krause - Influence of the Eddy Viscosity Ratio on the Results for the Skin Friction Coefficient along z-axis at $x=0.4$.

Müller-Krause Case - $x=0.4$

$Re = 1.95 \times 10^6$

Mesh: 81 x 41

$\eta_H = 0.35$



× Experiment - - - - - $C_{zx}=1.0$ ——— $C_{zx}=1.2$ - · - · - $C_{zx}=1.4$

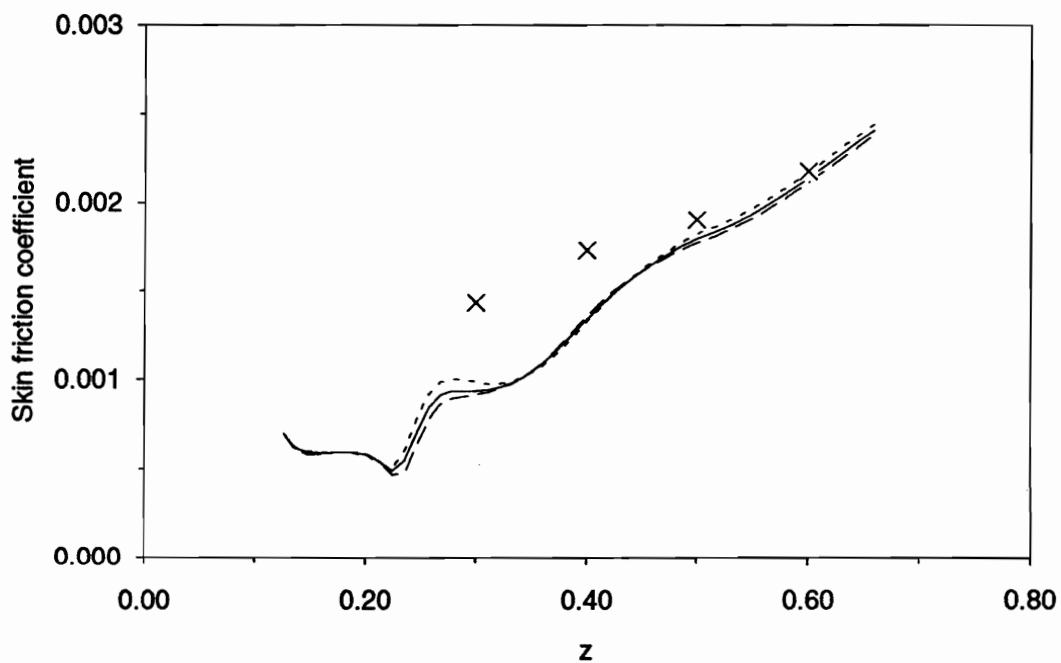
Figure 3.29 Müller-Krause - Influence of the Eddy Viscosity Ratio on the Results for the Wall Crossflow Angle along z-axis at $x=0.4$.

Müller-Krause Case - $x=0.6$

$Re = 1.95 \times 10^6$

Mesh: 81 x 41

$\eta_H = 0.35$



x Experiment
 $C_{zx}=1.0$
 _____ $C_{zx}=1.2$
 - - - - - $C_{zx}=1.4$

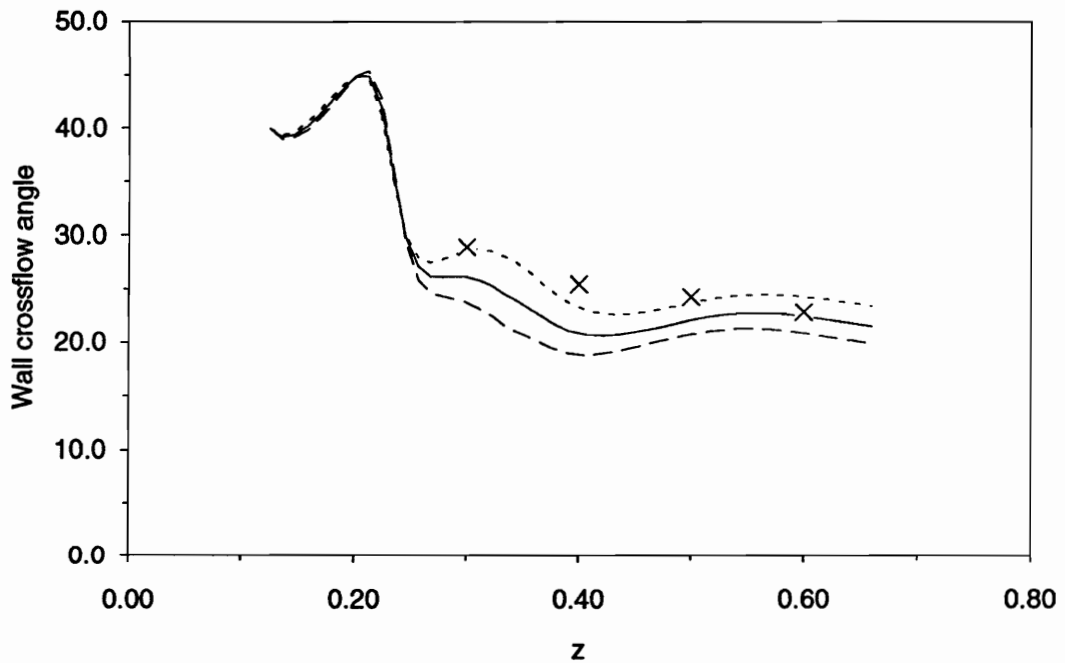
Figure 3.30 Müller-Krause - Influence of the Eddy Viscosity Ratio on the Results for the Skin Friction Coefficient along z-axis at $x=0.6$.

Müller-Krause Case - $x=0.6$

$Re = 1.95 \times 10^6$

Mesh: 81 x 41

$\eta_H = 0.35$



x Experiment
 $C_{zx}=1.0$
 _____ $C_{zx}=1.2$
 ----- $C_{zx}=1.4$

Figure 3.31 Müller-Krause - Influence of the Eddy Viscosity Ratio on the Results for the Wall Crossflow Angle along z-axis at $x=0.6$.

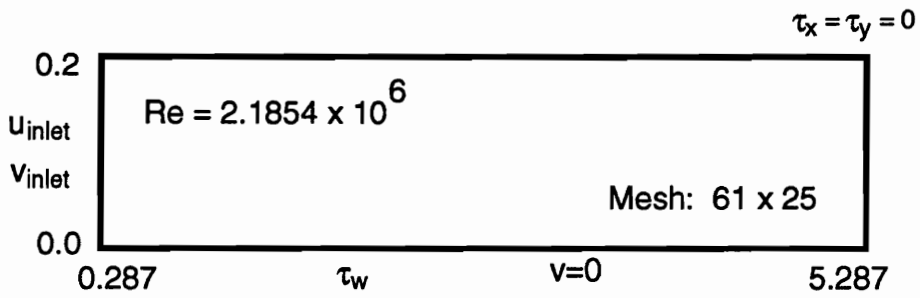


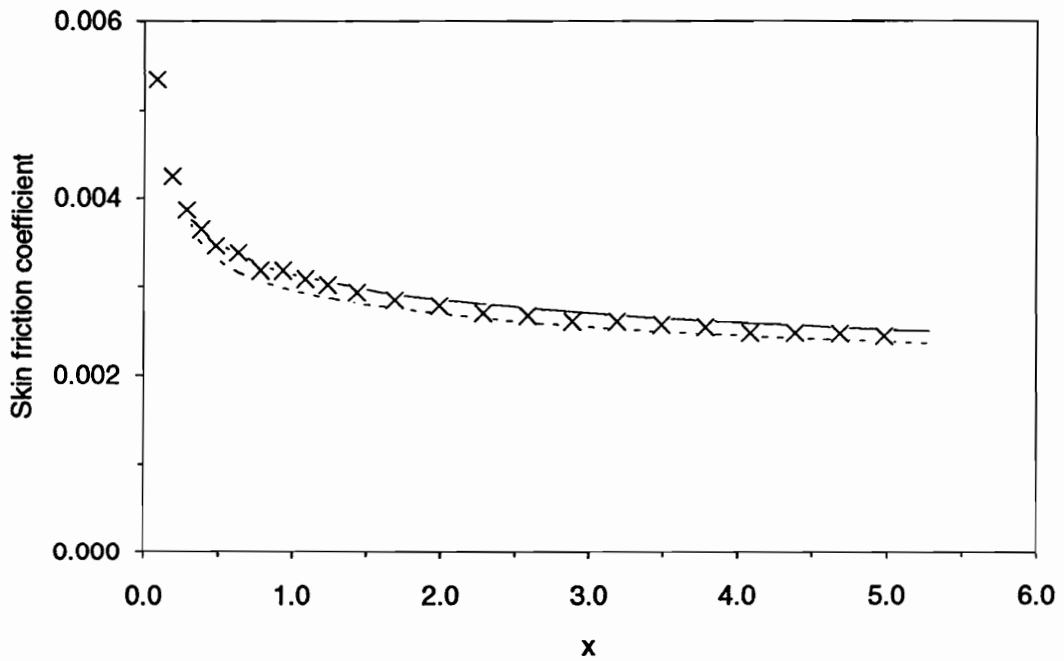
Figure 4.1 Wiegardt-Tillmann - Computational Domain, Flow Conditions, and Boundary Conditions.

Wieghardt-Tillmann Case

$Re = 2.1854 \times 10^6$

Mesh: 61 x 25

$\eta_H = 3.0$



x Experiment

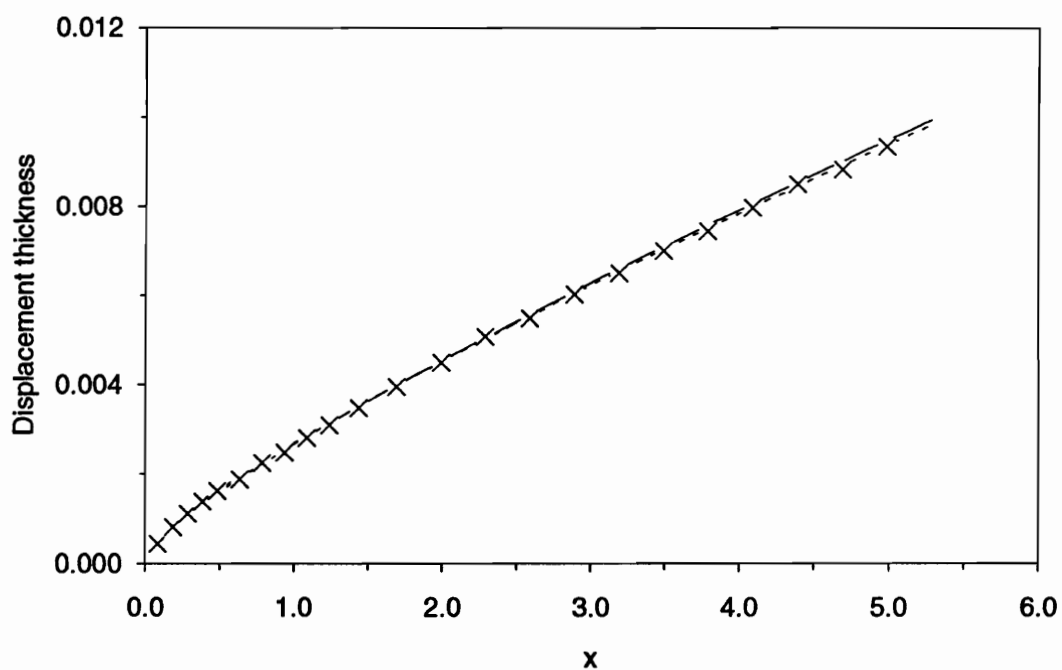
----- STRIP2D Integral Method

———— FENSIE Method

Figure 4.2 Wieghardt-Tillmann - Skin Friction Coefficient along the Plate.

Wieghardt-Tillmann Case $Re = 2.1854 \times 10^6$

Mesh: 61 x 25

 $\eta_H = 3.0$ 

x Experiment STRIP2D Integral Method _____ FENSIE Method

Figure 4.3 Wieghardt-Tillmann - Displacement Thickness along the Plate.

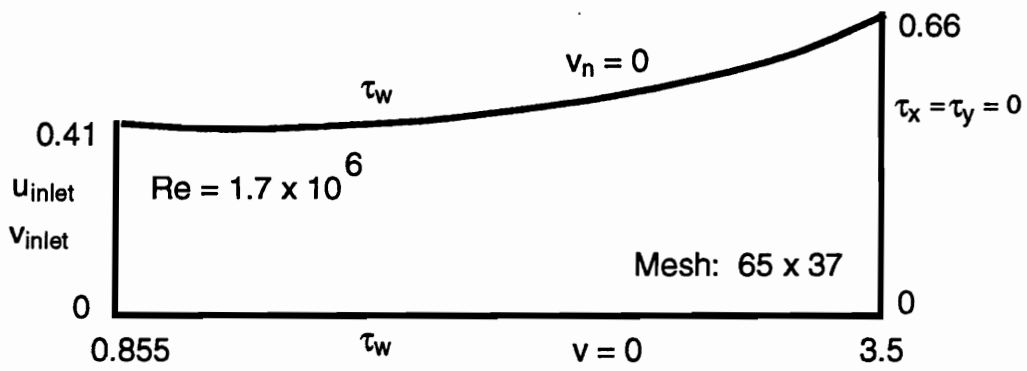


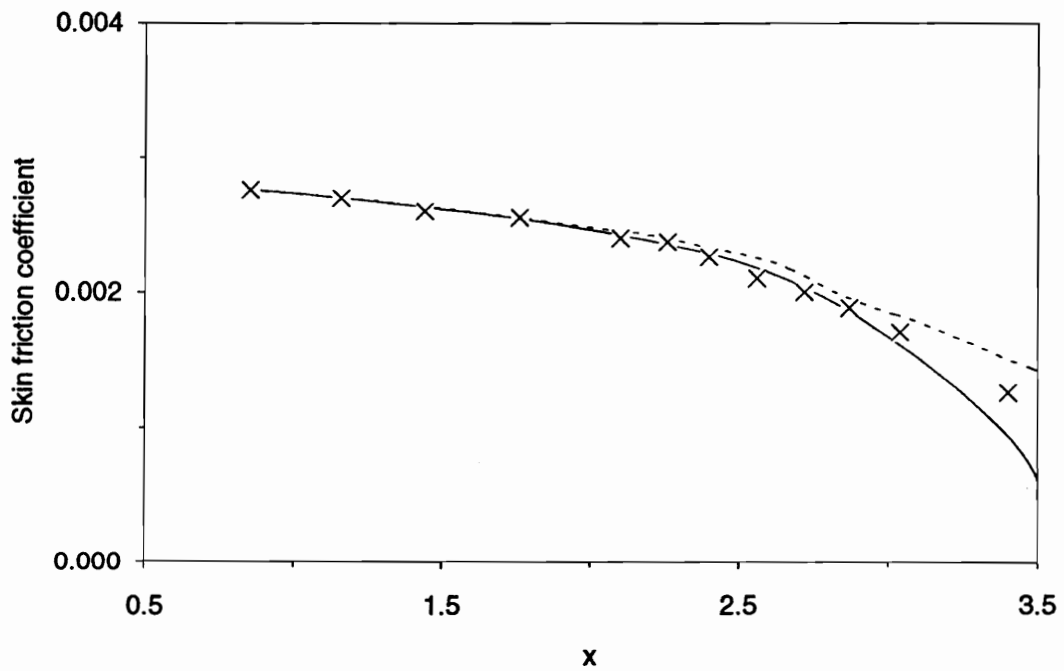
Figure 4.4 Samuel-Joubert - Computational Domain, Flow Conditions, and Boundary Conditions.

Samuel-Joubert Case

$Re = 1.7 \times 10^6$

Mesh: 65 x 37

$\eta_H = 3.0$

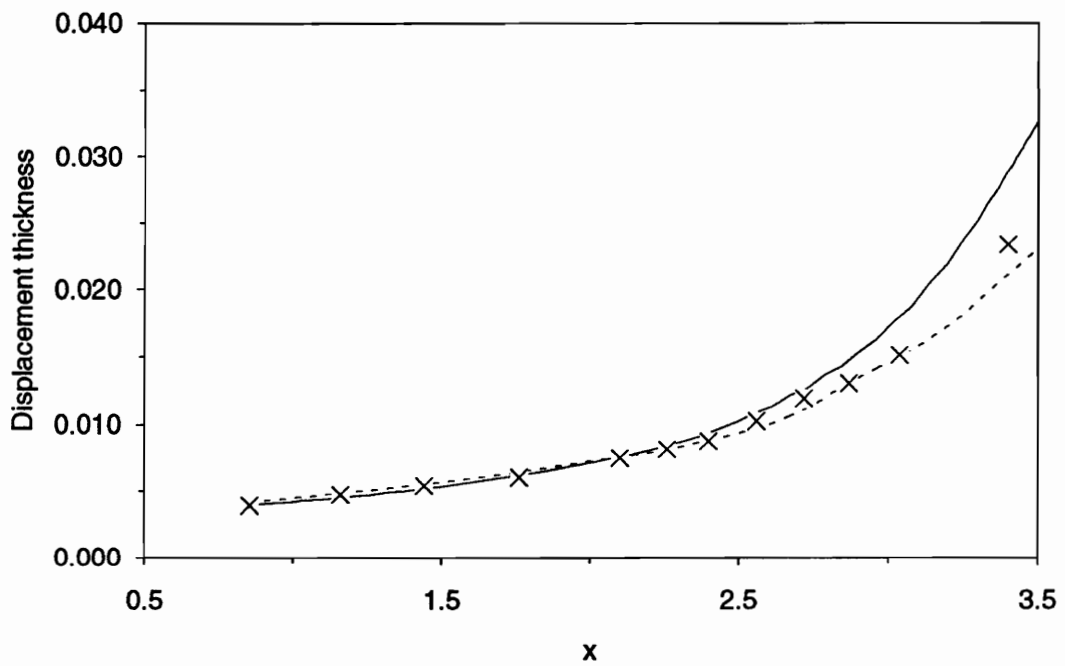


x Experiment
 STRIP2D Integral Method
 _____ FENSIE Method

Figure 4.5 Samuel-Joubert - Skin Friction Coefficient along the Flat Surface.

Samuel-Joubert Case $Re = 1.7 \times 10^6$

Mesh: 65 x 37

 $\eta_H = 3.0$ 

× Experiment - - - - - STRIP2D Integral Method — FENSIE Method

Figure 4.6 Samuel-Joubert - Displacement Thickness along the Flat Surface.

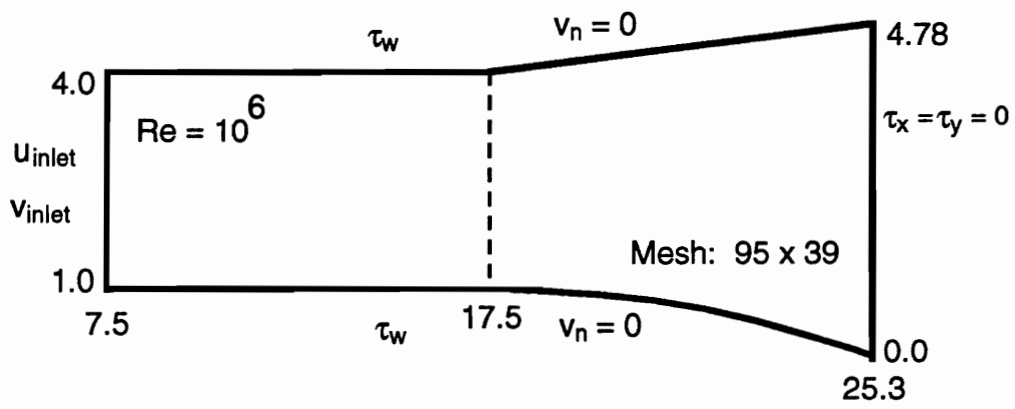


Figure 4.7 Schubauer-Klebanoff - Computational Domain, Flow Conditions, and Boundary Conditions.

Schubauer-Klebanoff Case

$Re = 1.0 \times 10^6$

Mesh: 95 x 39

$\eta_H = 2.0$

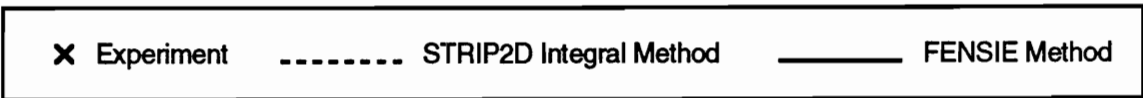
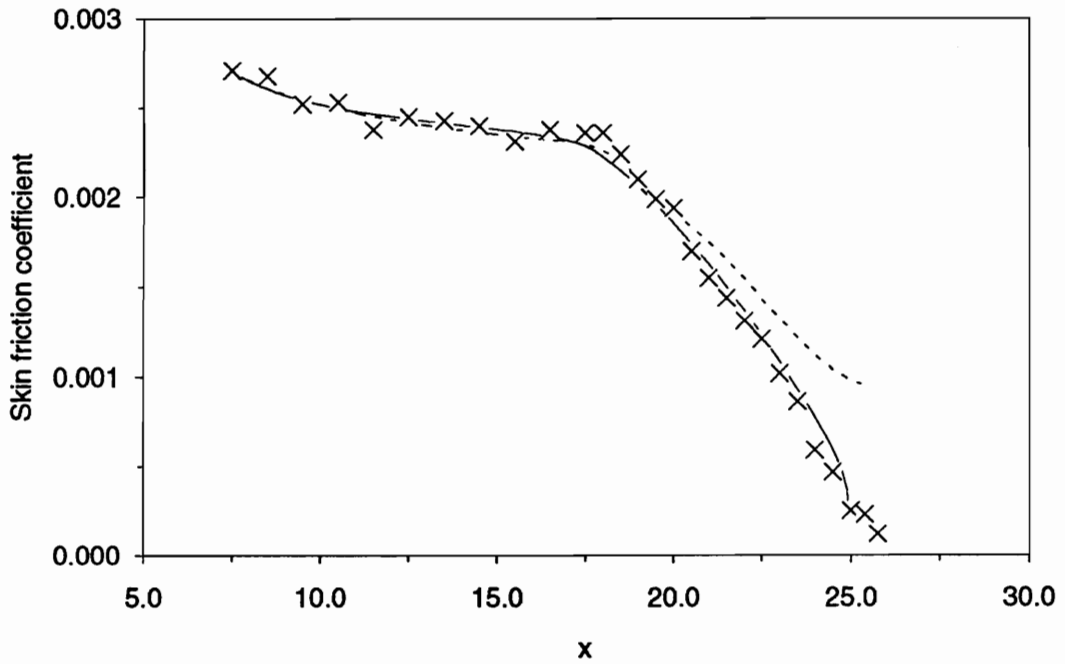


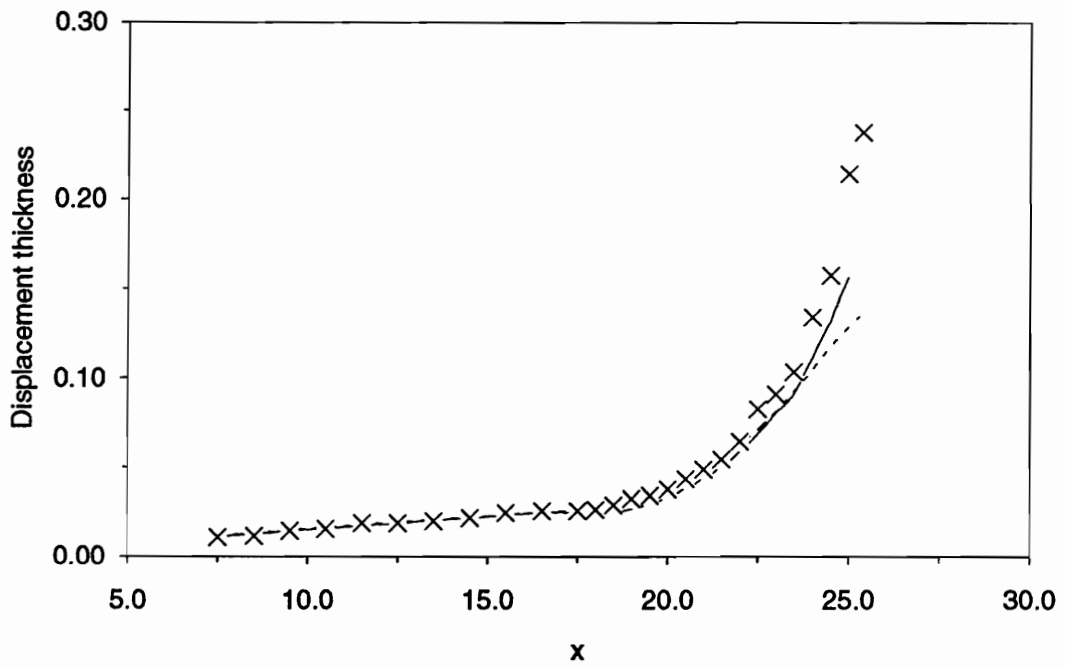
Figure 4.8 Schubauer-Klebanoff - Skin Friction Coefficient along the Body Surface.

Schubauer-Klebanoff Case

$Re = 1.0 \times 10^6$

Mesh: 95 x 39

$\eta_H = 2.0$



x Experiment
 ----- STRIP2D Integral Method
 _____ FENSIE Method

Figure 4.9 Schubauer-Klebanoff - Displacement Thickness along the Body Surface.

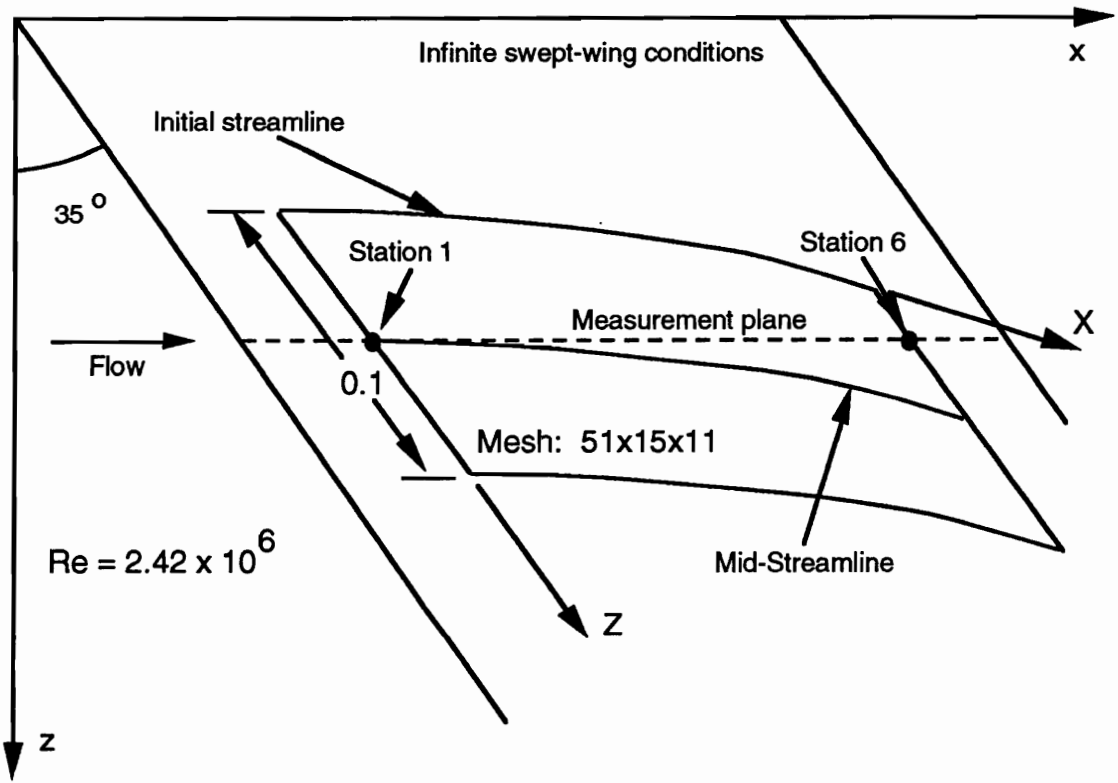


Figure 5.1 Van den Berg-Elsenaar - Computational Domain and Flow Conditions.

Van den Berg-Elsenaar Case

Re = 2.42×10^6

Mesh: 51 x 15 x 11

$\eta_H = 1.5$

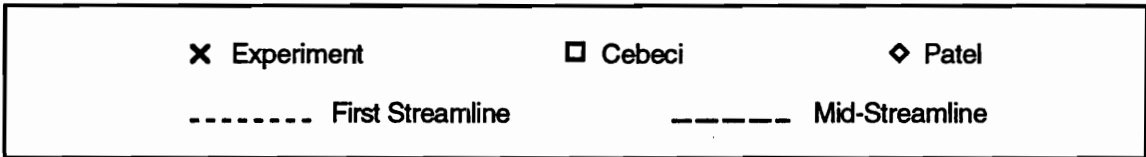
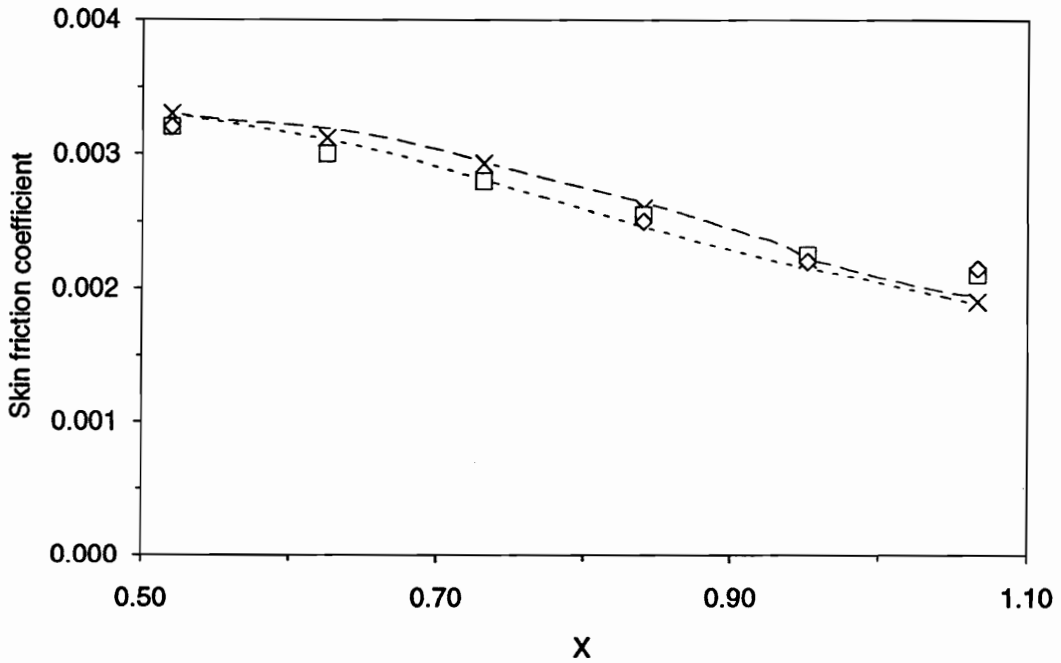


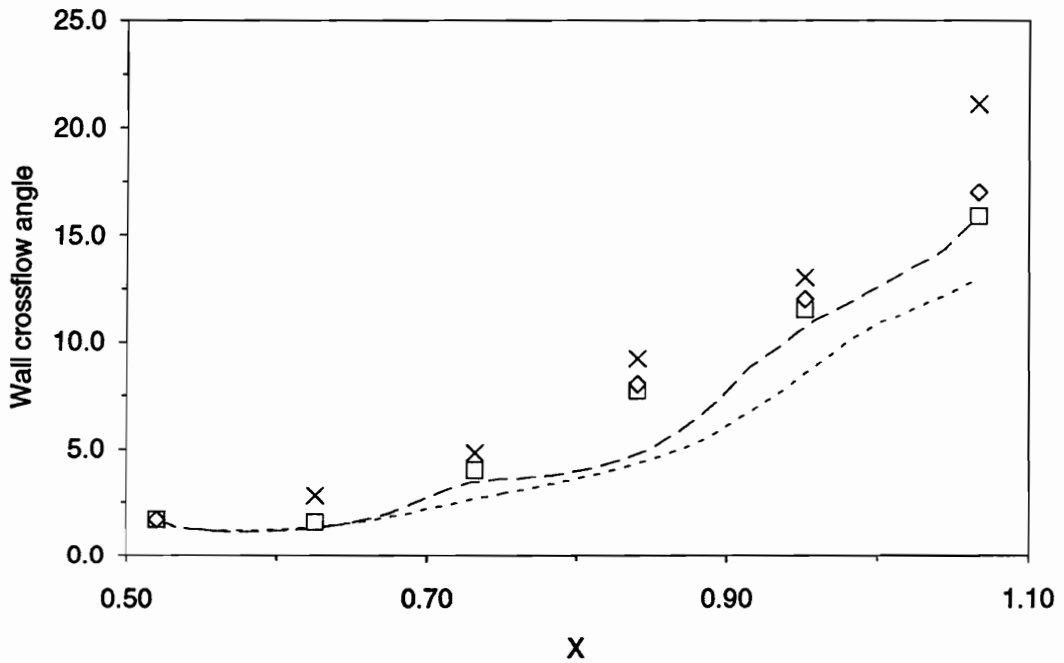
Figure 5.2 Van den Berg-Elsenaar - Skin Friction Coefficient along First and Mid- Streamlines.

Van den Berg-Elsenaar Case

$Re = 2.42 \times 10^6$

Mesh: 51 x 15 x 11

$\eta_H = 1.5$



× Experiment

□ Cebeci

◇ Patel

..... First Streamline

----- Mid-Streamline

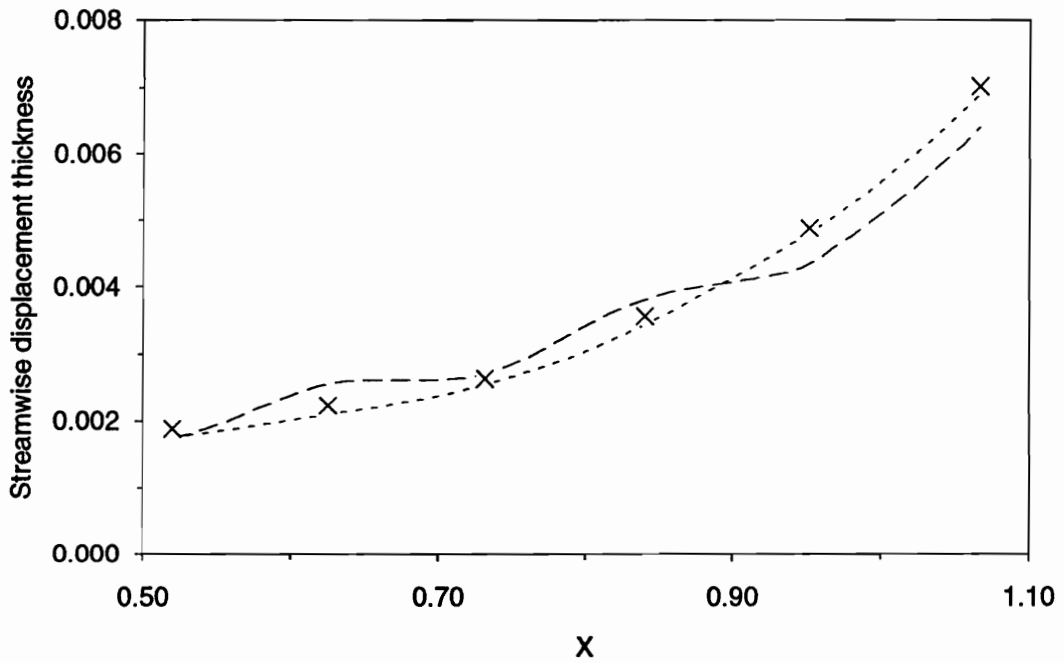
Figure 5.3 Van den Berg-Elsenaar - Wall Crossflow Angle along the First and Mid- Streamlines.

Van den Berg-Elsenaar Case

$Re = 2.42 \times 10^6$

Mesh: 51 x 15 x 11

$\eta_H = 1.5$



X Experiment

..... First Streamline

----- Mid-Streamline

Figure 5.4 Van den Berg-Elsenaar - Streamwise Displacement Thickness along the First and Mid- Streamlines.

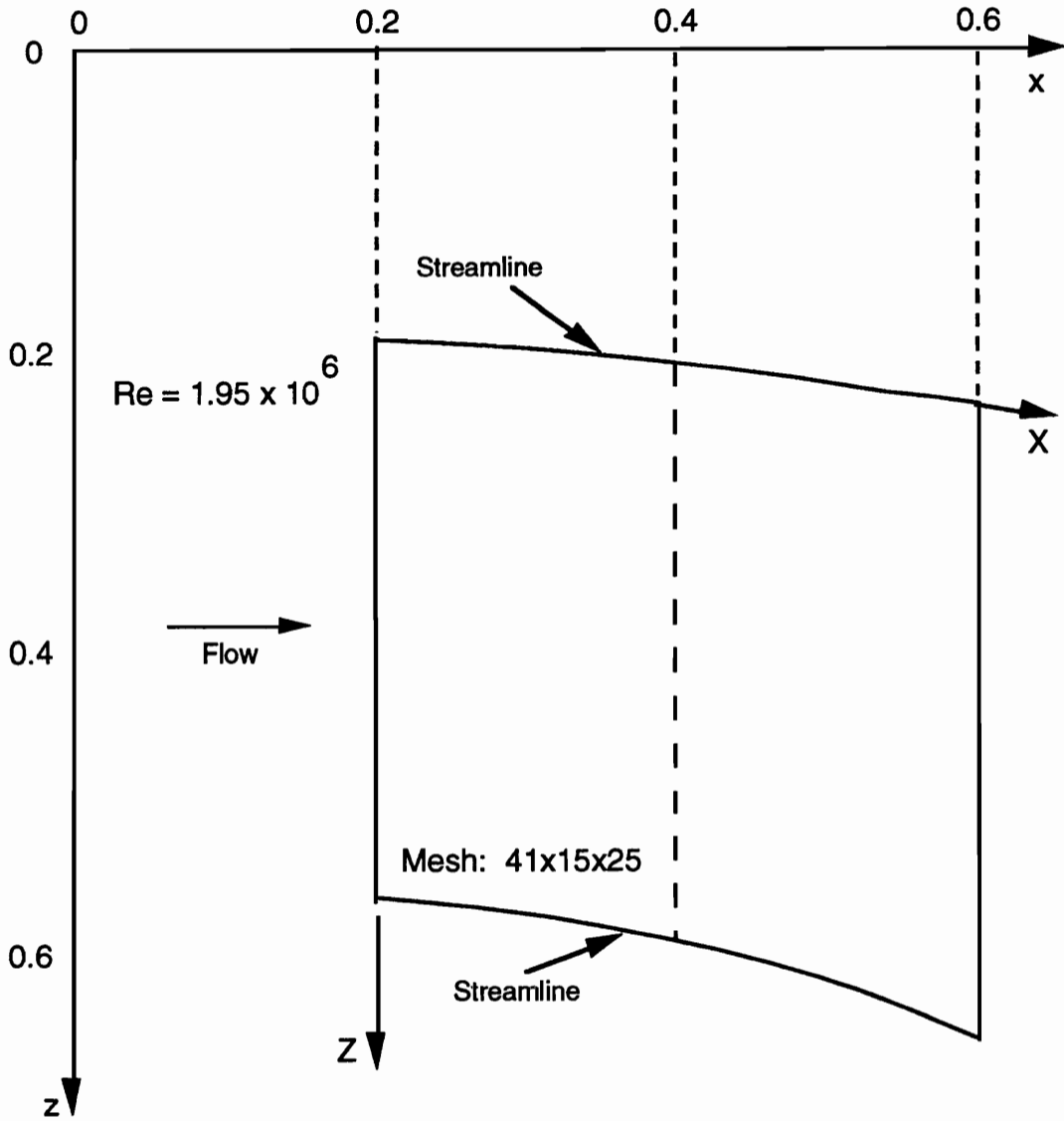


Figure 5.5 Müller-Krause - Computational Domain and Flow Conditions.

Müller-Krause Case - $x=0.4$

$Re = 1.95 \times 10^6$

Mesh: 41 x 15 x 25

$\eta_H = 2.0$

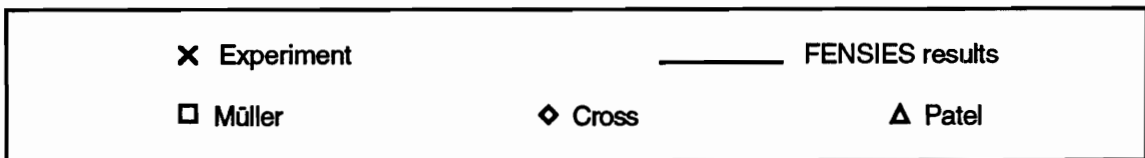
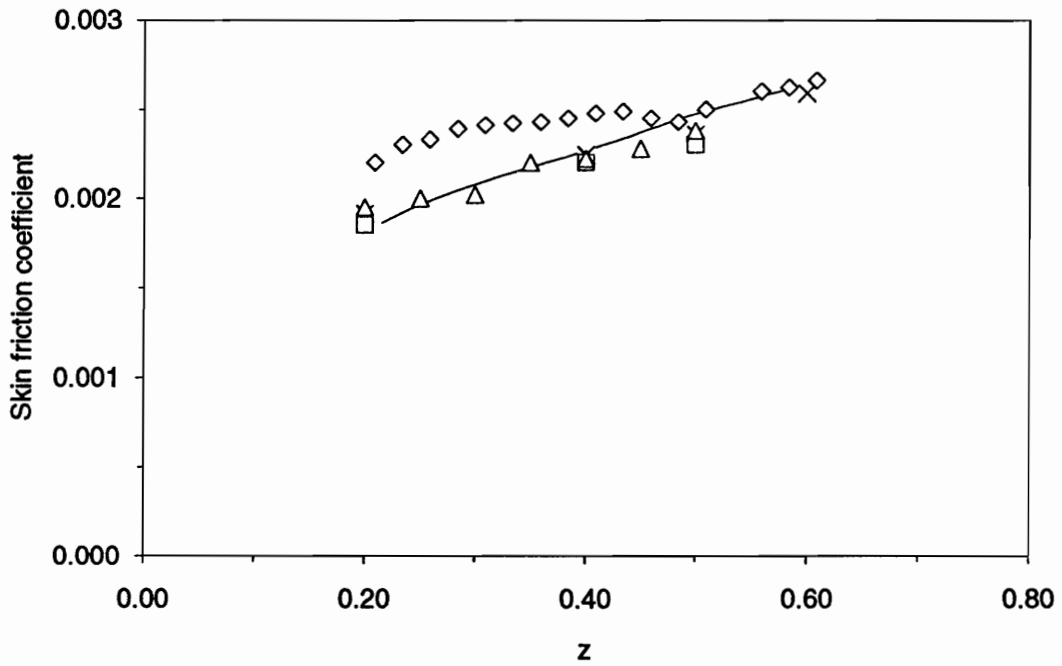


Figure 5.6 Müller-Krause - Skin Friction Coefficient along z-axis at $x=0.4$.

Müller-Krause Case - $x=0.4$

$Re = 1.95 \times 10^6$

Mesh: 41 x 15 x 25

$\eta_H = 2.0$

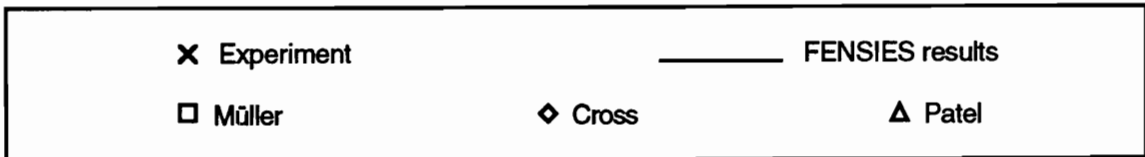
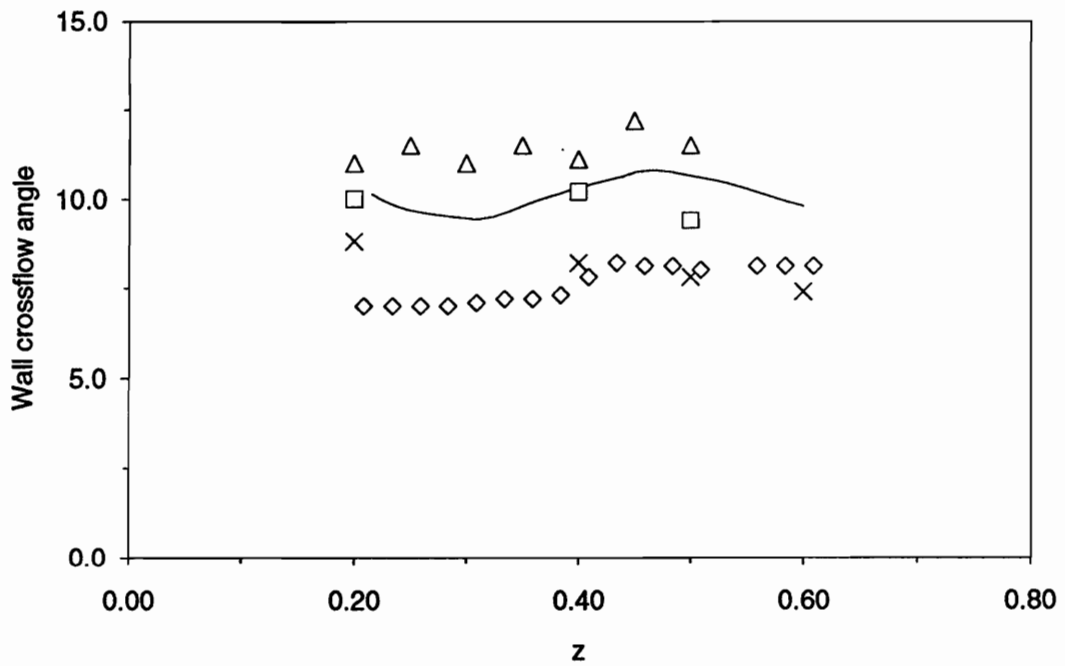
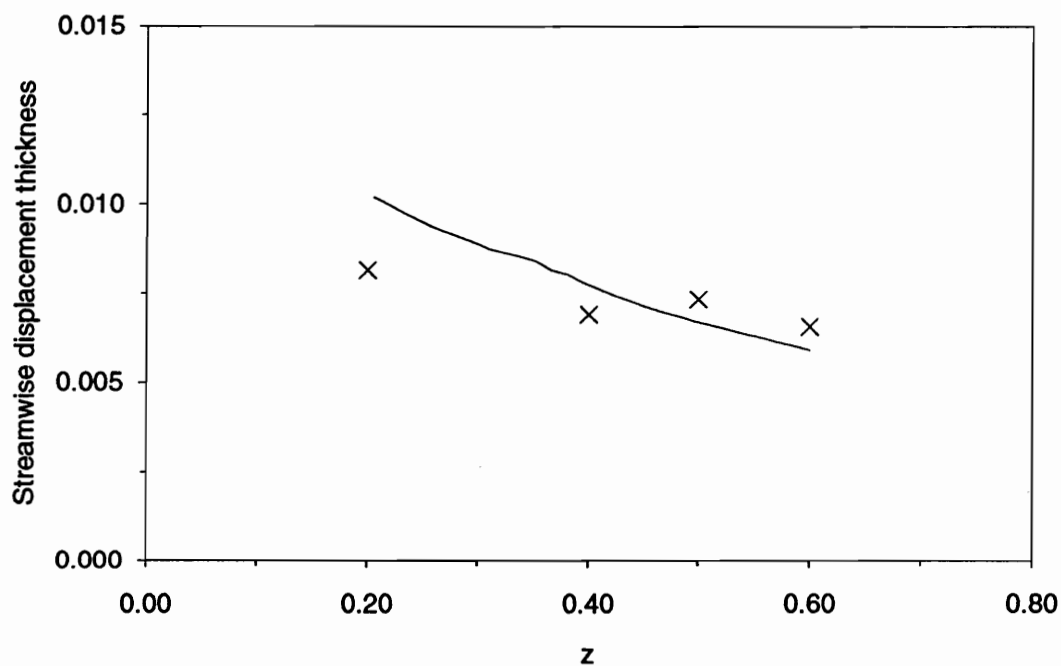


Figure 5.7 Müller-Krause - Wall Crossflow Angle along z-axis at $x=0.4$.

Müller-Krause Case - $x=0.4$ $Re = 1.95 \times 10^6$

Mesh: 41 x 15 x 25

 $\eta_H = 2.0$ 

x Experiment

— FENSIES results

Figure 5.8 Müller-Krause - Streamwise Displacement Thickness along z-axis at $x=0.4$.

Müller-Krause Case - $x=0.6$

$Re = 1.95 \times 10^6$

Mesh: 41 x 15 x 25

$\eta_H = 2.0$

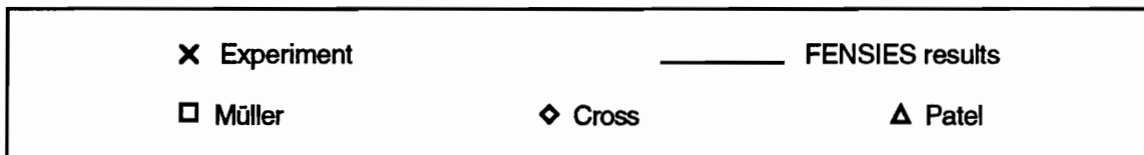
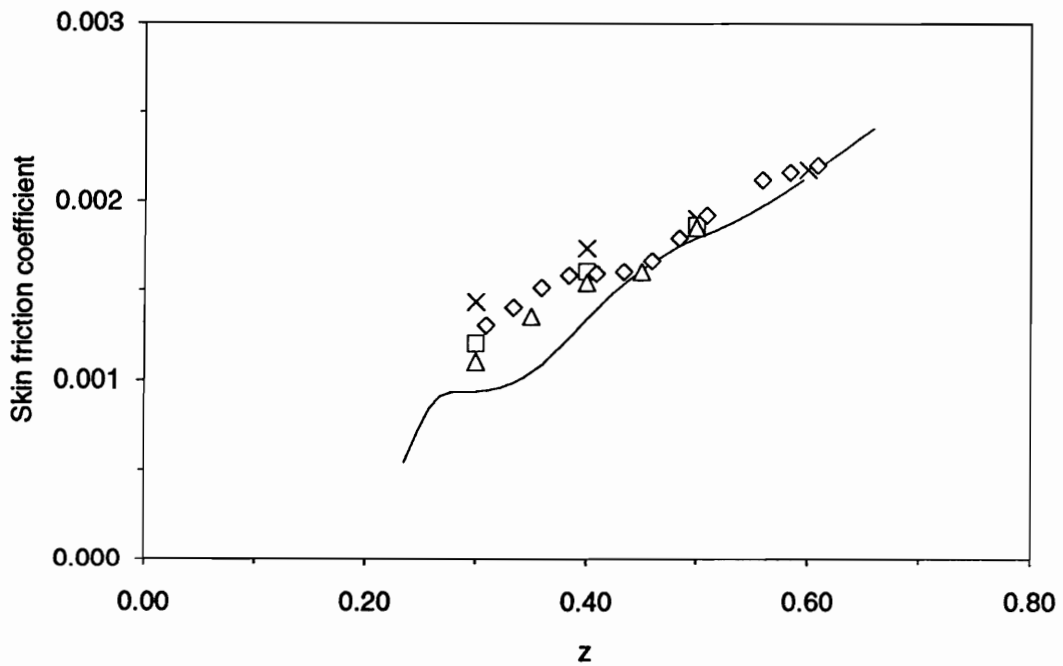


Figure 5.9 Müller-Krause - Skin Friction Coefficient along z-axis at $x=0.6$.

Müller-Krause Case - $x=0.6$

$Re = 1.95 \times 10^6$

Mesh: 41 x 15 x 25

$\eta_H = 2.0$

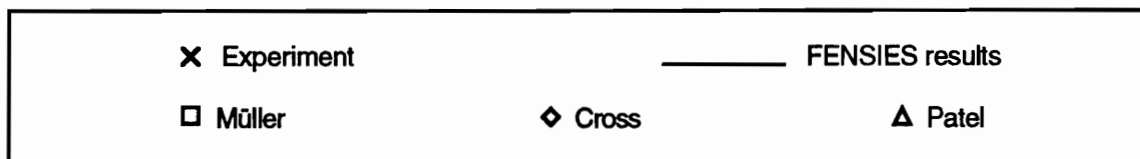
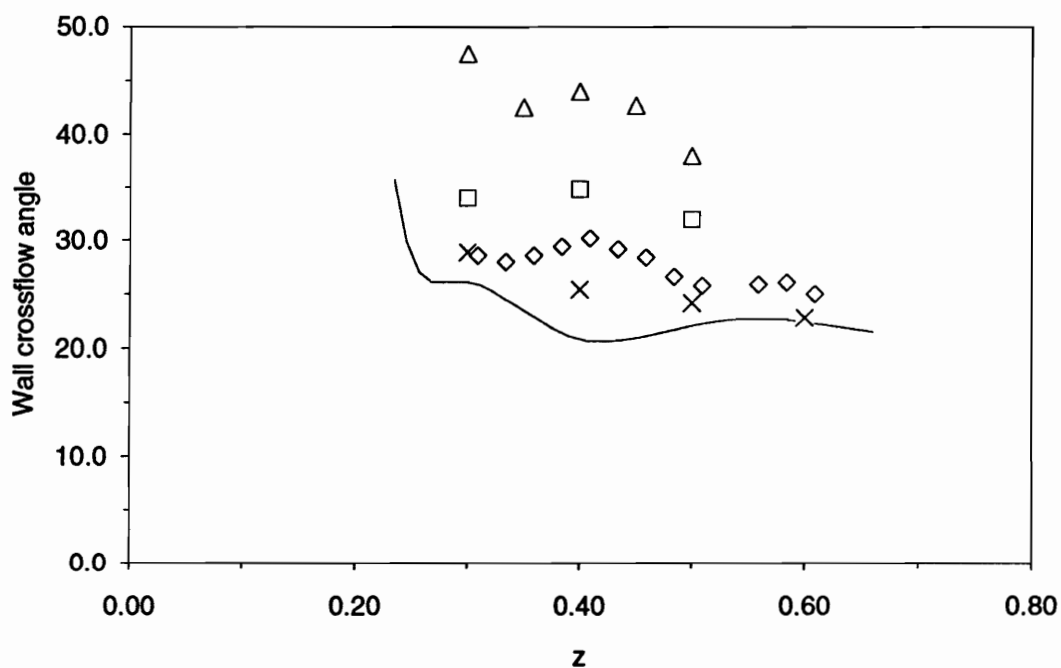
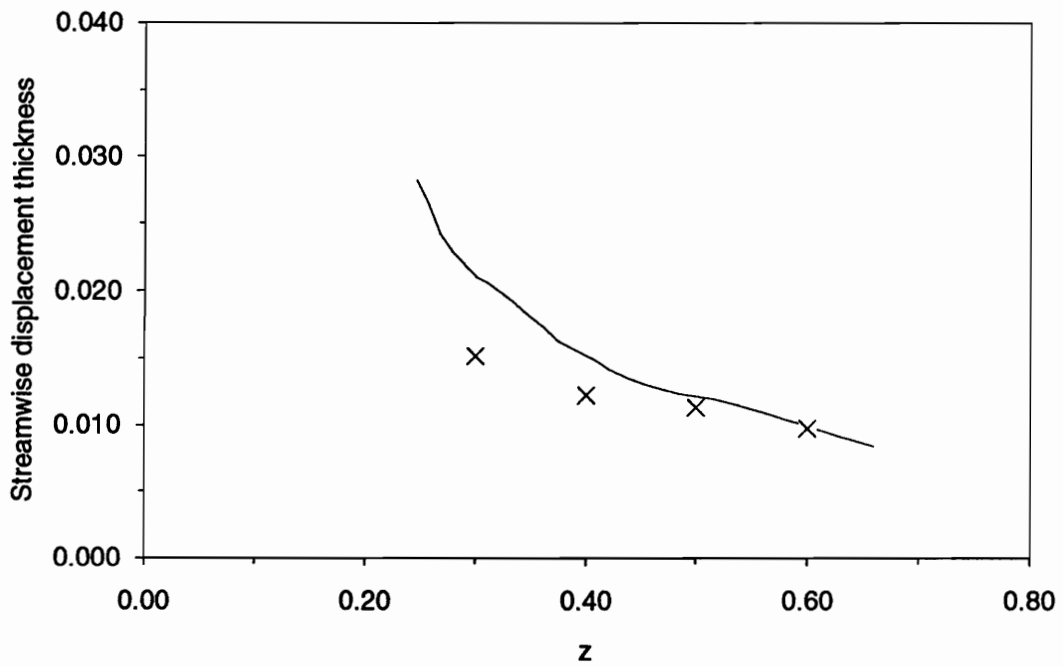


Figure 5.10 Müller-Krause - Wall Crossflow Angle along z-axis at $x=0.6$.

Müller-Krause Case - $x=0.6$ $Re = 1.95 \times 10^6$

Mesh: 41 x 15 x 25

 $\eta_H = 2.0$ **x** Experiment

— FENSIES results

Figure 5.11 Müller-Krause - Streamwise Displacement Thickness along z-axis at $x=0.6$.

VITA

Jean Caillé was born in June 1960 in Courville (Québec), Canada. He studied Mechanical Engineering at Ecole Polytechnique de Montréal and obtained his Bachelor's degree in 1983. He then started his graduate studies in the Applied Mathematics department at the same university, working on Computer-Aided Design systems for turbomachinery applications. He obtained his M.Sc.A. (Master of Science) degree in 1985, and the same year enrolled at VPI&SU in the Aerospace & Ocean Engineering department to pursue his studies at the doctorate level. He held a graduate research assistantship, and focused his interests on computational methods and turbulence modeling for incompressible flows. He also was an instructor for one year teaching classes at the undergraduate and graduate levels. Mr. Caillé is a member of the American Institute of Aeronautics and Astronautics (AIAA).

A handwritten signature in black ink that reads "Jean Caillé". The signature is written in a cursive style with a large initial 'J' and a distinct 'Caillé'.